Titin role in muscle homeostasis:

The kinase domain

Thesis submitted in accordance with the requirements of the University of Liverpool

for the degree of Doctor in Philosophy

by

Julijus Bogomolovas

February 2014

Abstract

The giant muscle protein titin is a central player in cardiovascular health and disease. Titin molecules spanning half of the sarcomere form a filament system in striated muscles. The titin filament is not only an essential structural component of sarcomere, but also plays a central role in myofibril signaling through its kinase domain (TK) and numerous protein ligands. Thus, not surprisingly, mutations in this molecule might have detrimental effects. In this work a structure-driven approach was taken to re-evaluate titin kinase catalytic activity and the pathogenicity of two cardiomyopathy-associated titin mutations.

Comparison of recombinant preparations from *E .coli* and insect cells revealed intrinsic inactivity of TK. It was demonstrated that previously reported phosphotransfer activity towards Tcap (a small Z-disc protein) is due to contaminant kinase activity from insect cells but not TK itself. Next, it was established that the eukaryotic host produces structurally indistinguishable TK from that produced in insect cells, albeit inactive towards Tcap, classical kinase substrates or extracts from mature or differentiating muscles. Structural analysis identified evolutionary conserved residue substitutions converting vertebrate TKs to pseudokinases.

The structural context of dilated cardiomyopathy associated mutation was revealed in the crystal structure of TK enclosing neighboring domains A170 and M1. The mutation site resides in a conserved helix located in the linker region between TK and the binding site of ubiquitin E3 ligase MuRF1. Aspartate to valine substitution causes disruption of a conserved hydrogen bond and detachment of the affected helix from TK. In the context of the titin filament, this causes dissociation of the binding site from TK and increases interdomain flexibility. Structural alterations translate into increased MuRF1-mediated degradation of mutant titin fragments through the ubiquitin-proteasome pathway. Speculatively, haploinsufficiency of mutant titin could be a possible pathomechanism leading to dilated cardiomyopathy associated with the mutation under study.

Comprehensive analysis of arrhythmogenic left ventricular cardiomyopathy associated titin mutation generated a novel model of pathogenesis. In contrast to previous reports, we demonstrate that mutation does not cause affected domain I10 unfolding, and is structurally compatible. Observed destabilization of the domain was attributed to a disrupted hydrogen bond, causing increased flexibility. A crystal structure of the affected domain flanked by adjacent domains I9-I11 demonstrated that threonine to isoleucine substitution might have detrimental effects on interdomain arrangement, resulting in exposure of a hydrophobic patch. Functionally, differential localization of mutant protein was observed in transgenic muscles. Speculatively, mutation could result in impaired folding of mutant protein and lead to accumulation of degradation-resistant aggregates or cause an increased stickiness to thin filaments as a novel pathomechanism.

Results presented in this work demonstrate that TK is a catalytically inactive pseudokinase acting as a molecular scaffold. It was demonstrated that TK and MuRF1 signaling modules are structurally interconnected and genetic perturbation of this link might lead to dilated cardiomyopathy. In similar fashion, genetic alteration of interaction between immunoglobulin domains might cause arrhythmogenic left ventricular cardiomyopathy.

Table of Contents

List of figures

List of tables

List of abbreviations

ARVC	Arrhythmogenic right ventricular cardiomyopathy
ATP	Adenosine triphosphate
BCIP	5-Bromo-4-chloro-3-indolyl phosphate
CRD	C-terminal regulatory domain
Da	Dalton
DCM	Dilated cardiomyopathy
DMEM	Dulbecco modified Eagle medium
DSF	Differential scanning fluorimetry
DTT	Dithiothreitol
FSBA	5′-(4-Fluorosulfonylbenzoyl)adenosine
GFP	Green fluoresecent protein
GST	Glutathione-S-transferase
HCM	Hypertrophic cardiomyopathy
HEPES	(4-(2-hydroxyethyl)-1-piperazineethanesulfonic acid
HSQC	Heternuclear single quantum correlation spectroscopy
Ig	Immunoglobulin
IPTG	Isopropyl β-D-1-thiogalactopyranoside
ITS	Insulin-Selenium-Transferrin
MLC	Myosin light chain
MM	Molecular mass
NBT	Nitro blue tetrazolium
NL	N-terminal linker
NMR	Nuclear magnetic resonance
NTA	Nitrilotriacetic acid
PAGE	Polyacrylamide gel electrophoresis
PBS	Phosphate buffered saline
PEG	Polyethylenglycol
PKA	Protein kinase A
RCM	Restrictive cardiomyopathy
RMSD	Root mean square deviation
SDS	Sodium dodecyl sulfate
TB	Terrific Broth
TBS	Tris buffered saline
TCEP	Tris(2-carboxyethyl)phosphine
TEV	Tobacco Etch Virus
TK	Titin kinase
TLS	Translation/Rotation/Screw
Tris	Tris(hydroxymethyl)aminomethane
TwcK	Twitchin kinase
WT	Wildtype

Acknowledgements

I thank my *Doktoreltern* Olga Mayans and Siegfried Labeit for giving me chance to work on such an interesting project. I am thankful to Siegfried for encouraging me to start PhD project directly after BSc and Olga for taking a risk and accepting me at University of Liverpool. With your advice and direction I was able to develop my research interests and skills and pursue often challenging project. As well I would like to thank my second supervisor Mark Wilkinson.

I am grateful to Caroline Dart and Igor Barsukov for following my PhD project progress as assessors. I would also thank Caroline and Belinda Bullard for agreeing to be examiners for my final viva.

I would like to thank all my lab colleagues in Mannheim. Especially, Alexander Gasch for his daily help in the lab, scientific (and not so) discussions, coffee and lunch breaks. I am thankful to Dittmar Labeit for taking care of the entire administrative load in Germany.

I am thankful to Teresa Carlomagno group and especially Bernd Simon for his long-standing and fruitful collaboration on biomolecular NMR and many helpful discussions.

I am thankful to Rüdiger Rudolf and his group for the transgenic muscle experiments and Coen Ottenheijm lab for the biomechanical measurements.

I owe many thanks to my lab mates in Liverpool: Barbara Franke, Christopher Hill, Rhys Williams and Thomas Zacharenko for their invaluable scientific and linguistic help with project and thesis.

I am grateful to my friends, especially Angerona, Linas, Mantautas and Paulius, tearing me away from the lab and reminding me of a life outside.

Last but not least, I owe this thesis to a great extent to my family, without their support, encouragements this would never be achieved. To them I dedicate this thesis.

Chapter 1

General introduction and aims

1.1 Introduction

Diseases of the cardiovascular system are the major cause of death worldwide. Understanding the molecular mechanisms that underlie the pathogenesis of cardiovascular diseases is essential for the development of effective therapies that can reduce the increasing mortality rates and treatment costs. Evidence accumulated over the past two decades have identified titin as the major coordinator of striated muscle homeostasis, and its dysfunction as an important element in the pathogenesis of cardiovascular diseases. At up to 4.2 MDa titin is the largest polypeptide chain so far discovered (Bang et al., 2001). Whilst the titin polypeptide is easily overlooked by standard analytical procedures, titin is in fact the third most abundant component of vertebrate striated muscle after myosin and actin (Fulton and Isaacs, 1991, Labeit et al., 1997). Titin molecules from adjacent half-sarcomeres are connected within the Z-disk and in the M-line lattices by interactions with Z-disc and M-line proteins, making a continuous filament system within the myofibril. Titin filaments contribute to the muscle homeostasis in two major ways: the maintenance of muscle biomechanical properties and the functional integration of sarcomere signaling pathways. Titin elasticity plays a crucial role in restoring the sarcomere back to its slack length after a stretch or a contraction (Granzier and Labeit, 2004). In cardiac muscle titin contributes to the Frank-Starling mechanism (Fukuda and Granzier, 2005, Helmes et al., 2003). Biomechanical properties of titin adjust to changing demands in multiple ways. These include alternative splicing (Guo et al., 2010), posttranslational modifications (Hidalgo et al., 2009) and ligand binding (Zhu et al., 2009), to name but a few. Thus indicating that titin-based force generation is a finely tuned process of a central importance. Secondly, multiple ligands make titin a major coordinator of sarcomere signaling (Granzier et al., 2002) (**Figure 1.1**) At Z-disc titin interacts with numerous structural and regulatory proteins (Linke and Kruger, 2010, Knoll and Buyandelger, 2013) Structurally titin is anchored in Z-discs throught interaction with

telethonin (Mues et al., 1998, Gregorio et al., 1998), α-actinin (Eilertsen et al., 1997), filamins (Labeit et al., 2006), small ankyrin-1 (Kontrogianni-Konstantopoulos and Bloch, 2003), obscurin (Bang et al., 2001) and nebulin in skeletal muscle (Witt et al., 2006). Moreover, these interactions bear a regulatory aspect, as for example, telethonin-MLP (Muscle LIM protein) interaction is a basis of mechanical stretch sensor machinery (Knoll et al., 2002) and titin interaction with potassium channels contributes to a stretch-dependent regulation of potassium flux in cardiac muscle, providing a "mechano-electrical feedback" system (Furukawa et al., 2001). In I- and A-bands titin interacts with components of thin (Jin, 2000, Linke et al., 2002, Trombitas et al., 1997) and thick filaments (Isaacs et al., 1992, Houmeida et al., 1995, Freiburg and Gautel, 1996), respectively. In addition, the I-band is one of the localization sites for the calcium dependent proteases, calpains (Hayashi et al., 2008, Raynaud et al., 2005) and N2A sequence localized is a binding site for a stretch-sensing family of muscle ankyrin repeat proteins: CARP, ankrd2/Arpp and DARP (Miller et al., 2003). In the M-band a large proportion of interactions are centred on the kinase domain. The family of muscle specific RING-finger (MuRF) ubiquitin ligases is either bound in close proximity or directly to the kinase domain (Mrosek et al., 2007, Centner et al., 2001, Lange et al., 2005). Furthermore M-line located Ig domains and their linking regions interact with various protein ligands. The sequence between M3 and M4 domains serves a as binding site for FHL-2 protein which links titin to metabolic enzymes (Lange et al., 2002); the M4 domain itself mediates interaction with myomesin, thus providing an additional link between titin and thick filament (Obermann et al., 1997). Interactions with calpain-3 (Sorimachi et al., 1996) and obscurin (Fukuzawa et al., 2008) are central to muscle homeostasis, as mutation-caused impairment of these interactions are shown to be a pathogenetic factor in the development of limb-girdle muscular dystrophy type 2A (Ojima et al., 2010) and C-terminal titin deletions cause a novel early-onset myopathy with fatal cardiomyopathy (Carmignac et al., 2007). Taken together, the titin filament is a major coordinator of sarcomere signaling.

Figure 1.1 Titin and titin ligands. Upper panel. Organization of titin (blue) and nebulin (red) in sarcomere from skeletal muscle**. Lower panel.** Titin-domain architecture (N2A-isoform of human skeletal muscle) laid out in a half-sarcomere, titin ligands, and main avenues of titin-based signaling Note that the thick filament-associated segment of titin in the A band contains 6 super-repeats each comprising 7 modular domains and 11 super-repeats each comprising 11 modular domains. Ankrd2, ankyrin repeat domain protein-2; Bin1, bridging integrator protein-1; CARP, cardiac-ankyrin-repeat-protein; DARP, diabetes-related ankyrin-repeat protein; FHL2, four-and-a-half-LIM-domain protein; MDM2, mouse double minute-2 protein; MLP, muscle LIM protein; MURFs (1/2), muscle-specific RING finger proteins(-1/-2); MyBP-C, myosin-binding protein C; MyHC, myosin heavy chain; Nbr1, neighbour of BRCA1 gene-1 (©2010 by American Physiological Society.
Taken from Linke and Kruger, 2010.

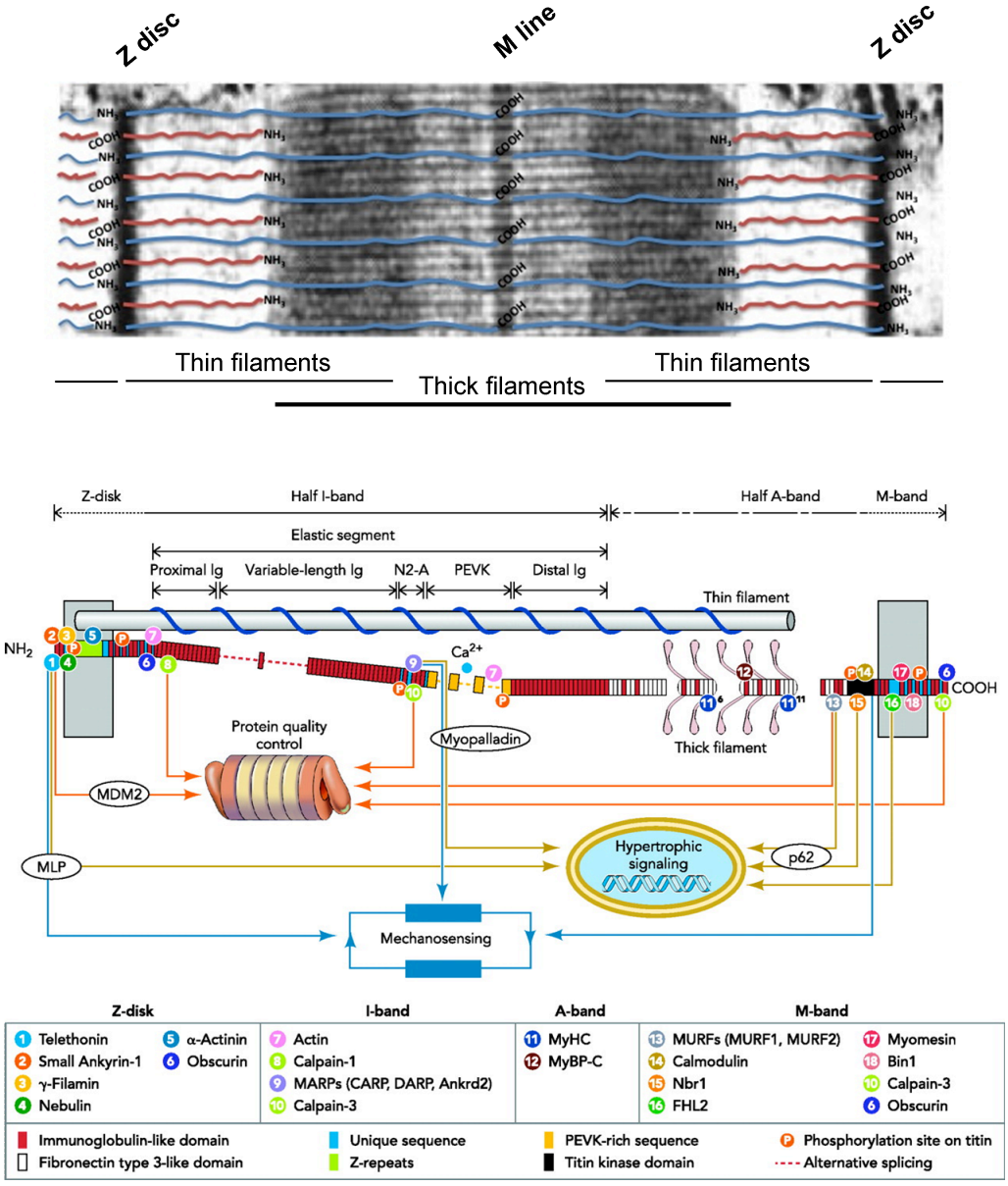

Consequently, titin dysfunction is an important element in the pathogenesis of cardiovascular diseases. Up to 108 titin mutations were found to be associated with all major types of human cardiomyopathies: dilated (DCM), hypertrophic (HCM), arrhythmogenic left ventricular (ARVC) and restrictive (RCM) (**Table 1.1 and Appendix 1**).

Table 1.1 List of cardiomyopathy-linked titin mutations. Location of mutation is referenced according the corresponding publication. DCM: dilated cardiomyopathy, HCM: hypertrophic cardiomyopathy, ARVC: arrhythmogenic right ventricular cardiomyopathy, RCM: restrictive cardiomyopathy, *: stop, IVS: intron, del: deletion, ins: insertion, fs: frameshift. (© 2013 Maegen A. Ackermann and Aikaterini Kontrogianni-Konstantopoulos. Adapted from Ackermann and Kontrogianni-Konstantopoulos, 2013 published under the CC BY 3.0 license. Available from: http://dx.doi.org/10.5772/55609)

Pathology	Mutation	Localization	Effect	Reference
DCM	V54M	Z-disc	↓ binding to telethonin	Itoh-Satoh et al., 2002
DCM	R743L	Z-disc	↓ binding to α-actinin	Satoh et al., 1999
DCM	W976R	Z-disc	Unknown	Gerull et al., 2002
DCM	Q4007*	I-band	Truncation	Itoh-satoh et al., 2002
DCM	Q4249*	I-band	Truncation	Herman et al., 2012
DCM	S4417N	I-band	↓ binding to FHL2	Itoh-satoh et al., 2002
DCM	G3470D	I-band	Unknown	Liu et al., 2008
DCM	C13771*	I-band	Truncation	Herman et al., 2012
DCM	G16189*	A-band	Truncation	Herman et al., 2012
DCM	W16359*	A-band	Truncation	Herman et al., 2012
DCM	R17295*	A-band	Truncation	Herman et al., 2012
DCM	R17470*	A-band	Truncation	Herman et al., 2012
DCM	E17783*	A-band	Truncation	Herman et al., 2012
DCM	C18789*	A-band	Truncation	Herman et al., 2012

DCM	R18858*	A-band	Truncation	Herman et al., 2012
DCM	R18985*	A-band	Truncation	Herman et al., 2012
DCM	R19560*	A-band	Truncation	Herman et al., 2012
DCM	R20858*	A-band	Truncation	Herman et al., 2012
DCM	Q25689*	A-band	Truncation	Herman et al., 2012
DCM	W26632*	A-band	Truncation	Herman et al., 2012
DCM	R26949*	A-band	Truncation	Herman et al., 2012
DCM	K27016*	A-band	Truncation	Herman et al., 2012
DCM	W27147*	A-band	Truncation	Herman et al., 2012
DCM	Y27567*	A-band	Truncation	Herman et al., 2012
DCM	W29318*	A-band	Truncation	Herman et al., 2012
DCM	R29415*	A-band	Truncation	Herman et al., 2012
DCM	E29510*	A-band	Truncation	Herman et al., 2012
DCM	Q30081*	A-band	Truncation	Herman et al., 2012
DCM	R31195*	A-band	Truncation	Herman et al., 2012
DCM	K31371*	A-band	Truncation	Herman et al., 2012
DCM	S31841*	A-band	Truncation	Herman et al., 2012
DCM	R32069Q	A-band	Unknown	Matsumoto et al., 2005
DCM	IVS118-g>a	I-band	Truncation	Herman et al., 2012
DCM	IVS172-g>c	I-band	Truncation	Herman et al., 2012
DCM	IVS172+g>a	I-band	Truncation	Herman et al., 2012
DCM	IVS185-2a>g	I-band	Truncation	Herman et al., 2012
DCM	IVS230+g>t	A-band	Truncation	Herman et al., 2012
DCM	IVS237+3a>g	A-band	Truncation	Herman et al., 2012

DCM	IVS253-5t>a	A-band	Truncation	Herman et al., 2012
DCM	IVS254-g>a	A-band	Truncation	Herman et al., 2012
DCM	IVS255+g>a	A-band	Truncation	Herman et al., 2012
DCM	IVS271+5g>a	A-band	Truncation	Herman et al., 2012
DCM	IVS274-2a>g	A-band	Truncation	Herman et al., 2012
DCM	IVS276+5g>c	A-band	Truncation	Herman et al., 2012
DCM	IVS277+g>a	A-band	Truncation	Herman et al., 2012
DCM	IVS279+2t>a	A-band	Truncation	Herman et al., 2012
DCM	IVS302+g>c	A-band	Truncation	Herman et al., 2012
DCM	6247 del g R2083fs	I-band	Unknown	Herman et al., 2012
DCM	19183 del g S6395fs	I-band	Unknown	Herman et al., 2012
DCM	44336 del a E14779fs	A-band	Unknown	Herman et al., 2012
DCM	44725 del t D14909fs	A-band	Unknown	Herman et al., 2012
DCM	45322 del t F15108fs	A-band	Unknown	Herman et al., 2012
DCM	53935 del c E17978fs	A-band	Unknown	Herman et al., 2012
DCM	60147 del c P20049fs	A-band	Unknown	Herman et al., 2012
DCM	64925 del t K21640fs	A-band	Unknown	Herman et al., 2012
DCM	65867 del a E21956fs	A-band	Unknown	Herman et al., 2012
DCM	67745 del t P22582fs	A-band	Unknown	Herman et al., 2012
DCM	81536-81537 del ct S27179fs	A-band	Unknown	Herman et al., 2012
DCM	84977-84980 del atta Y28326fs	A-band	Unknown	Herman et al., 2012
DCM	82381 del g A27460	A-band	Truncation	Gerull et al., 2006
DCM	89180-89184 del ttaaa T29725fs	A-band	Unknown	Herman et al., 2012
DCM	91043 del a N30348fs	A-band	Unknown	Herman et al., 2012

DCM	DCM 93376-93377 del ag R31126fs	A-band	Unknown	Herman et al., 2012
DCM	97824-97831 del agtgacca A32606fs	M-line	Unknown	Herman et al., 2012
DCM	98964 del a K32987fs Ig150	M-line	Unknown	Herman et al., 2012
DCM	38621 ins a A12873fs	I-band	Unknown	Herman et al., 2012
DCM	28kb duplication of ex 72-124	I-band	Unknown	Herman et al., 2012
DCM	53145 ins g E17715fs	A-band	Unknown	Herman et al., 2012
DCM	58880 ins a* S19628fs	A-band	Truncation	Yoskovitz et al., 2012
DCM	62986-62987 ins at ex. 326	A-band	Truncation	Gerull et al., 2002
DCM	72178 ins t Q24059fs	A-band	Unknown	Herman et al., 2012
DCM	78372 ins a G26124fs	A-band	Truncation	Yoskovitz et al., 2012
DCM	90493 ins cct T30165fs	A-band	Unknown	Herman et al., 2012
DCM	91537 ins a T30513fs	A-band	Unknown	Herman et al., 2012
DCM	67057-67063 del gcatatg ins ta^A22353fs	A-band	Unknown	Herman et al., 2012
DCM	72723-72739 del a ins aga S24241fs	A-band	Unknown	Herman et al., 2012
HCM	R740L	Z-disc	↑ binding to α-actinin	Satoh et al., 1999
HCM	S3753Y	I-band	↑ binding to FHL2	Itoh-Satoh et al., 2002
HCM	R8500H	I-band	↑ binding to CARP	Arimura et al., 2009
HCM	R8604Q	I-band	↑ binding to CARP	Arimura et al., 2009
HCM	IVS155+g>t	I-band	Unknown	Herman et al., 2012
HCM	23798-23810 del gtcaagatatctg G7933fs	I-band	Unknown	Herman et al., 2012
HCM	60147 del C	A-band	Unknown	Herman et al., 2012
ARVC	T2896I	I-band	↓ Stability	Taylor et al., 2011
ARVC	Y8031C	I-band	Unknown	Taylor et al., 2011

ARVC	H8848Y	I-band	Unknown	Taylor et al., 2011
ARVC	I16949T	A-band	Unknown	Taylor et al., 2011
ARVC	A18579T	A-band	Unknown	Taylor et al., 2011
ARVC	A19309S	A-band	Unknown	Taylor et al., 2011
ARVC	P30847L	A-band	Unknown	Taylor et al., 2011
ARVC	M33291T	M-line	Unknown	Taylor et al., 2011
RCM	Y7621C	I-band	Unknown	Peled et al., 2014

The vast majority of titin mutations have been causally linked to DCM (Itoh-Satoh et al., 2002, Satoh et al., 1999, Gerull et al., 2006, Gerull et al., 2002, Matsumoto et al., 2005, Yoskovitz et al., 2012, Herman et al., 2012). In particular, mutation caused titin truncations were shown to be a common cause of dilated cardiomyopathy, found in 25% of familial cases of idiopathic dilated cardiomyopathy and in 18% of sporadic cases (Herman et al., 2012). However, the pathomechanism leading to DCM due to titin truncations might be rather pleotropic in nature as some truncated titin variants are found only at transcript level (Gerull et al., 2006), whereas others are integrated into the sarcomere (Gerull et al., 2002). Moreover, the unequal distribution of truncating mutations in DCM patients might indicate that truncated titins are integrated into the sarcomere and cause dilated cardiomyopathy by means of a dominant negative mechanism and not haploinsufficiency (Herman et al., 2012). In comparison, nonsense mutations have been causally linked to HCM (Satoh et al., 1999, Satoh et al., 2002, Arimura et al., 2009), ARVC (Taylor et al., 2011) and RCM (Peled et al., 2014). Thus, clinical data imply that association of titin mutations with cardiomyopathy is a widespread and possibly causative phenomenon.

However delineating causative genotype-phenotype links in genetic heart disorders is a demanding task for the following reasons. Firstly emerging new generation sequencing technologies revealed unexpectedly large variation in the human genome, consisting mainly of rare genetic variants (Nelson et al., 2012, Keinan and Clark, 2012). Thus, rare sarcomeric gene variations associated with

cardiomyopathy in small patient families were found to be present in 17% of the NHLBI GO Exome Sequencing Project population (Norton et al., 2012) indicating that alone small-size association studies are insufficient to reliably discern disease causing mutation from benign rare variants. Secondly, rare genetic variants of sarcomeric genes might have very complicated penetrance pattern. It was shown that the risk of adverse cardiovascular events grows with increasing numbers of rare sarcomeric variants (Bick et al., 2012). Consequently, differentiation between benign and pathogenic genetic variants requires integration with functional assays, robust bioinformatics, large control cohorts and expert clinical evaluation (Mestroni and Taylor, 2013).

In this work a structure-driven approach was undertaken to gain evidence for the discrimination between benign and pathogenic rare titin genetic variations and understand the possible molecular pathomechanism.

A gigantic titin protein is a great challenge for the structural biology. However, due to repetitive nature of the molecule, obtained structures can serve for reliable estimations of larger titin fragments. Thus, depth of structural knowledge varies among different structural regions of titin (**Table 1.2**). Out of numerous interactions titin is involved in the Z-discs (Hoshijima, 2006) structures are known only for two: Z1Z2 with Tcap, a small protein embedding N-termini of the titin into the Z-discs. (Pinotsis et al., 2006, Zou et al., 2006) and Z-repeat with α-actinin (Atkinson et al., 2001). The I-band of titin consists mainly of 50-100 (depending on isoform) Ig-tandems, however structures of only 8 domains are known to date. This region functionally and structurally is divided according to splicing patterns into two subregions: the constitutively expressed region is interrupted by alternatively spliced Ig-tandems. Functionally it was shown that at least proximal Ig-tandems are not extensible upon the physiological sarcomere stretch (Furst et al., 1988) and might interact with thin filament (Granzier et al., 1997, Jin, 2000, Trombitas et al., 1997, Trombitas and Pollack, 1993, Trombitas et al., 1993). The alternatively spliced elastic region of titin is well represented by the I67-I69 tandem. Structure of such a comprehensive piece of titin chain revealed high order organization (von Castelmur et al., 2008) and allowed generation of a precise model explaining the elasticity of this filament region (Lee et al., 2010). Thus, structural knowledge on alternatively spliced

regions of titin I-band is sufficient to estimate the mutational effects in this region and gain insights into underlying pathomechanisms. However, structural knowledge on constitutively expressed regions of titin's I-band is very scarce. This region is represented only by two structures of single Ig domains: I1 from proximal and I91 from distal regions. Structures of 8 domains from titin's A-band are known. Analysis of titin in the region of A77-A78 revealed conformationally defined interfaces possibly leading to local and higher order architecture accommodating molecular scaffold functions of this region of titin (Bucher et al., 2010). In similar fashion, crystal structure of A168-A170 revealed the molecular determinant for the recruitment of the ubiquitin-ligase MuRF1 onto titin (Mrosek et al., 2007). In summary, structural knowledge on A-band titin interactions with its ligands: myosin, Myosin Binding Protein C and MuRF would advance the understanding of clinical relevant A-band mutations associated with hereditary myopathy with early respiratory failure (Toro et al., 2013, Ohlsson et al., 2012, Hedberg et al., 2013). The 2200 residue-long M-line region of titin consists of kinase and 10 Ig domains linked with linker sequences of variable length. Structures are known for vast majority of ordered domains. Currently structures of only 5 Ig domains are not known. Out of numerous interactions formed by the titin M-line region the molecular basis is known only for M10 and obscurin-like 1, shedding some light into understanding of tibial muscular dystrophy and limb girdle muscular dystrophy 2J (Pernigo et al., 2010). Based on structure, a unique TK activation was inferred (Mayans et al., 1998) and structural data were used to propose a molecular pathomechanism for how mutation in TK causes hereditary myopathy with early respiratory failure (Lange et al., 2005). However, this mechanism is under heavy critique, as TK mutation was shown to be a benign concomitant genetic variant, whereas pathogenic mutation resides upstream in the A-band fibronectin domain (Hedberg et al., 2013, Pfeffer et al., 2013). Thus, some controversy surrounds the underresearched TK region. In particular nothing is known about the proposed MuRF1 and TK crosstalk (Centner et al., 2001, McElhinny et al., 2002) although the structures of MuRF1 binding site and TK are elucidated. Thus structural knowledge on the link between MuRF1 and TK might facilitate understanding of their functional crosstalk.

Table 1.2 Summary of published titin structures.

Region	Structure	Residues	References
Z-disc	**Z1Z2** (2A38;2F8V;1YA5)	1-196	Marino et al., 2006 Pinotsis et al., 2006, Zou et al., 2006
	Z-repeat (1H8B)	650-672	Atkinson et al., 2001
I-band	**I1** (1G1C)	2038-2125	Mayans et al., 2001
	I67-I69 (2RIK; 2RJM)	7211-7490[1]	von Castelmur et al., 2008
	I65-I70 (3B43)	7017-7584*	von Castelmur et al., 2008
	I91 (2RQ8;1WAA;1TIT;1TIU)	5253-5341	Improta et al., 1996, Stacklies et al., 2009, Yagawa et al., 2010
A-band	**A71** (1BPV)	14859-14961	Goll et al., 1998
	A77-A78 (3LPW)	15452-15646	Bucher et al., 2010
	A164-A165 (3LCY)	24032-24225	Chen et al., no publication
	A168-A169 (2J8H;2J8O;2ILL)	24430-24609	Muller et al., 2007, Mueller-Dieckmann et al., 2007
	A168-A170 (2NZI)	24430-24719	Mrosek et al., 2007
M-line	**TK** (1TKI)	24748-25067	Mayans et al., 1998
	M1 (2BK8)	25073-25166	Muller et al., no publication
	M4 (3QP3)	26350-26446	Sauer et al., no publication
	M5 (1NCT;1NCU;1TNM;1TNN)	26059-26155	Pfuhl et al., 1997, Pfuhl and Pastore, 1995
	M7 (3PUC)	26350-26446	Sauer et al., no publication
	M10 (3Q5O;2Y9R;2WP3;2WWK;2WWM;3KNB)	26828-26926	Sauer et al., no publication; Pernigo et al., 2010, Sauer et al., 2010

[1] Residue numbering according titin N2A isoform protein NP_596869.4, otherwise according reference entry NP_003310

1.2 Aims

In this work a structure-driven approach was undertaken to gain evidence for the discrimination between benign and pathogenic rare titin genetic variations and understand the possible molecular pathomechanism. To date no structural data is available on the ARVC associated titin T2850I mutation. Therefore it was aimed to elucidate structures of wild-type and mutant I10 domain in order to gain insights into possible pathomechanism. Moreover, a representative fragment of a constitutively expressed Ig-tandem would facilitate the functional understanding of these deviant I-band regions and form a solid basis for evaluation of future genetic variations. Work on M-line region of titin was focused on understanding of possible TK and MuRF crosstalk, as a rare genetic variant in this region was found to be associated with dilated cardiomyopathy. This complex scientific problem partitioned into two lines of work. Firstly, it was aimed to reassess the functionality of TK in order to solve controversies surrounding this issue. Secondly, it was intended to gain structural knowledge on the physical link between MuRF binding site and TK region to gain insights into possible mechanism of functional crosstalk and how mutation in this region might disturb it. Taken together, structural knowledge to be gathered in this work should specifically shed light on the pathomechanisms of studied disease-associated variants and would contribute to basic understanding how titin filament interconnects signaling pathways and structural components of sarcomere.

Chapter 2

Titin kinase is an inactive pseudokinase scaffold involved in MuRF1-titin interaction

2.1 Introduction

The giant protein titin (3-4.2 MDa according to isoform) is believed to orchestrate the response of muscle to mechanical and metabolic stress. Single titin molecules span entire half-sarcomeres (from Z-disc to M-lines, >1 μm in length) and contain strain compliant elements, forming an elastic lattice within the cytoskeleton of acto-myosin motors (Granzier and Labeit, 2005). Titin binds an extensive range of myofibrillar proteins, including Tcap/telethonin that have cardio-protective roles (Knoll et al., 2011), transcriptional regulators (Lange et al., 2005, Miller et al., 2003), and remodeling factors such as calpain proteases (Sorimachi et al., 1996, Ojima et al., 2010) and E3 ubiquitin ligases (Centner et al., 2001, Mrosek et al., 2007). These proteins link titin to the regulation of the membrane potential (Furukawa et al., 2001) and to protein turnover and gene expression processes in the sarcomere (Witt et al., 2008). Taken together, the elastic character of the titin chain and its multiple scaffolding interactions make it an optimal platform to integrate force sensing in the muscle cell (Granzier and Labeit, 2005).

The kinase domain near the C-terminus of titin (titin kinase; TK[2]) in the sarcomeric M-line plays an important role in mechanotransduction. TK binds a protein complex formed by the autophagosomal receptors nbr1, p62, and the E3 ubiquitin ligase MuRF2 that regulates protein degradation (Lange et al., 2005, Witt et al., 2008). A force-dependent regulation of this signalosome was revealed by the beating arrest of cardiomyocytes under hyperkalemic depolarization (Lange et al., 2005). The arrest induced the disassembly of the TK signalosome and the subsequent

[2] If not indicated otherwise, TK in this work refers to catalytic kinase domain with C-terminal regulatory tail.

translocation of MuRF2 to the cell nucleus, where it blocked the anabolic action of the serum response transcription factor (SRF). Nbr1 and p62 are *in vitro* substrates of TK (Lange et al., 2005), but it is unknown how their phosphorylation regulates the function of the signalosome. Intriguingly, a docking site for the ubiquitin ligase MuRF1 (a close homolog of MuRF2) has been mapped to a locus of titin immediately N-terminal to TK (Centner et al., 2001, Mrosek et al., 2007). MuRF1 is strongly upregulated by atrophic stimuli such as immobilization, denervation, nutritional deprivation, aging and in disease (*e.g.* cancer, sepsis and renal failure), being an important mediator of muscle wasting (Bodine et al., 2001, Mayans and Labeit, 2012). The exact signaling relationship of TK, MuRF2 and the vicinal MuRF1 remains unclear. However, the importance of TK for muscle physiology is demonstrated by the severe phenotypes resulting from its genetic defect. Both transgenic mouse models (Peng et al., 2005, Peng et al., 2007, Weinert et al., 2006) and human patients that express titins with TK deletions (Herman et al., 2012) or point mutations (Lange et al., 2005) display life-threatening myopathies. This might also reflect additional roles of TK in the myofibril, such as regulation of myofibrillogenesis that is exerted through phosphorylation of Tcap, a small protein of the Z-disc, initially identified as a TK substrate in differentiating myotubes (Mayans et al., 1998).

All proposed roles of TK in cell signaling assume a kinase activity, where phospho-transfer occurs in a stretch-regulated fashion. The crystal structure of TK (Mayans et al., 1998) showed that this kinase is inhibited by a C-terminal regulatory tail (CRD) that folds against the catalytic core, binding deeply into the ATP binding pocket and blocking it (**Figure 2.1**). In addition, the catalytic aspartate at the active site is blocked by an interaction with a tyrosine residue, Y170, from the P+1 loop. For TK activation, the steric blockage imposed by both Y170 and CRD need to be removed. Early studies (Mayans et al., 1998) indicated that Y170 inhibition is released by phosphorylation by a developmentally regulated kinase, but the latter has remained unidentified. More uncertain is the mechanism of CRD removal as biochemical activators that can displace this tail are yet to be found. However, based on atomic force microscopy data and molecular dynamics simulations, a mechanoactivation hypothesis has been proposed (Puchner et al., 2008, Grater et al., 2005, Puchner and Gaub, 2010, Stahl et al., 2011). This hypothesis postulates that

cytoskeletal stretch during myofibril function causes the CRD to unwind from the catalytic core, freeing TK to adopt a catalytically active conformation. This mechanosensory mechanism agrees with the proposed involvement of TK in stretch-activated pathways in muscle (Lange et al., 2005). For future progress in understanding TK function, the interplay between its scaffolding, catalytic and mechanosensory processes must be resolved.

Figure 2.1 Overall fold representation of TK

The catalytic kinase core is shown in blue with an accompanying surface representation. The C-terminal regulatory domain (CRD) is colored yellow and three major components: α-helix 1 (αR1), α-helix 2 (αR2) and β-stand 1 (βR1) are indicated. Note that αR2 helix binds deeply into the ATP binding cavity. The lysine residue central to ATP binding and catalysis (K36), the catalytic aspartate residue (D127) and the inhibitory tyrosine from the P+1 loop (Y170) are displayed.

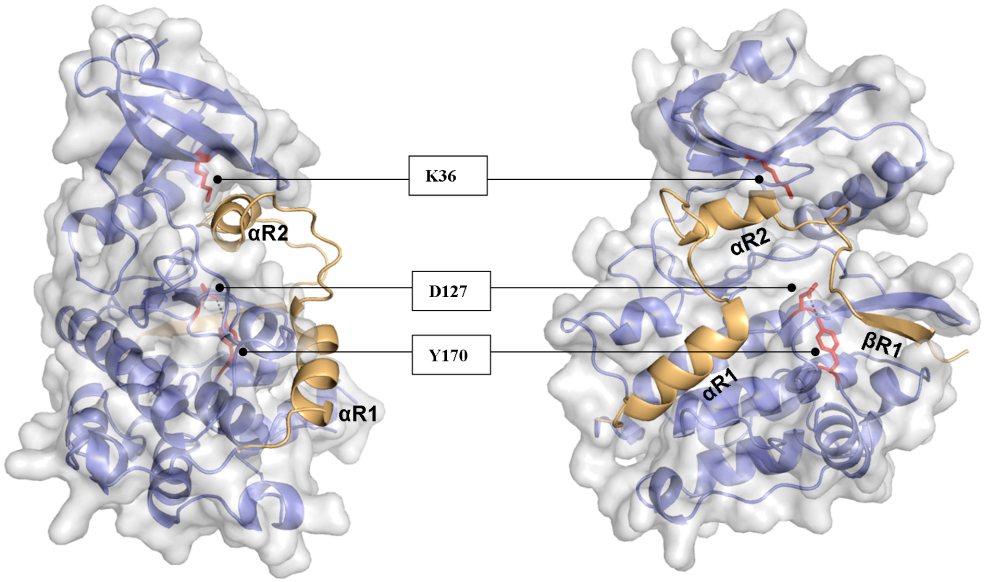

Here, we set out to profile the catalytic properties of TK making use of Tcap, its most established substrate. Unexpectedly, our structural and catalytic approaches have revealed that TK is an inactive pseudokinase. This result points to a new direction in understanding the role of TK in muscle signaling, where scaffolding and not kinase activity is to take centre stage.

2.2 Materials and Methods

2.2.1 Cloning

TK (residues 32172-32492; UniProtKB Q8WZ42) and its variants (TK^{K36A}, TK^{K36L}, TK^{Y170E}, $TK^{\Delta R2/Y170E}$) were cloned into the pET-Trx1a (former pETM-30) vector (EMBL collection) using NcoI and Acc65I restriction sites.. This vector fuses a His_6-tagged thioredoxin and a TEV (tobacco etch virus) protease cleavage site N-terminally to the target construct. For expression in Sf21 cells, the full-length protein encoded by the pET-Trx1a vector (Bogomolovas et al., 2009), including the N-terminal fusion, was cloned into pFastBac ET vector (EMBL). The NcoI compatible PscI site was introduced at the 5'-end of the construct and cloned into a linearized vector digested with NcoI/Acc65I restriction enzymes. The variant $TK^{\Delta R2/Y170E}$ was constructed by replacing residues 291-309 forming the regulatory a-helix R2 with the sequence GGSGGSA using TK^{Y170E} as a template. To ease structural annotation, residue 32172 is taken here as residue 1.

TwcK (twitchin kinase) (residues 6251-6537; UniProtKB Q23551) and its variants as well as full-length human Tcap (UniProtKB O15273) were cloned into the pETM-11 vector that adds a His_6-tag and a TEV protease cleavage site prior to the inserted protein. For compatibility with TK, residue 6251 in TwcK is considered here as 1 (based on the structural alignment in **Figure 2.8c**). GST tagged titin A168-170 (residues 31854- 32155), A168-TK (residues 31854-32492), TK and TK^{Y170E} were cloned into pETM-30 vector (EMBL collection). Mutations were introduced using overlap extension polymerase chain reaction. All constructs were verified by sequencing.

2.2.2 Recombinant protein production

Kinase samples were expressed in *E.coli* SoluBL21 (Genlantis) in TB medium supplemented with 50 mg/ml kanamycin. Cultures were grown at 37 °C to an OD_{600} = 1. Upon cooling to 16 ˚C, expression was induced with 0.2 mM IPTG and growth continued for further 18 hrs. Cells were harvested by centrifugation. The pellet was resuspended in lysis buffer (20 mM HEPES pH 8, 250 mM NaCl, 5 mM imidazole, 0.2% NP40, 2 mM β-ME, 2 mM PMSF), supplemented with DNAse I, lysozyme and 1 mM PMSF, and lysed by sonification. The supernatant was applied to a Ni^{2+}-NTA column (Qiagen) pre-equilibrated in lysis buffer and proteins eluted with 300 mM imidazole in lysis buffer without detergent. Tag removal was by incubation with TEV protease in 25 mM Tris pH 8, 50 mM NaCl, 5 mM DTT, overnight at RT. Proteins were further purified using ion exchange chromatography (HiTrap SP for TK; HiTrap Q for TwcK) and gel filtration on a Sephadex S75 16/60 column (GE Healthcare). Samples were stored at 4 ^{o}C until further use.

Tcap was produced as TwcK but without tag removal or gel filtration. GST-tagged proteins were purified using Glutathione-Sepharose (GE lifesciences) resin.

For eukaryotic TK expression (Protein Expression and Purification Facility of EMBL), Sf21 cells were transfected with the bacmid DNA construct of TK or its variants according to manufacturer instructions (Invitrogen Bac-to-Bac system). Transfected cells were incubated for 3 days at 27 °C and the supernatant, containing recombinant virus, was collected. Amplified virus (10 ml) was added to 1×10^6 Sf21 cells and incubated at 27 °C for 3 days. Sf21 cells were harvested 72 hrs postinfection and stored at -20 ^{o}C until protein purification, which followed the procedure above.

2.2.3 Protein stability measurement

Energy changes (ΔΔG) for the replacement of lysine K36 in the ATP-binding pocket with each possible amino acid type were estimated using FoldX (Van Durme et al., 2011). Experimental protein stability for selected mutated variants was estimated from differences in their melting temperature (Tm) monitored by

Differential Scanning Fluorimetry (DFS). DFS measurements were performed using a Mx3005p RT-PCR machine (Stratagene). Purified TK, TK^{K36A} and TK^{K36L} samples were assayed in 25 µl buffer consisting of 10 mM HEPES pH 7.5, 150 mM NaCl in 96-well plates. SYPRO-Orange (Invitrogen) was added at a dilution 1:1000. Fluorescence was monitored (λex = 465 nm, λem=590 nm) from 25 °C to 85 °C at 1 °C/min increment. Each measurement was done in triplicate and Tm values determined using a modified Boltzmann equation with linear correction of baseline drifts (Matulis et al., 2005).

2.2.4 Crystal structure determination

As previously (Mayans et al., 1998, Mayans and Wilmanns, 1999), crystals were grown at 21 °C by the hanging-drop method in 24-well VDX plates (Hampton Research). Drops contained 1 µl protein solution (12 mg/ml) and 1 µl reservoir consisting of 1.6 M Na/K tartrate, 25 mM sodium acetate pH 4.9, 25 mM imidazole pH 7.5, 2.5% PEG 400. Crystal optimization used seeding into solutions with 1.2 M Na/K tartrate but of otherwise identical composition. For data collection, crystals were flash frozen in liquid nitrogen using mother liquor supplemented with 30% [v/v] glycerol. X ray diffraction data were collected at 100 K on beamline I04, DIAMOND (Didcot), at a λ = 0.9763 Å on a ADSC Quantum detector. The data were processed with XDS/XSCALE (Kabsch, 2010) (**Table 2.1**). As before, crystals contained two molecular copies in the asymmetric unit (rmsd=0.14 Å, in MUSTANG (Konagurthu et al., 2006)). Phasing was by molecular replacement in Phaser (McCoy et al., 2007) using one copy of eukaryotic TK (PDB entry 1TKI) as a search model. Model refinement and solvent building was in PHENIX (Adams et al., 2011), applying simulated annealing with a starting temperature of 5000 °C. Manual building was in COOT (Emsley et al., 2010). Coordinates and structure factors have been deposited with the PDB (entry 4JNW).

2.2.5 *In vitro* phosphorylation assays

Phosphorylation assays were performed in 20 µl assay buffer (20 mM Tris-HCl pH 7.4, 10 mM magnesium acetate, 0.05% NP40, 0.1 mM DTT, 0.2 mg/ml acetylated BSA) containing 0.4 mM ATP (0.2 µCi/reaction of [γ-^{33}P]ATP) at 30 °C. Tcap, MLC-derived peptide (KKRARAATSNVFS), Tcap-derived peptide (RRSLSRSMSQEAQRG), casein and myelin basic protein were tested at 4 µg/reaction. Where indicated, the reaction mixture was supplemented with 0.5 mM $CaCl_2$ and 0.4 µg/reaction calmodulin from bovine testis (Sigma-Aldrich). For reaction mixtures that assayed peptide substrates, an aliquot was withdrawn at indicated time points and spotted on EDTA impregnated P81 phosphocellulose paper (Whatman). The latter was washed extensively with 75 mM orthophosphoric acid and once with ethanol, dried and exposed to a phosphoscreen. Reaction mixtures with protein substrates were first separated on SDS-PAGE, the gel briefly stained, dried and exposed to the phosphoimager screen. Screens were imaged with a Fujifilm BAS 2500 phosphoimager and images processed using AIDA (Raytest).

2.2.6 Preparation of inactivated C2C12 extracts

C2C12 cells were grown on gelatin coated plastic flasks in DMEM, 10% fetal calf serum, 1x ITS, penicillin, streptomycin. For differentiation, the medium was changed to DMEM, supplemented with 2% horse serum and penicillin/streptomycin once the cells reached 70-90% confluence. For FSBA extract inactivation, cells were lysed in 50 mM Tris pH 7.4, 150 mM NaCl, 1% NP-40. Clarified lysate was depleted of endogenous ATP on a desalting column (GE Lifesciences) and treated with 20 mM FSBA at 30 °C for 1 hr. FSBA was removed by buffer exchange into phosphorylation assays buffer (above) supplemented with 5 mM DTT.

2.2.7 Pull-downs using recombinant titin fragments on muscle extracts

Quadriceps tissue from adult mice was pulverised under liquid nitrogen and the powder homogenized in 20 mM Tris pH7.5, 100 mM NaCl, 2 mM b-ME and Complete Protease Inhibitor (Roche). Extraction proceeded for 90 min on ice. The resulting extracts were clarified at 3000g for 30 min, aliquoted, frozen in liquid nitrogen and stored at -80 °C.

For GST pull-downs, 50 µg each of GST, GST-A168-170, GST-A168-TK, GST-TK and GST-TK^{Y170E}, were immobilized on 30 µl of Glutathione-Sepharose-beads and washed with PBS, 0.1% NP40. Extracts were thawed on ice and spun for 1 min at 21000xg. The supernatant was diluted by adding 3 volumes of PBS, 0.1% NP40. Next, 1 ml of diluted extract was mixed with 30 µl of beads loaded with a given titin-fragment and incubated for 16 hrs at 4°C under light stirring. Mixtures were spun for 1 min at 1000g, supernatants were removed and the beads washed 3x with 1 ml PBS, 0.1% NP40. After a final wash with PBS, supernatants were removed and the beads resuspended in SDS sample buffer. Bound material was examined by SDS-PAGE and Western-blotting using a MuRF1 specific antibody.

2.2.8 Filter Binding Assay

Purified His_6-MuRF1-coiled coil (aa169-263, Q969Q1; reported in Mrosek et al.) was biotinylated with NHS-PEG_4-Biotin (Thermo Scientific). To remove unreacted biotin, the sample was filtered twice through a PD-10 column (GE Healthcare) in PBS. 1 mM DTT and 50% glycerol were added and the sample frozen until further use.

Purified titin constructs were spotted (approx. 1 µg) on nitrocellulose membranes pre-wetted with TBS (25 mM Tris pH 7.5, 150 mM NaCl). The filter was blocked by TBST/5% milk, washed with TBST (TBS + 0,05% Tween 20) and incubated for 3 hrs with biotinylated MuRF1 coiled-coil at a concentration of 0.5

µg/ml in TBST/1%milk. The membrane was washed in TBST and incubated for 1 hr in TBST containing 2 µg/ml streptavidin conjugated to alkaline phosphatase (Thermo Scientific). After washes in TBST and a final wash in TBS, the detection with NBT/BCIP was done as described by the supplier (Roche).

2.3 Results

2.3.1 Preparations from insect cells contain a contaminant Tcap phosphorylating activity

We tested the activity of TK samples (comprising the catalytic kinase core and CRD) on the Tcap substrate by expressing three TK variants in Sf21 insect cells: wild-type TK, the activated phosphomimic TK^{Y170E}, and the constitutively inactive TK^{K36L} (mutated residues illustrated in **Figure 2.1**). In TK^{Y170E}, the mutation removed the inhibition of the catalytic aspartate by the tyrosine residue in the P+1 loop. This sample has been previously reported to be active (Mayans et al., 1998, Zou et al., 2003) In TK^{K36L}, the highly conserved lysine residue involved in the coordination and processing of ATP was mutated into an unreactive leucine group that abolishes catalysis. Mutation of this lysine residue into *e.g.* alanine, histidine, methionine or isoleucine is an established method to generate inactive kinases (Gloeckner et al., 2006, Iyer et al., 2005, Ling et al., 1999, Shaw et al., 2004). Although mutation to alanine is most common, in TK this exchange resulted in certain structural instability. Using FoldX (Van Durme et al., 2011) and Differential Scanning Fluorimetry to measure sample melting curves, we identified leucine to be well tolerated by the TK fold (**Figure 2.2**). Thus, TK^{K36L} was used throughout this work.

Figure 2.2 Stability of TK lysine mutants
a. Energy changes (ΔΔG) for the replacement of lysine K36 by every other amino acid calculated using FoldX. The values confirm observations that the conventional replacement of K36 to alanine is poorly tolerated leading to the destabilization of the N-terminal lobe of the TK fold. A replacement of this residue by leucine, however, is predicted to agree well with the structure of TK; **b.** DSF denaturation traces recorded at λ_{em}=590 nm. Substitution of K36 for alanine (TK^{K36A}) had a clear destabilizing effect (DTm= 6.6 °C) on TK, whereas the stability of TK^{K36L} (DTm= 2.2 °C) was approximately equivalent to that of wild-type TK.

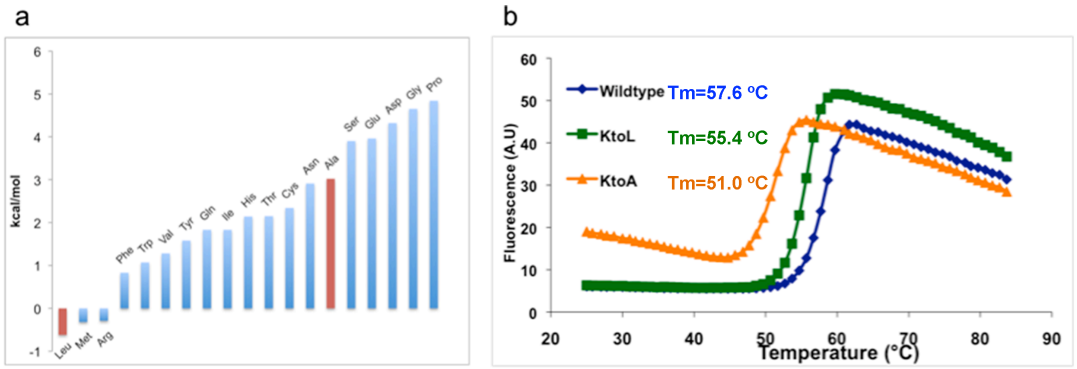

In activity assays that used ATP[γ-^{33}P], all three TK variants – including the inactive TK^{K36L} – showed similar phospho-transfer activities on Tcap and were modestly stimulated by Ca^{2+}/calmodulin (**Figure 2.4a**). As an independent validation, we studied the activity of immuno-complexed wt-TK where its active site had been blocked by a specific antibody directed against the P+1 loop (the efficient complexation of TK by this antibody is shown in **Figure 2.3**).

Figure 2.3 Dot blot assays of anti-TK and anti-MuRF1 antibodies. anti-MuRF1 antibodies (**a**) recognize the spotted MuRF1 sample, but not the TK constructs, whereas anti-TK antibodies recognize TK, but not MuRF1 or titin Ig/Fn3 domains (titin sample). Antibodies were produced against the synthetic P+1 loop peptide (TK) or the recombinant protein (MuRF1) in rabbits and purified using the immobilized antigens.

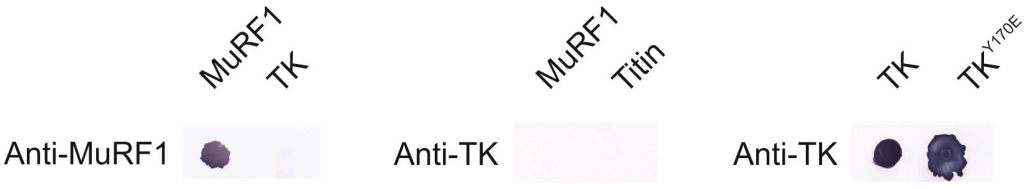

Immuno-complexed TK, non-complexed TK samples, and non-treated TK controls showed similar levels of activity (**Figure 2.4b**). Hence, both activity data from mutated and immuno-complexed TK samples suggested that the insect cell preparations catalyzed Tcap phosphorylation in a TK-independent way, with kinase activity arising from other component(s) in the cell milieu.

Figure 2.4 Tcap phosphorylation assays using TK preparations from insect cells
a. Preparations of wild-type TK, the activated TKY170E phosphomimic and the constitutively inactive TK^{K36L} phosphorylate Tcap comparably and stimulated by Ca^{2+}/calmodulin. SDS-PAGE (left) and autoradiogram (right) are shown; **b.** Phosphorylation assay of TK sterically inhibited by immuno-complexation with an antibody raised against the P+1 loop vicinal to the active site. An antibody (anti-MuRF1) that does not complex TK is included for comparison; **c.** Untransfected Sf21 cell extracts supplemented with Tcap (but not Ca^{2+}/calmodulin) display phosphorylating activity (the stimulation of catalysis upon addition of calmodulin was ~25%, this modest activation is likely due to the presence of endogenous calmodulin in the extract). SDS-PAGE (left) and autoradiogram (right) revealing Tcap phosphorylation; **d.** Segregation of phosphorylating activity (cyan) and TK presence (red) during purification. Sf21 cell crude extract containing the recombinant TK^{K36L} was filtered through a Ni^{2+}NTA column. Bound proteins were eluted with a linear gradient of imidazole (100% buffer B=0.3 M imidazole; green line) and monitored by A_{280}; the resultant chromatogram is in blue. The content of TK^{K36L} in eluted fractions was determined by spot-blot immunoassay using anti TK P+1 loop antibody. The amount of colored product quantified densitometrically was proportional to the amount of TK^{K36L} in each fraction (red). Phosphorylation of a Tcap-derived peptide substrate in the presence of calmodulin was quantified in each fraction densitometrically by standard phosphorylation assay that used [γ-^{33}P]ATP and spotting on P81 paper (cyan). The data show that Tcap phosphorylation segregated from TK^{K36L}.

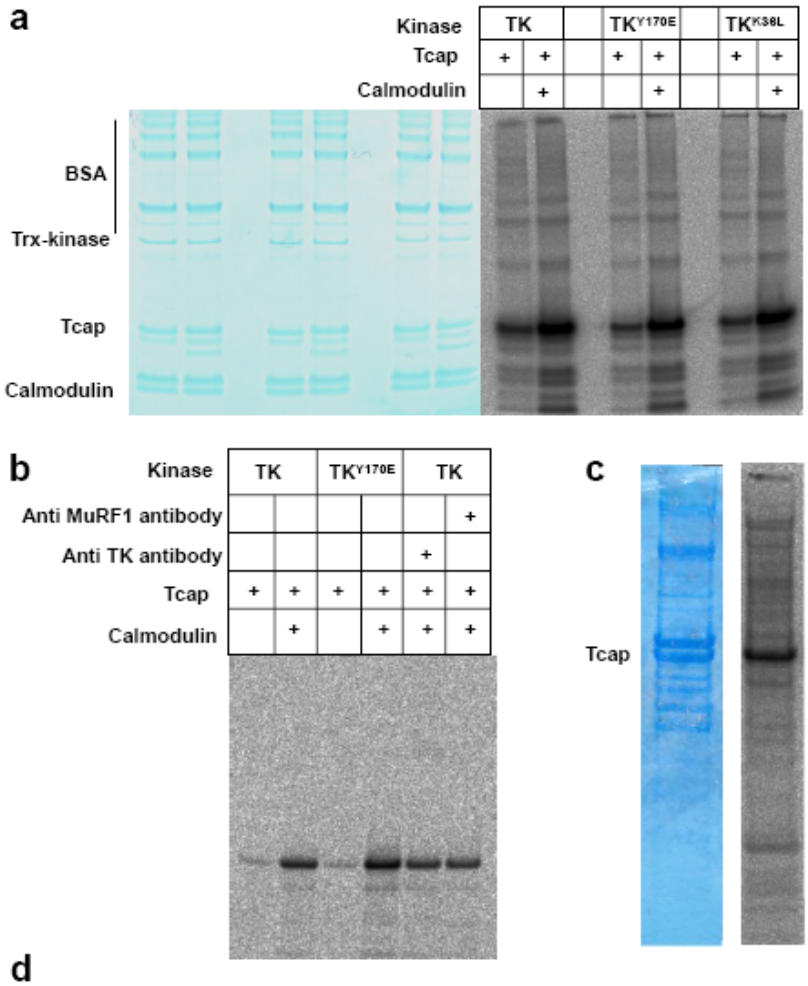
a
Kinase
TK
TK^Y170E
TK^K38L
Tcap
Calmodulin
BSA
Trx-kinase
Tcap
Calmodulin
b
Kinase
TK
TK^Y170E
TK
Anti MuRF1 antibody
Anti TK antibody
Tcap
Calmodulin
c
Tcap
d
TK concentration (AU)
A280 (mAU)
Buffer B (%)
Tcap phosphorylating activity (AU)
Elution (ml)

Further evidence that the observed catalysis resulted from a contaminant kinase was derived from TK purification. Recombinant TK segregated from the Tcap phosphorylating activity during fractionation (**Figure 2.4d**) and phospho-transfer activity on Tcap decreased progressively as TK purity increased. The resulting highly pure TK samples showed 80-fold less activity than initial preparations (**Figure 2.5**). The existence of such contaminating kinase activity was finally confirmed by assaying non-transfected Sf21 cell extracts, which displayed notable phosphorylation of Tcap (**Figure 2.4c**). Efforts to identify the contaminant kinase during this work were not successful. Although a protein candidate could be isolated (**Figure 2.5**), Sf21 cells originate from *Spodoptera frugiperda* whose genome is not sequenced, impeding the identification of proteins through proteomic methods. In brief, these data show that Tcap is a substrate of endogenous kinases in Sf21 cells.

Fig 2.5 Phospho-transfer activity does not segregate with TK in purification
In vitro Tcap phosphorylation assays using **a.** partially purified TK samples after one-step affinity chromatography and **b.** TK samples thoroughly purified using the three-step chromatography protocol described in Methods. Both a. and b. show: Coomassie stained SDS-PAGE of reaction mixture (left), autoradiogram of phosphorylated samples (center) and SDS-PAGE of the TK sample prior to being added to the reaction mixture (right). A same amount of total protein content (as estimated using A_{280}) was used in both experiments; **c.** Densitogram showing a quantification of Tcap phosphorylation according to autoradiograms. The quantitation shows that purified TK samples displayed 80-fold less phosphor-transfer activity than partially pure TK samples. A contaminant (red pointer) co-purifies with TK at low levels. We speculate that this is the likely kinase acting on Tcap. Efforts to identify this protein through proteomic approaches were not successful as the genome of *Spodoptera frugiperda* is not available.

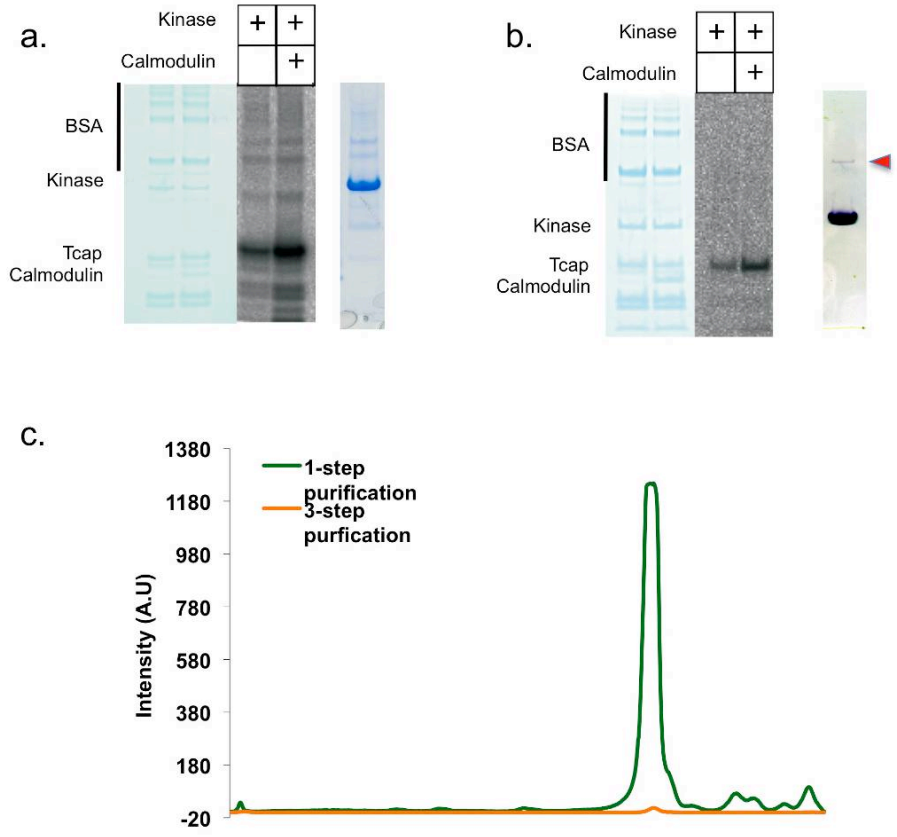

2.3.2 TK produced in *E.coli* is catalytically inactive

Since kinases present in insect cells preparations masked the potential catalysis of TK on Tcap, we established the over-production of TK in *E. coli*. To validate that the bacterial form of this sample was viable, we performed a mass spectrometry analysis of TK samples from *E. coli* and Sf21 cells. The data confirmed that neither of the proteins was truncated or otherwise chemically compromised (*e.g.* ΔMM from full mass theoretical values of TK^{Y170E} from Sf21 and E.coli cells was +0.7 Da and +1.8 Da, respectively). The bacterially expressed TK had no phospho-transfer activity on Tcap or on the universal kinase substrates myelin basic protein and casein. This agrees with previous observations of inactivity of bacterial TK (Puchner et al., 2008). To test whether the lack of catalysis resulted from fold defects in the bacterial sample, we elucidated its crystal structure to 2.06 Å resolution (**Table 2.1**). Noteworthy, crystals of eukaryotically expressed TK belonged to space group $P2_12_12_1$ with cell dimensions 78.61 Å, 89.77 Å, 113.32 Å and diffracted to 2.0 Å resolution (Mayans et al., 1998, Mayans and Wilmanns, 1999). That lattice and the one of bacterially-expressed TK in this study are identical.

Crystallization used previous protocols for Sf9-expressed TK (Mayans and Willmans, 1999) and crystals reproduced the lattice parameters of the latter (Mayans et al., 1998). Following bias removal by simulated annealing, the resulting model of bacterially-produced TK was in complete agreement with that of Sf9-expressed samples (rmsd=0.29 Å for all Cα atoms, calculated with MUSTANG; Konagurthu et al., 2006) (**Figure 2.6a**). These data confirmed that there are no noticeable molecular differences between bacterial and eukaryotic forms of TK and that the absence of catalysis on Tcap signifies that Tcap is not a substrate of TK.

Figure 2.6 Structural and functional characterization of TK produced in *E.coli*

a. Superimposition of the crystal structures of TK expressed in bacteria (red) and insect cells (PDB entry 1TKI) (blue). The overall RMSD for C_a atoms is 0.29 Å; **b.** Representation of the activated variant $TK^{\Delta R2/Y170E}$, where the deleted fraction is in grey and the added loop is shown schematically in red. The sequence exchanges in this variant are shown below; **c.** Identification of potential TK substrates in differentiating C_2C_{12} cell extracts depleted of endogenous kinases by treatment with FSBA. Protein kinase A (PKA) was used as positive control. Autoradiogram (panel c) and densitogram of phospho-image (lower panel) are provided. The data show no significant differences in labeling pattern when comparing cell extract alone or supplemented with activated forms of TK.

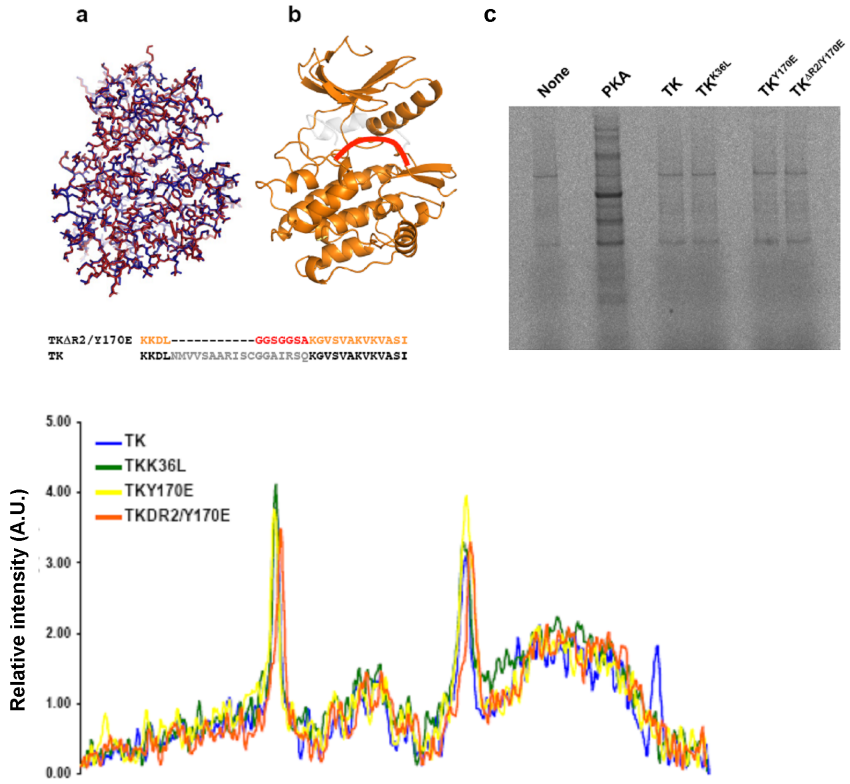

We then examined whether muscle cell extracts contain substrates for the bacterially expressed and highly purified TK preparations by performing phosphorylation assays using wt-TK and TK^{Y170E} on extracts from differentiating murine C_2C_{12} myocytes (day 2) as well as gastrocnemius muscle from adult mouse (the extracts were depleted from endogenous kinase activities using FSBA). This

work did not reveal candidate TK substrates (**Figure 2.6c**). To test whether this result reflected tight TK auto-inhibition, we designed the variant $TK^{\Delta R2/Y170E}$, where the inhibition of the ATP-binding pocket by the regulatory βα-helix R2 of the CRD had been removed (nomenclature as in **Figure 2.1**). In $TK^{\Delta R2/Y170E}$, helix R2 was substituted by a flexible loop that links helix R1 to the C-terminal b-strand R3 (**Figure 2.6b**). As before, assaying this dually activated variant did not reveal any candidate substrates in cell extracts (**Figure 2.6c**). These results suggest that inactivity is a genuine characteristic of TK.

Table 2.1 Data collection and refinement statistics

	TK
Data collection	
Space group	$P2_12_12_1$
Cell dimensions	
a, *b*, *c* (Å)	78.86, 89.73, 113.88
Resolution (Å)	28.9-2.06 (2.1-2.06)
No. reflections	49667 (2681)
R_{sym}(I) (%)	9.1 (56.2)
$I / \sigma I$	13.9 (3.6)
Completeness (%)	97.9 (95.4)
Redundancy	5.7 (5.3)
Refinement	
Resolution (Å)	28.98-2.06
R_{work} / R_{free} (%)[b]	16.63 / 20.37
No. atoms	
Protein	5235
Ligand/ion	28
Water	469
B-factors (A^2)	
Protein	22.8
Ligand/ion	48.4
Water	30.7
R.m.s. deviations	
Bond lengths (Å)	0.007
Bond angles (°)	1.000

2.3.3 TK contains atypical residues in its catalytic motifs

To explore the molecular basis of the apparent inactivity of TK, we examined the sequence composition of its active site. A multiple sequence alignment of TK sequences **(Appendix 2)** revealed consistent deviations from canonical active motifs: namely, the bulky hydrophobic residue methionine in position 2 of the V<u>A</u>IK motif and a glutamate in the <u>D</u>FG motif. The canonical VAIK motif (Boudeau et al., 2006, Endicott et al., 2012) is located in strand-β3 and contains the catalytic lysine that ion-pairs the non-transferable α- and β-phosphates of ATP. There is a strong selection for small hydrophobic residues, such as alanine or valine, in position 2 of the VAIK sequence. This residue forms the bottom of the cavity that accommodates the purine heterocycle moiety of ATP. A bulky residue at this position, as methionine in TK, might sterically hinder ATP binding or lead to a non-catalytically viable binding mode. The latter case appears likely as AFM studies of TK unfolding in the presence of ATP suggest that binding occurs (Grater et al., 2005, Puchner et al., 2008). This deduction also agrees with studies on B-Raf where substitution of that residue with methionine did not abolish ATP binding (Taylor et al., 2013), and with findings on JAK2, which has a leucine residue in this position and binds ATP in an unconventional way (Bandaranayake et al., 2012). Interestingly, in those rare cases where TK sequences deviate from the methionine residue at this position, they always contain leucine instead, supporting the view of a deviant ATP binding mode (**see Appendix 2**). In the DFG motif, aspartate chelates the magnesium ion that coordinates the β- and γ-phosphates of ATP. This residue is conserved across most members of the protein kinase-like superfamily (Scheeff and Bourne, 2005). Although glutamate and aspartate are chemically similar, this substitution is sufficient to inactivate phospho-transfer in kinases (Brown et al., 1995, Schu et al., 1993). In the human kinome (Scheeff et al., 2009), the deviant residues found in TK are extremely rare among active kinases **(Figure 2.7)**. TK is the only known human kinase that contains glutamate instead of aspartate in the DFG motif, while ATR kinase is the only other human kinase containing a methionine in position 2 of the VAIK motif, although its level of activity is unclear. In contrast, among pseudokinases there is no marked selection for given residues in position 2 of the VAIK motif or aspartate in the DFG signature. Thus, the YMAK/EFG signatures clearly point to irregular catalytic

properties in TK.

Figure 2.7 TK contains atypical residues in catalytic motifs.
a. Distribution of residues in position 2 of the VAIK motif and position 1 of the DFG motif in protein kinases of the human kinome. The classification of kinases and pseudokinases was taken from (Scheeff et al., 2009). TK, the only human kinase containing an EFG motif, is misclassified as an active kinase due to previous reports of catalysis on Tcap (Mayans et al., 1998, Zou et al., 2003, Lange et al., 2005). Other kinases with deviant catalytic motifs are: CASK (GFG motif); ATR (xMxK motif); LMR2, NEK8 and RIPK1 (IxK); DNAPK, FRAP and SMG1 (LxK); **b.** Commonly occurring residues in the VAIK and DFG motifs of titin kinases from vertebrate (upper) and invertebrate titin-like kinases (lower). Sequences for representative kinases of each group are given in **Appendix 2**.

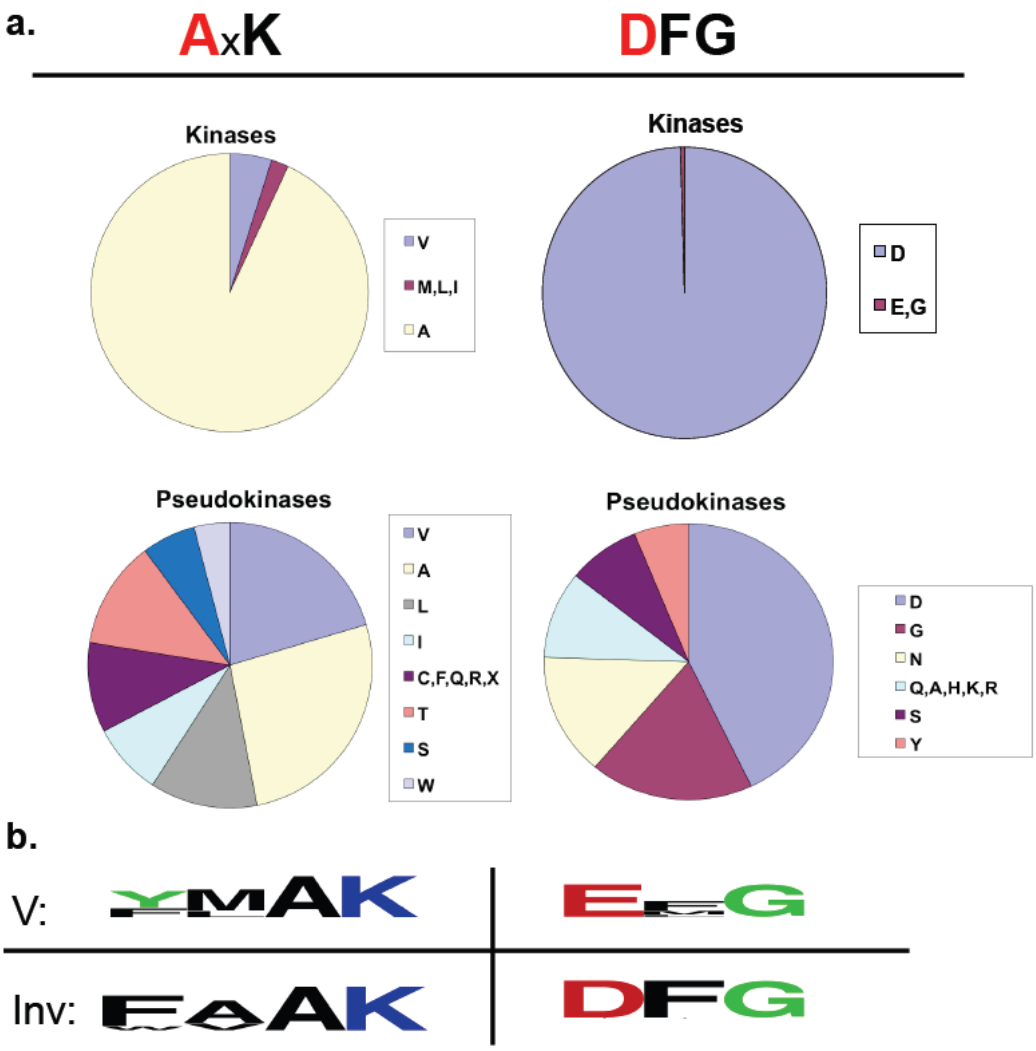

Interestingly, an exploration of sequences of TK-like kinases from invertebrates that included twitchin and TTN-1 kinases from nematodes and mollusks, and projectin from insects showed that these homologs contain canonical catalytic motifs characteristic of active kinases (**Appendix 2**). In agreement, the twitchin kinases from *Aplysia* and *C. elegans* exhibit high levels of catalysis (Heierhorst et al., 1996, Lei et al., 1994, von Castelmur et al., 2012). This suggests an evolutionary dichotomy where invertebrate members of the TK family are functional enzymes, but the vertebrate counterparts are inactive pseudokinases.

2.3.4 Transfer of YMAK/EFG TK signature motifs to twitchin kinase abolishes catalysis

To study the role of the atypical, conserved methionine and glutamate residues in the active site of TK, we introduced these residues into twitchin kinase from *C. elegans* (*ce*TwcK). The latter is a close homolog of human TK that is well characterized structurally and biochemically (Heierhorst et al., 1996, Lei et al., 1994, von Castelmur et al., 2012). *ce*TwcK (bacterially expressed) exhibits elevated levels of catalysis when assayed on a model peptide substrate derived from myosin light chain (MLC) protein. *ce*TwcK and TK share high conservation (34% sequence identity; **Figure 2.8c**) and structural similarity (rmsd for C_α atoms = 1.29 Å when comparing the structure of TK in this work and PDB entry 3UTO using MUSTANG, Konagurthu et al., 2006) (**Figure 2.8a**). The active sites of these two kinases are in close structural agreement, particularly their ATP binding pockets, their β3 strands and the $^{D}/_{E}$FG motifs (**Figure 2.8b**). Thus, we concluded that *ce*TwcK is a suitable template to investigate the effect of the unusual motifs of TK on catalysis.

Based on this proviso, the mutations A34M and/or D147E were introduced in *ce*TwcK (variants *ce*TwcK^{A34M}, *ce*TwcK^{D147E}, *ce*TwcK$^{A34M/D147E}$) and phosphorylation assays carried out on the MLC-derived peptide substrate. The double mutant *ce*TwcK$^{A34M/D147E}$ was generated to account for the possible compensatory co-evolution of these substitutions in TK. In contrast to wild-type *ce*TwcK, that showed its characteristically high activity, all generated mutants lacked measurable phospho-transfer catalysis (**Figure 2.8d**). To confirm that this result was not due to

unsuspected distortions of the active site of *ce*TwcK caused by the mutations, we generated the variant *ce*TwcK^{A34V} as positive control. In this construct, the alanine in the VAIK motif is replaced by a valine residue, which is found in the catalytically active TwcKs from mollusks (**Appendix 2)** as well as 5% of the active members of the human kinome (Scheeff et al., 2009) As expected, *ce*TwcK^{A34V} retained noticeable levels of catalysis (**Figure 2.8e**). These results indicate that the two atypical active site residues M34 and E147 in TK are sufficient to inactive it into a pseudokinase state.

Figure 2.8 Comparison of TK and TwcK active sites.
a. Structural superimposition of TK and *ce*TwcK (PDB entry 3UTO). Ribbon thickness and coloring correlate with the rmsd values of the superimposition as given in the accompanying scale (minimum, maximum and average values are shown). The structural agreement is excellent overall including active site regions, divergences only occur in peripheral loop areas; **b**. Detailed comparison of the ATP binding pockets of TK (green) and *ce*TwcK (pink) (numbering corresponds to TK). Boxed labels indicate TK residues that were trans-engineered into *ce*TwcK; **c**. Structure-based sequence alignment of human TK and *ce*TwcK corresponding to the superimposition displayed in a. and b. The canonical composition of functional motifs is shown in red, the P+1 loop is boxed and the tyrosine residue undergoing phosphorylation in TK is indicated with an asterisk; **d**. Comparative autoradiogram of catalysis by *ce*Twck and its variants TwcK^{A34M}, TwcK^{D147E} and TwcK$^{A34M/D147E}$ carrying TK residues in their ATP binding pockets. The time course shows phosphorylation of a MLC-derived peptide; **e**. Comparative autoradiogram of the catalysis from *ce*Twck and TwcK^{A34V}. The latter carries the non-inactivating valine residue commonly found in the ATP binding pocket of TwcK from molluscs

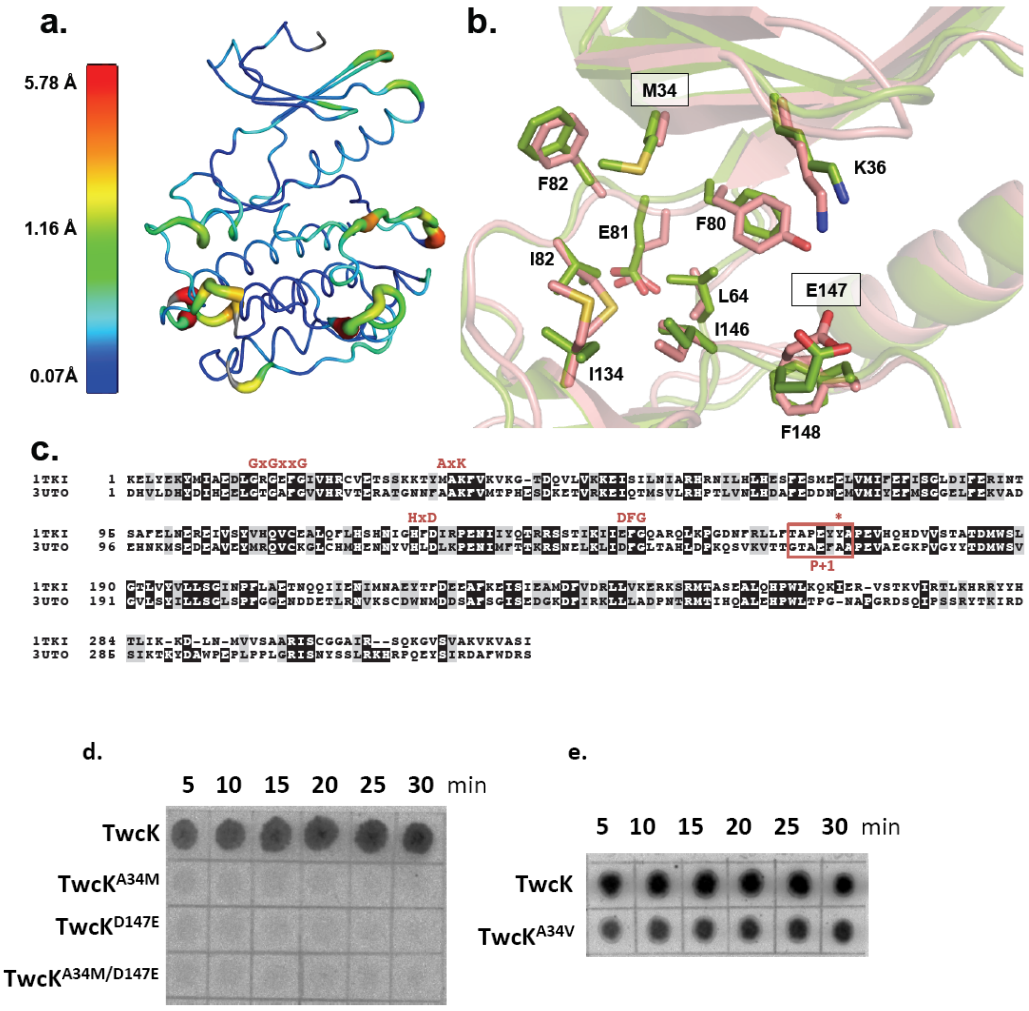

2.3.5 TK supports the interaction of M-line titin with the atrogin MuRF1

Based on these findings, we reassessed how TK might contribute to muscle signaling in non-catalytic ways. The binding of the muscle-specific E3 ubiquitin ligase MuRF1 in the immediate vicinity of TK is well documented (Centner et al., 2001, Mrosek et al., 2007). MuRF1 binds a tandem of Ig-Ig-Fn domains, A168-A170, immediately preceding the TK domain. The binding is mediated by the C-terminal helical domain of MuRF1 and determined by the presence of a loop with sequence KTLE in the titin domain A168 (Mrosek et al., 2008). Here, we generated titin constructs comprising variations of the established MuRF1 docking site as well as TK. A168-A170 and its C-terminally truncated variant A168A-A169 showed capable of binding MuRF1; while the loop mutant A168-A170$^{\Delta KTLE}$ (where the KTLE motif had been mutated into a AAAA sequence), N-terminally truncated A169-A170 and the single A169 domain (**Figure 2.9**) did not display detectable interaction. Interestingly, when the fragment A169-A170 (which does not bind MuRF1 with detectable affinity) was extended to include TK, MuRF1 binding was restored and stronger than observed for the established A168-A170 locus (**Figure 2.9a**). It is worth noticing that the concentration of A169-TK was 10 times lower than that of the other constructs in the assay, indicating that TK markedly boosts the MuRF1 interaction.

We further confirmed these findings via pull-down assays on skeletal muscle extracts (**Figure 2.9b**). Here, A168-A170 and A168-TK were able to pull-down the endogenous MuRF1 but, as before, the sample containing TK showed a stronger binding. Neither TK alone (either as wild-type or Y170E phosphomimic) nor the core domain A169 alone interacted with MuRF1 detectably (**Figure 2.9a**). This indicates that the MuRF1 docking site in M-line titin spans the region A168-TK, which constitutes an extended multi-domain scaffold of approx. 18-20 nm length. This length agrees well with the predicted dimensions of the helical domain of MuRF1, which is thought to fold into a long coiled-coil (Mrosek et al., 2007). Our data suggest that individual titin domains (or their interfaces) in this binding locus contribute differently to the affinity of the interaction, where a crucial high affinity locus is located at the A169-TK junction that is likely to play a dominant role in the recruitment and retention of MuRF1 in the sarcomeric M-line.

Figure 2.9 Dissection of TK/MuRF1 molecular interactions.
a. Identification of the MuRF1-titin interaction region by filter binding assay. The helical domain of MuRF1 interacts with its established docking site A168-A170 and the C-terminally truncated version A168-A169, but not with the loop mutant A168-A170$^{\Delta KTLE}$, the N-terminally truncated A169-A170 or the single domain A169. Binding to A169-A170 is restored and enhanced when TK is included in the construct (A169-TK); **b.** Pull down assay using skeletal muscle extract demonstrates that A168-A170 and A168-TK bind endogenous MuRF1 efficiently, but that the binding is stronger in the presence of TK. Neither GST nor TK alone are capable to pull down endogenous MuRF1.

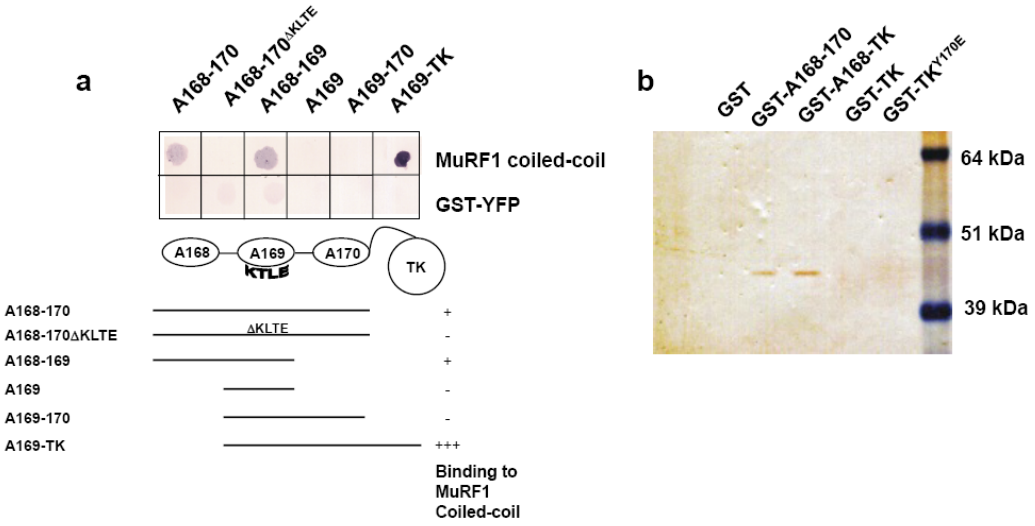

2.4 Discussion

The signaling context of TK in the sarcomere has remained elusive since its discovery over two decades ago (Labeit et al., 1992). Efforts to identify activators and substrates of this kinase have only yielded candidates of unclear physiological relevance. Three sarcomeric proteins have been proposed to be phosphorylation substrates of TK: Tcap (Mayans et al., 1998), nbr1 and p62 (Lange et al., 2005). Nbr1 and p62 elicit weak catalysis *in vitro*, seemingly unrelated to their function in the TK-signalosome (Lange et al., 2005). In contrast, Tcap induces notable levels of phosphorylation, being TK's best established substrate. However, Tcap is known to anchor titin in the Z-disk, cross-linking the N-termini of two neighboring titin molecules (Zou et al., 2006) and further connecting titin to MLP and minK associated stretch signalling (Knoll et al., 2011, Furukawa et al., 2001). In the sarcomere, this Tcap-based assembly in the periphery of the Z-disk is approx. 1 μm away from TK in the M-line. The non-diffusible nature of both enzyme and substrate led to question the *in vivo* significance of the interaction. Here, we provide now evidence that TK is an inactive pseudokinase and Tcap an unlikely substrate. Our data compile the testing of wild-type TK, active phosphomimics (TK^{Y170E}, $TK^{\Delta R2/Y170E}$) and inactivated variants (TK^{K36L}) expressed in Sf21 eukaryotic cells and in the *E. coli* bacterial system. These TK forms were assayed for activity on Tcap as well as on inactivated extracts from developing myocytes and mature muscles. This did not reveal catalysis that could be attributed to TK, suggesting that TK was incapable of carrying out phospho-transfer. Structurally, we attributed this fact to two atypical residues, M34 and E147, that are conserved in vertebrate TKs. Each of those residues, individually, proved capable of disabling the highly active TK homolog, twitchin kinase. We concluded that the previous assignments of catalysis and substrates to TK derived from the presence of a contaminant kinase activity (or activities) in the insect cell preparations commonly employed for the production of this kinase.

The obstruction of functional studies by contaminant kinases in recombinant preparations from insect cells is not rare. For example, Hamel and co-workers (Hamel et al., 2011) found that a contaminant kinase in preparations of a substrate masked the activity of MAPK invalidating phosphorylation assays of the latter. A further case is

that of G-protein preparations, which are commonly contaminated with a lipid kinase (Shymanets et al., 2009). Scientifically misinterpreted, the contaminant activity was initially attributed to integrin-linked kinase (ILK), which later was shown to be an inactive pseudokinase (Fukuda et al., 2011). The study of potential catalysis in pseudokinases through loss of function variants can also yield notoriously misleading results. As examples, conventional KtoA active site mutants of BUBR1 affected the mitotic checkpoint (Malureanu et al., 2009, Huang et al., 2008), which was later shown to result from impaired conformational stability and not catalytic inactivation (Suijkerbuijk et al., 2012). The equivalent KtoA mutation in ILK led to renal agenesis during kidney development (Lange et al., 2009a), even though ILK has no catalytic activity and that pathogenic mutations act by impairing the structural integrity of this kinase (Fukuda et al., 2011). Similarly, the KtoA mutation destabilizes TK (**Figure 2.2**). We propose that also here structural grounds led to previous claims of loss of catalysis in TK^{K36A} variants (Mayans et al., 1998, Puchner et al., 2008, Grater et al., 2005).

Our findings prompt the reassessment of how TK as an inactive pseudokinase contributes to muscle stress signaling and indicate that its hypothesized mechanoactivation mechanism (Puchner et al., 2008) must be revisited, as this is unlikely to relate to phospho-transfer activity. The hydrophobic core of protein kinases is organized into two "spines": the R(regulatory) and C(catalytic) spines (Taylor et al., 2013). Typically, the R-spine assembles transiently during kinase activation. In TK, the R-spine is statically assembled into an active conformation (in the absence of phosphorylation in Y170 in the P+1 loop), adding to the active arrangement of the EFG motif and the activation loop (Temmerman et al., 2013). The C-spine includes residue Y107 from the αE-helix contributing to the stabilization of the TK fold in a permanent "pseudoactive" conformation (**Figure 2.10**).

Figure 2.10 Internal hydrophobic core architecture of PKA, TwcK and PKA. Residues forming C-spine are under yellow surface, R-spine under red. Residues are numbered according using PDB entry: **a**.) PKA 2CPK **b**.) TwcK 3UTO **c**.) 1TKI. Note the patchy arrangement of residues forming N-lobe portion of R-spine in TK. **d.)** N terminal portion αE-helix is intergrown with C-spine in TK. Molecular surface of TK's R-spine is in yellow, αE-helix of TK is in pale green, PKA in teal, and TwcK in pink. Sidechains of corresponding residues in PKA (Y146) and TwcK (Y257) are lateral towards R-spine, whereas in TK (Y107) is piercing the C-spine.

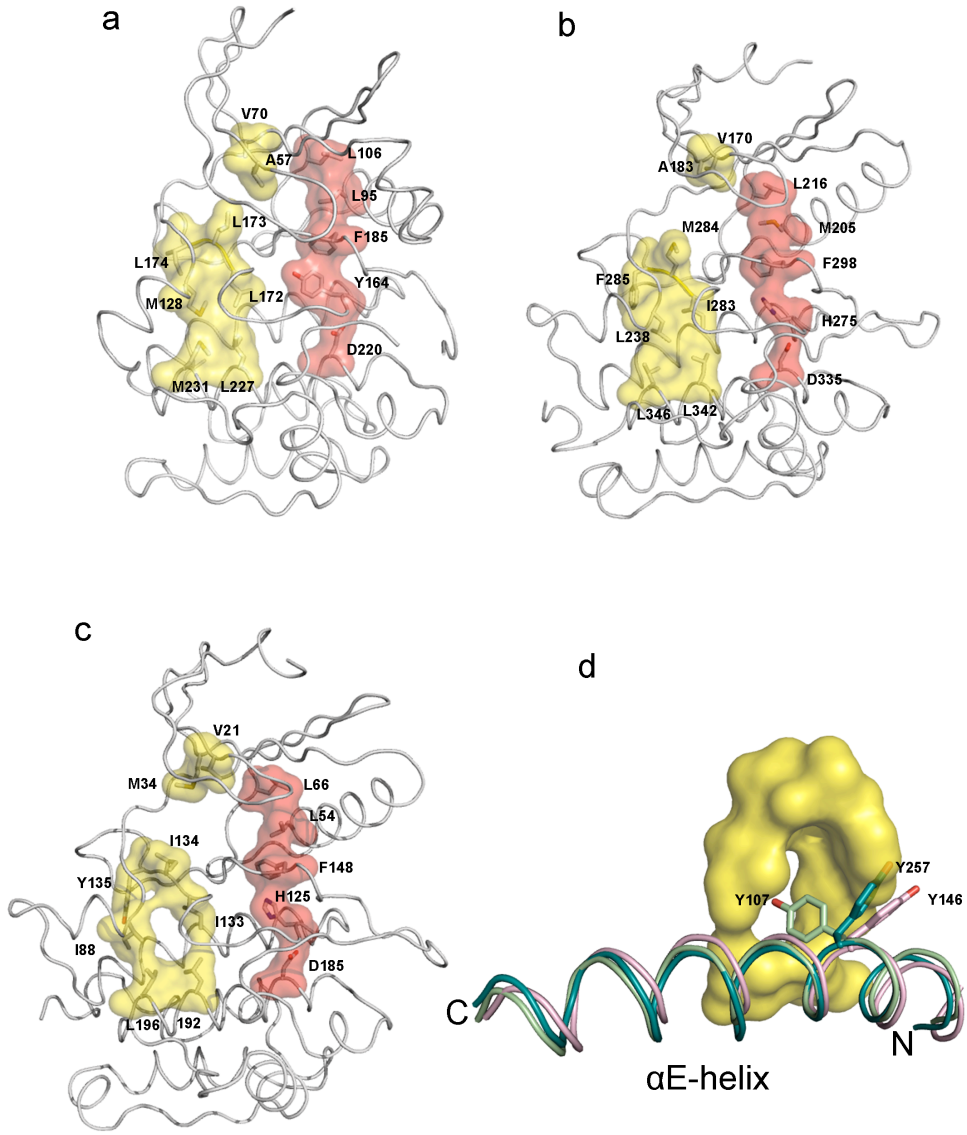

Thus, it is unclear how nucleotide binding –if it occurs– can lead to a switch response in this pseudokinase. Instead, mechanical deformations of the CRD tail might alter the features of the kinase surface, possibly modifying the interaction with its associated proteins. Pseudokinases participate in cellular pathways as regulated scaffolds for the assembly of signaling complexes (Boudeau et al., 2006). We show here that TK in its conformational ground state interacts with MuRF1. MuRF1 is present in low levels in the muscle cell and becomes transcriptionally up-regulated by myopathic stimuli including mechanical inactivity and metabolic stress conditions such as starvation or diabetes. This suggests that TK and MuRF1 are part of a shared stress-signaling pathway. Together with earlier data (Witt et al., 2005), it appears now that both MuRF1/MuRF2 can occupy the TK scaffold, where inactivity may cause the release of MuRF2 and the recruitment of MuRF1. This might result in either TK serving as a switch to gate MuRF1/MuRF2 signaling or TK serving as a cross-talk node of MuRFs pathways in function of myofibrillar stretch. This conformationally regulated scaffolding might constitute the primary switch mechanism of TK.

Finally, the inactivity of vertebrate TK contrasts markedly with the high levels of *in vitro* catalysis of its invertebrate homologs, TwcK, TTN-1 and projectin. Interestingly, this difference correlates with a similar contrast in obscurin kinases, also members of the TK kinase family. Obscurin is located in the sarcomeric M-line, linking together the sarcoplasmic reticulum (Lange et al., 2009b), titin (Bang et al., 2001) and the thick motor filaments (Kontrogianni-Konstantopoulos et al., 2004) Obscurin (and the invertebrate homolog UNC-89) contains two kinases, PK1 and PK2. In vertebrates, PK1 and PK2 have canonical active sites and are catalytically active (Hu and Kontrogianni-Konstantopoulos, 2013, Mayans et al., 2013). In invertebrates, PK1 is inactive or has modified its activity as it lacks identifiable catalytic residues; and PK2 has a degenerated active site indicating that its activity might be modest (Mayans et al., 2013). This inverse correlation in the catalysis of kinases from titin-like and obscurin-like filaments in vertebrate/invertebrate suggests a correlated co-evolution of giant protein kinases (**Figure 2.11**). It is tempting to speculate that in vertebrates, the inactivation of TK was coupled to a co-activation of the obscurin kinases. Thus, stretch-activated phospho-transfer seems to reside today in different filament systems in muscles across animal phyla. Future studies in these

muscle kinases are required to understand their patterns of activity and scaffolding in terms of muscle responses to stress stimuli.

Figure 2.10 Distribution of active kinases and inactive pseudokinases in titin-like filaments from vertebrate and invertebrate muscle
For each filament the following domains are shown: Ig (blue circles); Fn3 (green circles); active kinases (magenta boxes); inactive pseudokinases (grey boxes). Pseudokinases where inactivity cannot be reliably predicted are indicated with a question mark. The conservation of the Ig-Ig-Fn3-(pseudo)kinase domain arrangement is present independently of kinase catalytic properties.

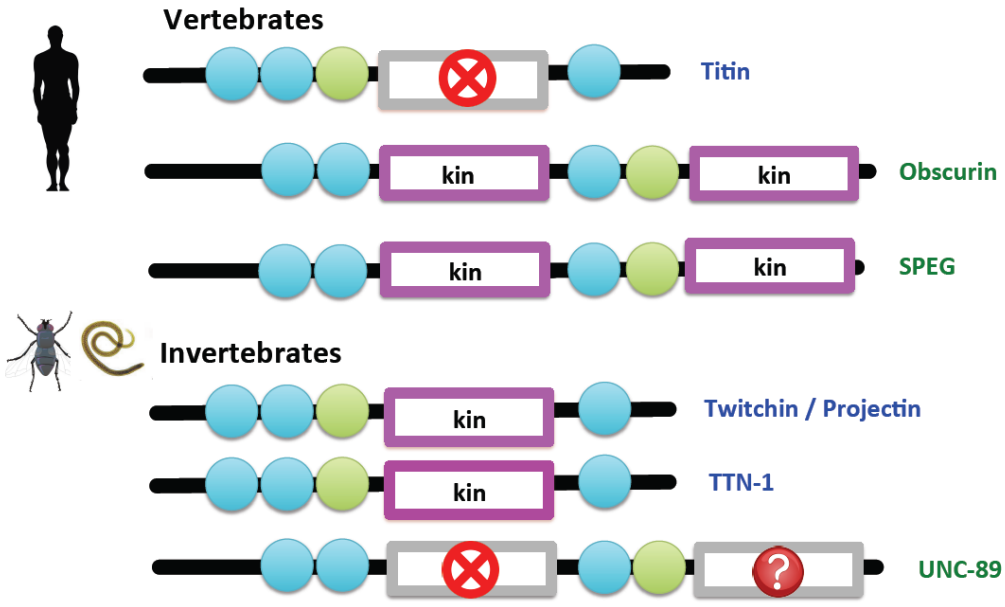

Chapter 3

Genetic perturbation of the evolutionary conserved motif bridging titin kinase and MuRF1 signaling platforms leads to dilated cardiomyopathy

3.1 Introduction

Titin has been frequently predicted to participate in stress signaling since the titin filament can sense sarcomeric strain that induces conformational changes within its polypeptide chain. In particular, mechanical models of stretch-activation have been proposed for the titin kinase (TK) domain that is evolutionarily conserved among titin-like myofilaments. Located at the C-terminus of the molecule, TK belongs to the myosin light chain kinase family of non-RD-kinases (Mayans et al., 1998). Experimental evidence underscores the critical role of TK in sarcomere maintenance. Deletion of TK enclosing M-band titin in mice is embryonically lethal due to failure in heart development (Weinert et al., 2006) or causes terminal cardiomyopathy when postnatally induced (Gotthardt et al., 2003). However, the TK-mediated signaling pathways are still poorly understood. *In vitro* studies of differentiating myocytes implicate TK-mediated phosphorylation of telethonin (TCAP) in the reorganization of the cytoskeleton during myofibrillogenesis (Mayans et al., 1998). In mature muscle, TK was proposed to act as a scaffold for assembly of the autophagic machinery complex, comprising nbr1, p62 and the E3 ubiquitin ligase MuRF2. This signalosome was suggested to act as a muscle activity sensor; upon mechanical inactivity the complex disbands and MuRF2 translocates to the nucleus where it excludes nuclear serum response factor and causes the repression of transcription (Lange et al., 2002). To date, all TK activity-regulating events have been identified in the catalytic domain, however, the neighbouring domains of many kinases are known to play a regulatory role. For example, the catalytic activity of twitchin kinase (TwcK), an invertebrate homologue of TK, has been shown to be regulated through a linker sequence N-terminal to the kinase domain (NL) (von Castelmur et al., 2012). In vertebrates, a binding site for the E3 ubiquitin ligases, MuRFs, is located N-terminally to the TK domain, formed by the evolutionary conserved tandem of Ig^{A168}-Ig^{A169}-$FnIII^{A170}$,

hereby A168-A170. It was consistently demonstrated that only MuRF1 is directly interacting with the A168-A170 repeat (Center et al., 2001, Witt et al., 2005, Mrosek et al ., 2008) whereas other two family members MuRF2 and MuRF3 might associate with titin filament indirectly (Centner et al., 2001, Lange et al., 2005). Functionally MuRF1 was shown to mediate muscle catabolism either through direct targeting of sarcomere components such as troponin I (Kedar et al., 2004), myosin heavy chain (Clarke et al., 2007) or muscle actin (Polge et al., 2011) to degradation by ubiquitin-proteasome pathway or indirectly by regulating gene expression machinery (Willis et al., 2007, Wadosky et al., 2014, Willis et al., 2014), muscle energetics (Willis et al., 2009, Hirner et al., 2008), protein kinase Cε (Arya et al., 2004) or acetylcholine receptors (Rudolf et al., 2013, Khan et al., 2014). However, the functional basis of MuRF1-TK interaction remains elusive. It was demonstrated that overexpression of MuRF1 disrupts the binding region of titin (McElhinny et al., 2002), but there are no indications, that titin could be a substrate for the ubiquitin ligase activity of MuRF1 (Kedar et al., 2004), implying other than a simple enzyme-substrate relation between MuRF1 and titin.

To explore the possibility of crosstalk between TK and MuRF1 signalling pathways, we have determined the crystal structure of human TK together with its flanking domains (A170-TK-M1). We then investigated the molecular consequences of a rare SNP, rs200675195, in the NL (N-terminal linker connecting A170 and TK) segment corresponding to the mutation D24728V[3], found in a small family affected by dilated cardiomyopathy (DCM). The mutation increases interdomain flexibility, resulting in enhanced MuRF1-dependent ubiquitination of TK. Together with the previous identification of MuRF1 as a myocardial anti-hypertrophic gene (Witt et al., 2008, Chen et al., 2012, Willis et al., 2007), our results suggest that genetic perturbation of the A170-TK /MuRF1 complex is likely to affect myocardial trophicity, and that this is a probable disease mechanism in the hereditary cardiomyopathy here reported.

[3] Residue numbering is based on titin protein entry NP_003310.4. For simplicity, throughout the text this mutation will be referred to as "DtoV".

3.2 Materials and Methods

3.2.1 Protein cloning and expression

A list of protein constructs used in this study is presented in **Table 3.1**. Recombinant samples for crystal structure determination, NMR, SAXS and GST-pulldown were produced in *E.coli* as described (Bogomolovas et al., 2009). Constructs containing TK were expressed in SoluBL 21 (Genlantis), others in BL21 Star (Novagen) cells.

For adenovirus production A168-TK^{WT} and A168-TK^{DtoV} were cloned into pET-GST1a vector (Bogomolovas et al., 2009). This vector fuses a His_6-tagged GST and a TEV (tobacco etch virus) protease cleavage site N-terminally to the target construct. The fusion was then cloned into the adenovirus production vector DUAL-CCM(+) and RGD-modified fiber knob recombinant adenoviruses were commercially produced and purified (Vector Biolabs).

For MuRF1 expression in mammalian cells, the pEGFP-C1 vector was used. Open reading frame of EGFP was replaced with MuRF1 through NheI-NotI restriction sites.
Twitchin kinase constructs were produced as described (von Castelmur et al., 2012). DtoV exchange in $_{NL}TwcK_{CRD}^{DtoV}$ was introduced through overlap extension PCR. All constructs were verified by sequencing.

Table 3.1 Protein constructs

Construct	Reference sequence, residue numbers and applied changes	Description
A170-M1^{WT}	NP_003310; Res. 24622-25160	Wildtype titin kinase domain surrounded by neighbouring fibronectin (A170) and immunoglobulin (M1) domains.
A170-M1^{DtoV}	NP_003310; Res. 24622-25160; Asp24728Val	Mutant titin kinase domain surrounded by neighbouring fibronectin (A170) and immunoglobulin (M1) domains.
A170-TK^{WT}	NP_003310; Res. 24622-25068	Wildtype titin kinase domain with preceding fibronectin domain
A170-TK^{DtoV}	NP_003310; Res. 24622-25068; Asp24728Val	Mutant titin kinase domain with preceding fibronectin domain
A168-TK^{WT}	NP_003310; Res. 24430-25068	MuRF1 binding site extended with wildtype TK domain
A168-TK^{DtoV}	NP_003310; Res. 24430-25068; Asp24728Val	MuRF1 binding site extended with mutant TK domain
TK^{WT}	NP_003310; Res. 24747-25068	Wildype TK core
A168-NL^{WT}	NP_003310; Res. 24430-24731	MuRF1 binding site with NL of wildtype TK
A168-NL^{DtoV}	NP_003310; Res. 24430-24731; Asp24728Val	MuRF1 binding site with NL of mutant TK
A170-NL^{WT}	NP_003310; Res. 24622-24747	Fibronectin domain with wildtype N-terminal linker
A170-NL^{DtoV}	NP_003310; Res. 24622-24747 Asp24728Val	Fibronectin domain with mutated N-terminal linker
GST-MuRF1cc	NP_115977 Res. 169-327	Coiled-coil region of MuRF1 fused to GST
MBP-MuRF1	NP_115977	Full length human MuRF1 fused to MBP
TwcK$_{CRD}$	NP_502274.2; Res. 6245-6581	C.elegans twitchin kinase domain with CRD
$_{NL}$TwcK$_{CRD}$	NP_502274.2; Res. 6205-6581	C.elegans twitchin kinase domain with NL and CRD
$_{NL}$TwcK$_{CRD}^{DtoV}$	NP_502274.2; Res. 6205-6581; Asp6235Val	Mutant C.elegans twitchin kinase domain with NL and CRD

3.2.2 Crystal structure determination

Crystals of A170-M1^{WT} were grown in 2 µL hanging drops at 20 °C obtained by mixing protein solution and mother liquor (12% PEG 4K, 0.1 M Tris pH 7.5, 50 mM NaCl, 30% glycerol, 5 mM L-proline) in equal proportions. For X-ray data collection crystals were flash frozen in mother liquor. Diffraction data were collected on I04-1 beamline at Diamond Light Source (Didcot, UK) using PILATUS 2M photon counting detector (Dectris, Baden, Swizerland) at 0.91730 Å wavelength. In

total 180 images were collected with 4.5 s exposure time, 1 ° oscillation and detector distance of 297 mm. Data and model refinement statistics are listed in **Table 3.2**. For merging statistics anomalous pairs were kept separate. Phasing was done by molecular replacement in Phaser (McCoy, 2007) using TK (PDB entry 1TKI, Mayans et al., 1998), the A170 Fn3 domain (PDB entry 2NZI, Mrosek et al., 2007) and the M1 Ig domain (PDB entry 2BK8) as search models. Manual rebuilding was in COOT (Emsley et al., 2010). The model was refined and the solvent built in PHENIX (Adams et al., 2011).

Table 3.2 X-ray data statistics and model refinement parameters

	A170-M1^{WT}
Space group	**P 2_1**
Cell dimensions	
a, *b*, *c* (Å)	63.61, 184.65, 66.08
a, b, g (°)	90, 116.6, 90
Solvent content (%)	55.16
Matthews coef. (Å^3/Da)	2.74
Copies in asu	2
Data collection	
X-ray source	DIAMOND I04-1
Detector	PILATUS 2M
Wavelength (Å)	0.91730
Resolution (Å)	29.54-2.39 (2.48-2.39)
No.unique reflections	52551 (5292)
R_{sym}(I) (%)	13.2 (72.2)
I / sI	8.47 (1.54)
Completeness (%)	97.8 (98.7)
Redundancy	3.4 (3.3)
Refinement	
Resolution (Å)	29.54-2.39
R_{work} / R_{free}(%)	18.92 / 24.68
No. atoms	8870
Protein	8666
Water	204
B-factors	
Protein	49.2
Water	45.5
R.m.s. deviations	
Bond lengths (Å)	0.009
Bond angles (°)	1.26

3.2.3 Exome sequencing

Genomic DNA was extracted from buffy coat using a commercial kit (Qiagen) and exome sequencing was performed on two affected subjects. The patients in this study were identified from a standardized DCM cohort (Knoll et al., 2006). Sequencing was performed commercially (BGI Americas). Adapters were ligated to shared genomic DNA, amplified by ligation mediated PCR, purified and hybridized to custom NimbleGen array for enrichment. Captured fragments were sequenced on a high throughput HiSeq2000 platform. Raw image files were processed by Illumina base calling Software 1.7 for base calling with default parameters and the sequences of each individual were generated as 90bp paired-end reads. Further reads were processed and variants called using two independent workflows: GATK(DePristo et al., 2011, McKenna et al., 2010) and DNAnexus implemented in DNAnexus cloud-based data analysis and management platform for DNA sequencing data. Variants shared between both subjects were further filtered using against dbSNP135 and the 1000 Genome project to exclude previously identified disease irrelevant SNPs using wANNOVAR (Chang and Wang, 2012). Genetic variations in DCM gene list (Meder et al., 2011) were reported. Identical results was obtained using both data processing pipelines.

3.2.4 NMR studies

For NMR titration studies A170-NL^{WT} and A170-NL^{DtoV} were uniformly ^{15}N labeled in M9 medium as described (Bogomolovas et al., 2009) and titrated with unlabelled TK^{WT}. $^{1}H^{15}N$ heteronuclear single quantum correlation spectra were recorded at 22 °C in 20 mM Tris pH 7, 50 mM NaCl, 0.5 mM TCEP on Bruker 700 MHz spectrometer equipped with cryogenic triple-resonance probes. Spectra were processed with Topspin.

3.2.5 X-ray solution scattering

SAXS data were collected on the P12 beamline (λ=0.124 nm) at the Petra III storage ring (EMBL, DESY, Hamburg) using a 2D photon counting Pilatus 2M pixel

X-ray detector (Dectris, Switzerland). Data were processed and reduced using the ATSAS software package (Petoukhov et al., 2007). Radiation damage, monitored by repetitive 1 sec exposures, was negligible. Were applicable replicated measurements were averaged using PRIMUS (Konarev et al., 2003) and curves at several protein concentrations merged using ALMERGE (Franke et al., 2012). Radiuses of gyration (R_{gyr}) (alternatively calculated based on Guinier approximation using AUTORG, Petoukhov et al., 2007), maximum particle dimensions (D_{max}), and pair distribution functions (P(r)) were calculated using the indirect transform package DATGNOM (Petoukhov et al., 2007). The molecular weight was estimated from SAXS profiles using the Porod volume based MoW server (Fischer et al., 2010)

3.2.6 Cell culture

H9C2 rat cardiomyocytes were grown in DMEM/10% FCS/1X IST and antibiotics on gelatin coated 10 mm dishes. For differentiation into myotubes cells were allowed to reach confluence and then grown for 7 additional days in DMEM supplemented with 1% FCS and 1 mM all-trans retinoic acid. Myotubes were transfected at 100 MOI with recombinant adenovirus expressing wildtype or DtoV mutant GST-A169-TK and when indicated transfected with MuRF1 expressing plasmid using TurboFect reagent (Fisher Biosciences) according to manufacturer recommendations. After 24 hours cells were lysed in PBS+ 0.2% NP-40 + 2 mM DTT and protease inhibitors and clarified supernatant was purified on glutathione resin.

3.2.7 GST-Pulldown with recombinant proteins

Approximately 50 µg each of GST-A168-NL^{WT}, GST-A168-NL^{DtoV} and GST-MuRF1 were immobilized on 30 µl of Glutathione-Sepharose-beads and washed once with PBS + 0.1% NP40. Purified His_6-MBP-MuRF1 was diluted 20-fold in PBS supplemented with 0.1% NP40. After centrifugation for 10 min at 14000g, the volume corresponding to 20 µg His_6-MBP-MuRF1 (approximately 500µl) was then added to each of the three tubes. The tubes were then incubated for 2-3 hours at 4°C under light movement. After spinning for 1 min at 3000g supernatants were removed and

the beads washed either 1x with 1 ml PBS or 1x with 1 ml PBS + 0,1% NP40 and 1x with 1 ml PBS. Supernatants were completely removed, and the beads were directly resuspended in SDS sample buffer. The supernatant was completely removed and 30 µl of 1.3x LDS Sample Buffer (Invitrogen) added to the beads. After 10 min incubation at 70°C the supernatant was transferred to a fresh tube and then separated on 4-12% Bis-Tris gels (Invitrogen).

3.2.8 Western Blot

After separation on 4-12% Bis-Tris Gels proteins samples were transferred onto a nitrocellulose membrane, which was subsequently blocked in TBST/5%BSA. After washing the membrane 2x in TBST the filter was incubated for 2h with anti-human TK (Myomedix, Mannheim, Germany) at a concentration of 0.5µg/ml in TBST/5%BSA. The membrane was washed three times in TBST, incubated for 1h in TBST containing goat anti-rabbit IgG conjugated to alkaline phosphatase at 1:1000 dilutions (Dako, Glostrup, Denmark). After 3 washes in TBST and a final wash in TBS, the detection with NBT/BCIP was done as described by the supplier (Roche Diagnostics).

Alternatively membranes were incubated with Cy3-labelled anti-rabbit-IgG (Jackson) as a secondary antibody at a concentration of 0.5µg/ml. Incubation and washes were performed as described above. The membrane was then dried and scanned with an FLA-5100 fluorescent image analyser (Fuji).

3.3 Results

3.3.1 Crystal structure of A170-M1 reveals structural basis of MuRF1 and TK crosstalk.

We have elucidated the crystal structure of the human titin kinase region A170-M1 that spans both up- and downstream neighbouring domains and the respective linker sequences (**Figure 3.1**). The structure at 2.46 Å resolution reveals that the kinase domain is enwrapped by both the N- and C-terminal linker sequences with fibronectin A170 and immunoglobulin M1 domains projecting from the assembly (**Figure 3.1b**).

Figure 3.1 Crystal structure of A170-TK-M1
a. Schematic representation of TK environment. Domains are coloured as in crystal structure, additional domains forming the MuRF docking platform are represented in dashed lines. **b**. Overall crystal structure of A170-M1^{WT}; Fn3 domain A170 is in blue, N-terminal linker is in yellow, kinase core is represented as grey molecular surface, C-terminal regulatory tail is in green and Ig domain M1 is in red. D^{24728} is represented as a purple sphere.

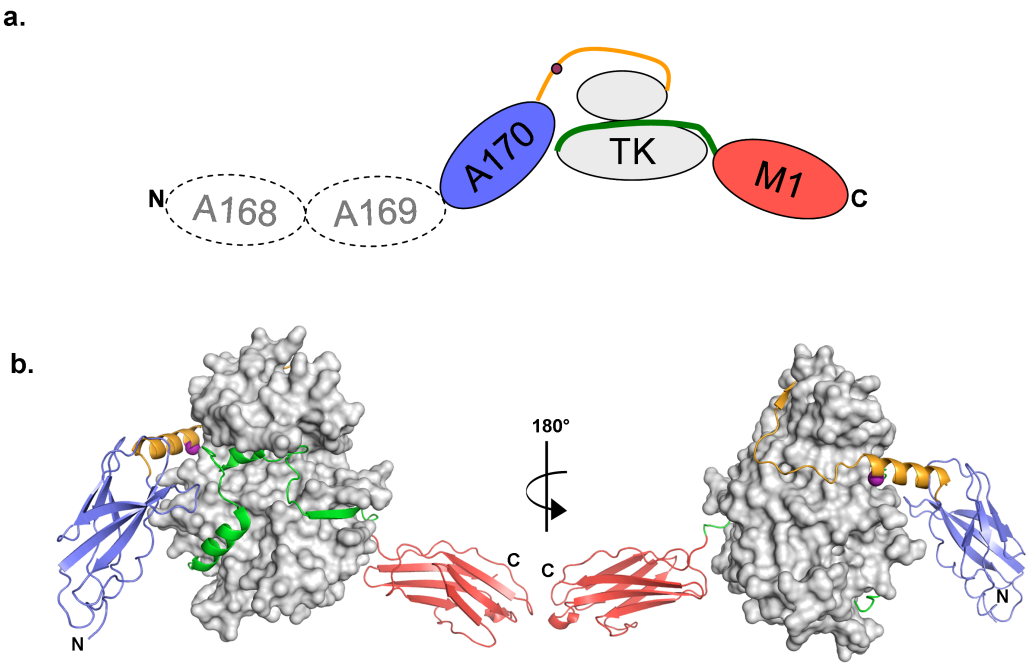

In excellent agreement with previous data (Mayans et al., 1998), the C-terminal tail domain (CRD) wraps around the larger kinase C-lobe, deeply penetrating the catalytic cleft. The N-terminal linker (NL) is 23 residues long and straddles the back of the N-terminal kinase lobe, packing against the hinge region in a similar fashion to that of the equivalent fragment in the invertebrate twitchin kinase (von Castelmur et al., 2012). In titin kinase, however, the NL forms a prominent α-helix in its junction to domain A170. The structure shows that this NYD motif mediates a number of interactions that secure the packing of the NL segment to the kinase domain (**Figure 3.2a**). In particular, the lateral carboxyl group of Asp^{24728} is buried in the interface of the kinase domain, where it engages in two hydrogen bond interactions with i) the lateral hydroxyl group of Ser^{24831} that is located in a loop between the α-helix C2 and β-strand C5 and ii) the amino backbone group of Arg^{24885} located in the loop between β-strands C7 and C8. The rest of the NL segment interacts with the kinase core only loosely (**Figure 3.3a**), and in fact structural differences are observed in this region between the two asymmetric unit copies (**Figure 3.3b**).

Figure 3.2 NL region orchestrates domain arrangement and acts as a spacer between two MuRF1 binding sites
a. Close-up of the NL-TK interaction. D^{24728} is located at the helical region of the N-terminal linker, making hydrogen bonds with the Ser^{24831} and Arg^{24885} and thus attaching the N-terminal linker to the kinase core. b. Dissection of MuRF1-titin interaction using a fluorescent binding assay. The helical domain of MuRF1 binds to established site A168-A170 and has affinity to the kinase domain itself, whereas NL acts as a repellent for MuRF1 and reduces the binding.

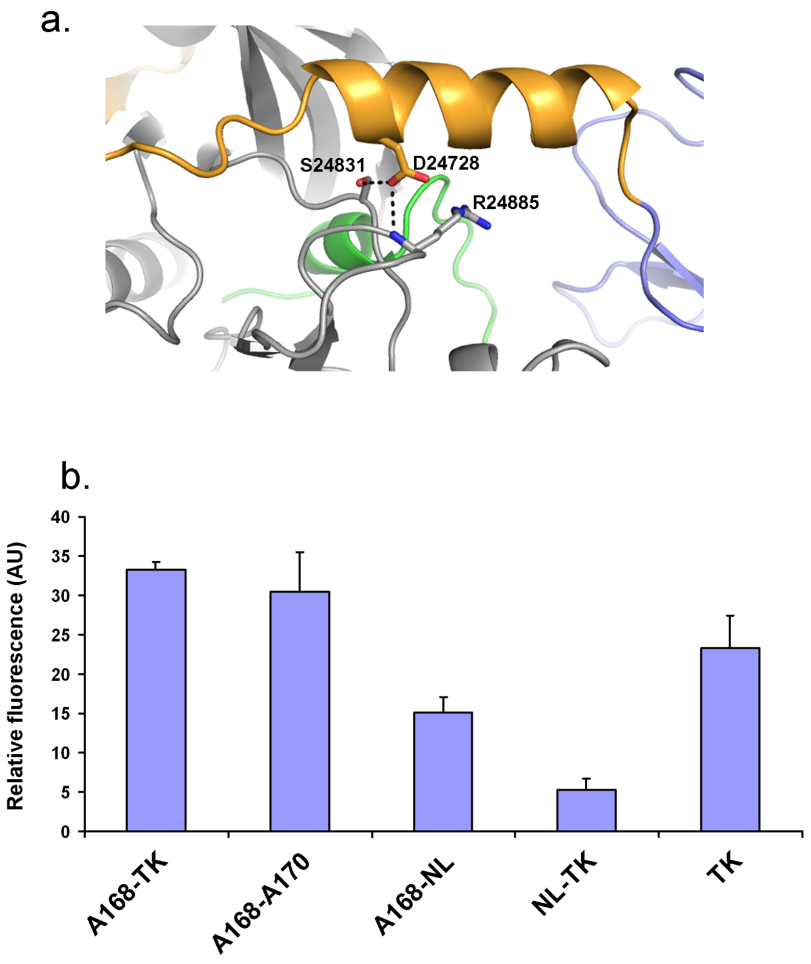

These findings indicate that the NYD motif crucially contributes to the packing of the NL segment against the kinase domain. MuRF1 binds a tandem of three Ig-like domains, A168-A170, immediately preceding the TK domain (Centner et al., 2001). The binding is mediated by the C-terminal helical domain of MuRF1 and is deterministically influenced by the presence of a loop with sequence KTLE in the titin domain A169 (Mrosek et al., 2007, Muller et al., 2007). However, TK domain and NL have not been considered as an integral part of the MuRF1 binding site previously. Motivated by the compact domain arrangement in the A170-M1 structure, we evaluated the possible contribution of NL and TK to the MuRF1 binding surface (**Figure 3.3b**). In excellent agreement with published data, A168-A170 is capable of binding MuRF1. Interestingly, we observed that inclusion of NL to the known A168-A170 binding site (construct A168-NL) or TK (construct NL-TK) significantly reduced MuRF1 binding. Consequently, combination of both MuRF1 affinity regions A168-A170 and TK in construct A168-TK had no additive effect, as repellent NL was included. Taken together, these results indicate that the MuRF1 binding site spans the region A168-TK, consisting of two affine regions brought together through the repellent NL.

Figure 3.3 Interactions between NL and TK.
a. Specific Interactions were analysed using YASARA software. Note that mainly beginning (where D31225V is located) and the end of the NL are specifically interacting with TK. **b**. Superimposition of the two molecular copies of A170-M1 in the crystallographic asymmetric unit. Both ribbon thickness and colouring correspond to the RMSD values of the superimposition as given in the accompanying scale, where minimum, maximum and average RMSD values are shown. The structural agreement is overall excellent except for the differences in the middle of NL.

a.

Hydrophobic interactions

N-terminal linker	Kinase core
Ala 24724	Arg 24885
Tyr 24727	Arg 24770 Phe 24829 Ser 24831 Val 25040 Val 25041
Asp 24728	Thr 24884
Glu 24730	Thr 24779 Phe 24829
Val 24731	Phe 24829 Ser 24831 Gln 24883 Thr 24884
Arg 24735	His 24812
Ser 24738	Arg 24806
Thr 24740	Arg 24806
Ala 24742	Leu 24813
Ser 24743	Glu 24815
Ser 24745	Glu 24749
Ser 24746	Lys 24748 Glu 24749
Thr 24747	Phe 24817 Ser 24819 Glu 24822 Val 24824

Hydrogen bonds

N-terminal linker	Kinase core	Distance (Å)
Tyr 24727	Glu 24758	1,78
Asp 24728	Arg 24885	2,4
	Ser 24831	1,37
Glu 24730	Thr 24779	1,72
Ala 24742	Asn 24803	1,97
Ser 24743	Ser (N) 24816	1,92
	Ser (OG) 24816	2,43
His 24744	Ser (N) 24816	1,68
	Ser (OG) 24816	1,89
Ser 24745	Ser 24816	2,34
	Glu 24818	1,8
Ser 24746	Glu 24749	2,08
	Lys 24748	2,44
Thr 24747	Glu 24818	2,28
	Leu 24750	2,18

π-π interaction

N-terminal linker	Kinase core
Tyr 24727	Phe 24829

π-cation interaction

N-terminal linker	Kinase core
Arg 24735	His 24812

b.

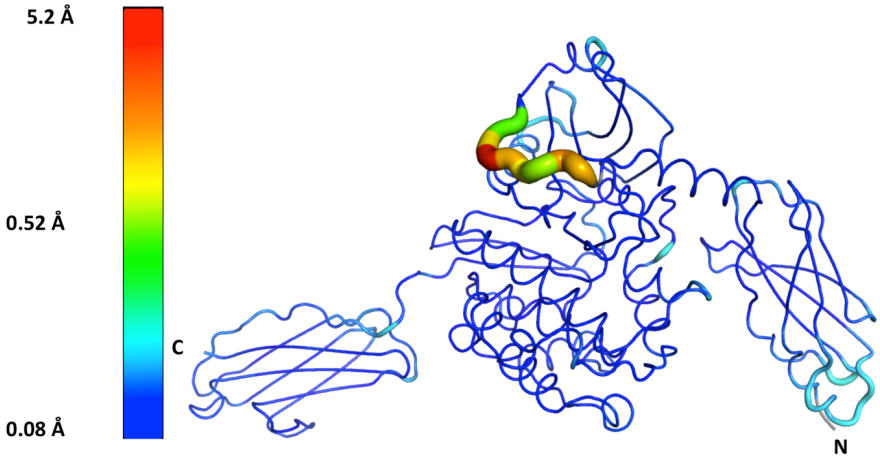

3.3.2 Structural context of D24728 is conserved among the titin-like myofilaments

The crystal structure of A170-M1 implied that compact A170 and TK domain arrangement is influenced by D^{24728} located in the helical region of NL. Examination of primary NL sequences revealed remarkable conservation of the discussed aspartate residue among titin-like filaments in the animal kingdom (Figure 3A). The conservation of this linear motif is reflected in its preserved 3D context. Superimposition of corresponding structures of human TK region and the *C. elegans* titin-like filament, twitchin, (PDB 3UTO[5]) revealed that the structural context of D^{24728} is highly similar (**Figure 3.4**). Taken together, D^{24728} and homologous aspartates in titin-like filaments are under strong evolutionary pressure for conservation.

Figure 3.4 Helical region of NL is highly conserved among the titin-like myofilaments
a. D^{24728} is highly conserved in the titin kinase family. **b**. Superimposition of human TK (this work) and twitchin from *C. elegans* (PDB 3UTO[5]) reveals that the structural context of D^{24728} is highly preserved between the human and worm proteins (residue numbering follows the PDB entry).

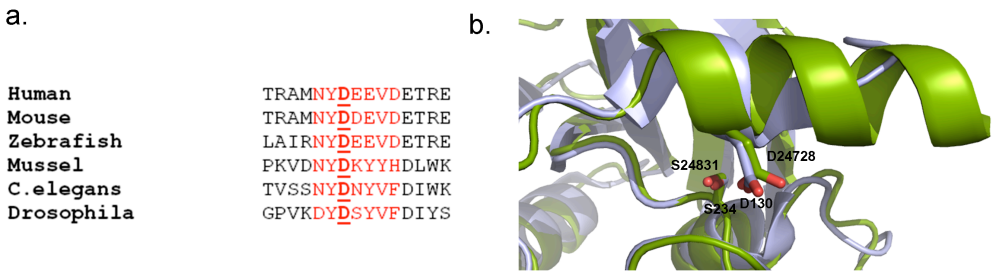

3.3.3 Rare SNP rs200675195 in NL is associated with hereditary dilated cardiomyopathy

Outstanding preservation of D^{24728} among titin-like myofilaments led us to speculate on the detrimental effects of mutations at this position. SNP rs200675195

causing D^{24728} mutation to valine was found in the short genetic variation database dbSNP. Within a large meta-cohort[4] of assembled exome sequences this allele was found in 5 from a total of 12031 sequenced individuals, resulting in a minor allele frequency (MAF) of 0.02%. In NHLBI GO Exome Sequencing Project cohort, that is enriched in individuals with heart, lung and blood disorders, this allele was also found 5 times, corresponding to roughly 1 of 2,500 patients (yielding a higher MAF of ~0.04%). The higher MAF of rs200675195 in NHLBI GO Exome Sequencing Project cohort compared to larger unbiased meta-cohort implies that this mutation is associated with heart, lung and blood disorders. Consistent with this idea, available SNP effect predicting algorithms (SIFT [23], PROVEAN [24], Polyphen-2[25]) predict DtoV to be damaging. To further test this hypothesis, we performed direct sequencing of the TK-encoding titin exon in 200 cardiomyopathy patients [26]. This also identified rs200675195 in one patient diagnosed with severe DCM. Furthermore, presence of this allele was predictive for the disease in the available small family tree (**Figure 3.5a and 3.5b**), since a daughter was found to be heterozygous for the DtoV mutation and suffered from heart disease.

[4] http://genome.sph.umich.edu/wiki/Exome_Chip_Design

Figure 3.5 Rare SNP rs201763096 causing D24728V exchange is associated with dilated cardiomyopathy

a. DtoV mutation in a DCM family (+/- indicates heterozygosity for the mutation; arrow indicates index patient; grey indicates unknown clinical status; open squares or circles: unaffected, black circles or squares indicate affected; age at death in brackets; slash indicates deceased; roman numbers indicate # of generations studied; arabic numbers indicate patients. **b.** Clinical characteristics. **c**. Summary of identified genetic variants.

a.

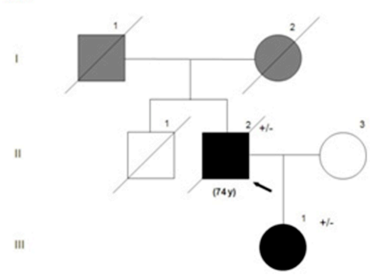

b.

Mutation	Patient	Clinical characteristics	NYHA class
DtoV	II-2	DCM, survived sudden cardiac arrest in 1986	IV
DtoV	III-1	Beginning DCM, sinus tachycardia	I

c.

Gene	Substitution	Allele frequency	SNP id	Zygosity status	PROVEAN prediction	SWIFT prediction	Polyphen-2 prediction
TTN	DtoV	0.0419%	rs200675195	Het	-6.42 Deleterious	0.001 Damaging	1.000 Probably damaging
NEXN	EtoA	0.2017%	rs201763096	Het	-1.839 Neutral	0.023 Damaging	0.067 Benign

Finally, we sequenced whole exomes of the two DtoV patients to search for other genetic variants associated with DCM; the DtoV allele may only cause disease as a compound heterozygote, or might not be the disease-causing allele in the first place. In both analyzed patient exomes, the set of known DCM associated genes[27,28] had good sequence coverage (**Figure 3.6**). After variant calling and filtering, two shared heterozygous variants in DCM associated genes were identified; the aforementioned DtoV allele in TK and a second variant in nexilin. The nexilin variant frequency was above the proposed cut-off for pathogenic DCM mutations[28] and was predicted to be benign (**Figure 3.5c**).

Figure 3.6 Mean exon coverage for the DCM genes. Average exon coverage for patient II-2 is shown in red, for patient III-1 in black. All genes were sequenced with sufficient sequencing depth for reliable genetic variant calling.

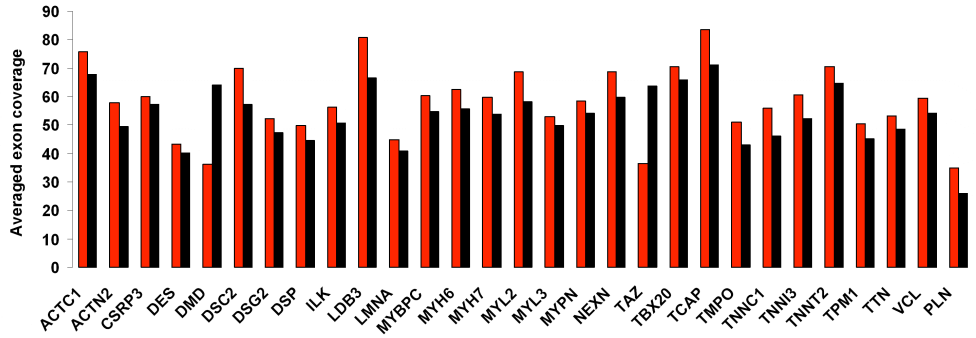

In summary, our sequencing data predict that individuals with the rare SNP, rs200675195, have and increased likelihood of suffering from DCM. Future studies with larger families will be required to formally prove this association, or to test for additional alleles acting as compound heterozygotes.

3.3.4 The D24728V mutation impairs the structure of extensive regions of the MuRF1 binding site

Our data indicated that rare SNP, rs200675195, may be involved in the pathogenesis of human DCM. In the DtoV exchange caused by the studied SNP, the small hydrophobic residue introduced is incapable of hydrogen bonding through its side chain and is likely to impair the binding of the NL segment against the kinase core. We predicted that this destabilizes the packing of the full NL segment, possibly disrupting the connection between high affinity binding sites of MuRF1 on titin. Structurally, the DtoV mutation occurs within the segment that links TK to its preceding Fn3 domain, A170, which is a part of the MuRF1 binding site on titin[21, 22]. Therefore, we hypothesized that the DtoV mutation might impair the packing of the NL against TK. To address this question we performed *in vitro* NMR titrations using ^{15}N labelled A170-NL and unlabelled TK (**Figure 3.7a and 3.7b**). We speculated that if in a single polypeptide chain NL and TK interact with each other, then upon splitting them into two separate chains they would bind to each other. Experimentally

we could confirm that after splitting, A170-NL^{WT} interacts with TK, as demonstrated by the chemical shift perturbations in HSQC spectra overlays (**Figure 3.7a**). Overlay of A170 and A170-NL spectra indicated that mainly resonances from NL residues are perturbed, implying nativity of the observed interaction (**Figure 3.8**). However, when TK was titrated with A170-NL^{DtoV} no chemical shift perturbations were observed (**Figure 3.7b**), indicating no interaction between proteins. Consistent with this observation, multiple structural perturbations are seen in the NL region when spectra from A170-NL^{WT} and A170-NL^{DtoV} are superimposed (**Figure 3.8**). In conclusion, NMR data indicate that DtoV substitution causes structural perturbation, resulting in abolishment of NL attachment to the TK core.

Figure 3.7 Structural consequences of DtoV exchange.
a. HSQC-monitored titration of A170-NL^{WT} with increasing concentrations of TK^{WT} (red, green, magenta). Black arrows indicate the major peak shifts. **b**. HSQC spectra overlay of A170-NL^{DtoV} (red) and in presence of TK^{WT} (magenta) reveal no peak shifts. **c**. SAXS-derived molecular parameters; D_{max}, R_{gyr}, V_{porod} and MW denote maximal dimension, radius of gyration, Porod volume and molecular weight, respectively. MW_{calc} derived from scattering curve, MW_{theor} based on primary sequence. **d**. Distance distribution functions of A170-TK^{DtoV} and A170-TK^{WT}. **e**. Dimensionless Kratky plot of A170-TK^{DtoV} and A170-TK^{WT} scattering curves. Intersection of black lines indicates expected maximum position for a fully rigid globular protein (that follows Guinier's law $I(q) = I(0)\exp(-(qR_{gyr})^2/3)$).

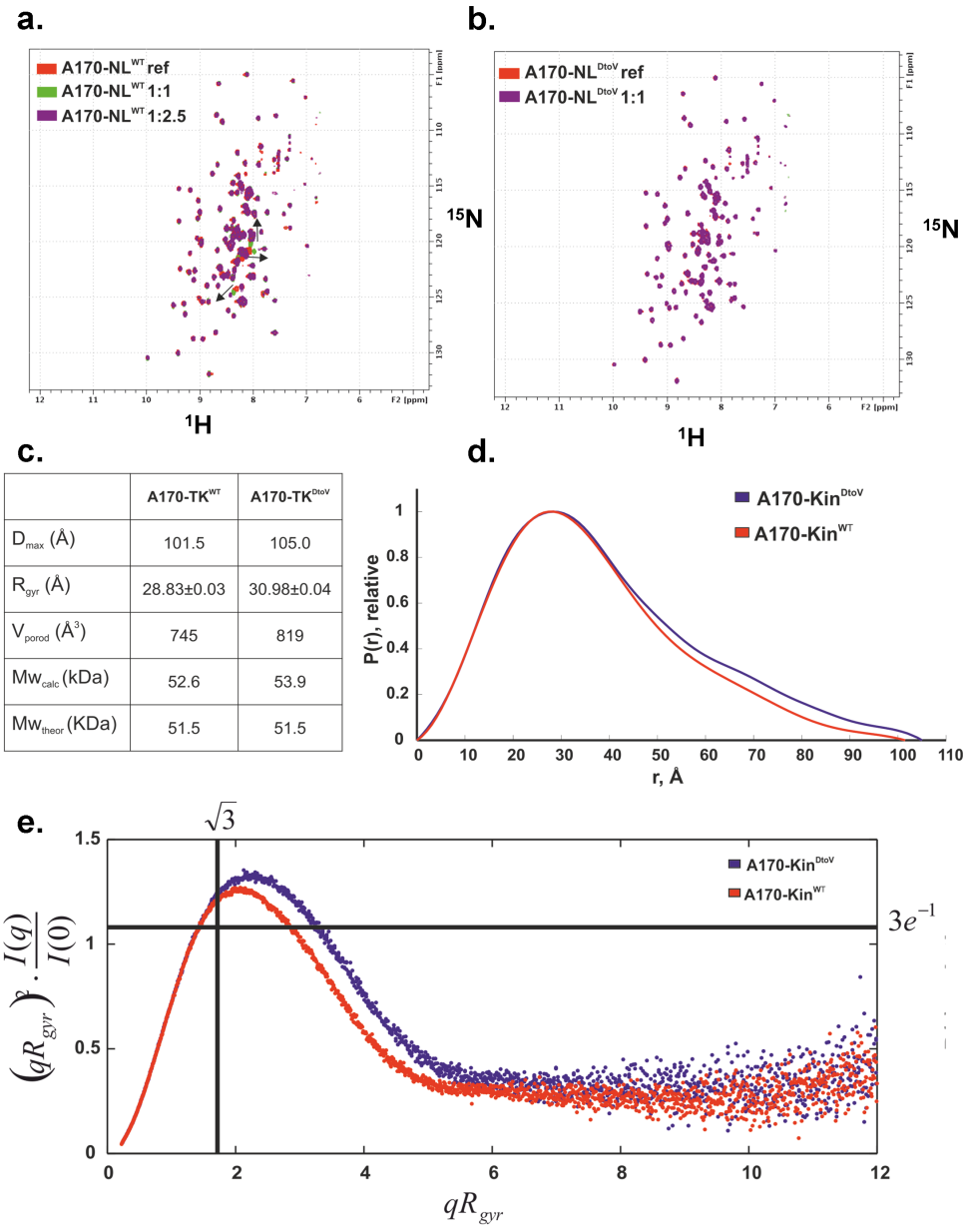

	A170-TK^{WT}	A170-TK^{DtoV}
D_{max} (Å)	101.5	105.0
R_{gyr} (Å)	28.83±0.03	30.98±0.04
V_{porod} (Å^3)	745	819
Mw_{calc} (kDa)	52.6	53.9
Mw_{theor} (KDa)	51.5	51.5

Figure 3.8 Effect of D31225V mutation on NL. HSQC spectra overlay of solely A170 domain (red) and A170-NL constructs: wildtype (blue) and mutant (green) (both wildtype and mutant versions). The Asp to Val mutation alters those chemical shifts that arise from the linker residues (indicated in square). Multiple structural perturbations caused by the mutation indicate major effects on the A170-NL segment**.**

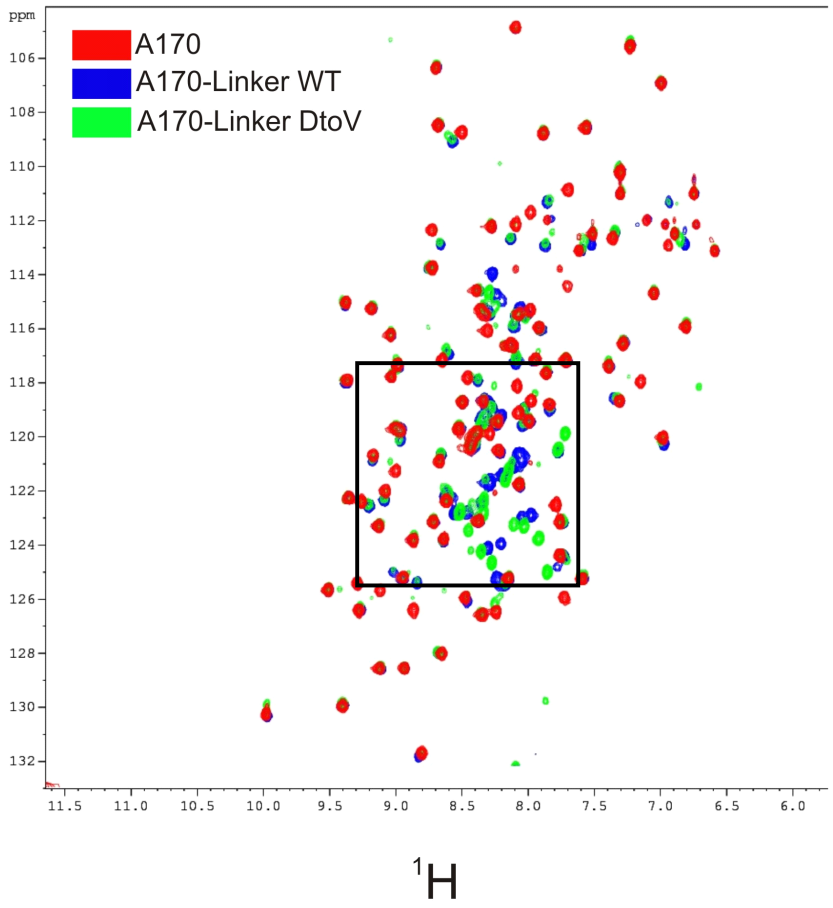

In order to gain an insight into the effect of the DtoV mutation on interdomain organization, we performed SAXS measurements on A170-TK^{DtoV} and A170-TK^{WT}. A larger radius of gyration and increased maximal particle dimension indicated a change in conformation caused by the mutation (**Figure 3.7c**). To evaluate possible differences in interdomain flexibility caused by the DtoV mutation, SAXS data were presented in a dimensionless Kratky plot (**Figure 3.7d**), allowing for direct comparison of objects of different shape and size. In this representation a rigid globular protein would provide a bell shaped curve with a maximum value of ~ 1.1

(3*exp(-1)) at ~ 1.75 ($\sqrt{3}$), whereas completely flexible unfolded protein would yield a curve that gradually increases to a constant value of 2. Both WT and mutant A170-TK show broadening of a bell shaped curve and shift of a maximum towards higher qR_{gyr} values, expected for the scattering of proteins with structured domains linked by flexible linkers[29,30]. The scattering curve of A170-TK^{DtoV}, when compared to wildtype is broader and its maximum is further shifted towards high qR_{gyr} values, consistent with a more flexible domain conformation in this mutant. These findings are at least partially reflected in the pair distribution function (P(r)), which represents the histogram of distances between scattering volumes within the molecule (**Figure 3.7e**). Taken together, our data indicate that the DtoV mutation is sufficient to impair binding of NL to TK, resulting in increased interdomain flexibility between the previously characterized MuRF1 binding site and TK.

3.3.5 The D24728V mutation causes activation of homologous *C. elegans* kinase

In order to validate the observed effects of DtoV substitution we chose *C. elegans* twitchin kinase (TwcK) as a model. TwcK is a well-characterized invertebrate homologue of human TK, with which it shares high sequence and structural similarity (RMSD for *C. elegans* TwcK and human TK is 1.29 Å, 34 % sequence identity). Moreover, the role of the NL segment as an intrasteric inhibitor of TwcK catalysis is well characterised (von Castelmur et al., 2012). In contrast, recombinant TK preparations are essentially inactive without a dual activation process[1] that is not fully understood and the physiological TK substrates in the heart are not known. We have introduced the DtoV mutation in *C. elegans* TwcK and measured the phosphotransfer activity (**Figure 3.9**). $_{NL}TwcK_{CRD}$ containing both inhibitory regions exhibits negligible activity, but upon DtoV mutation ($_{NL}TwcK_{CRD}{}^{DtoV}$) the catalytic activity is restored to levels comparable to those of constructs lacking the NL ($TwcK_{CRD}$). This supported our conclusions that DtoV translates into altered interactions between the NL and the kinase core, resulting in significant release of the inhibitory NL.

Figure 3.9 Effect of DtoV exchange on titin-like protein from *C. elegans*.
a. A solid phase paper assay was used to quantify phosphorylating activity of twitchin kinase variants. **b**. Quantification of P81 paper phosphotransfer assay results. $_{NL}TwcK_{CRD}$ containing both inhibitory regions demonstrates only a trace amount of catalysis. Introduction of the DtoV mutation in $_{NL}TwcK_{CRD}$ ($_{NL}TwcK_{CRD}^{DtoV}$) augments kinase activity and catalysis levels become comparable to $TwcK_{CRD}$ containing only the C-terminal regulatory element.

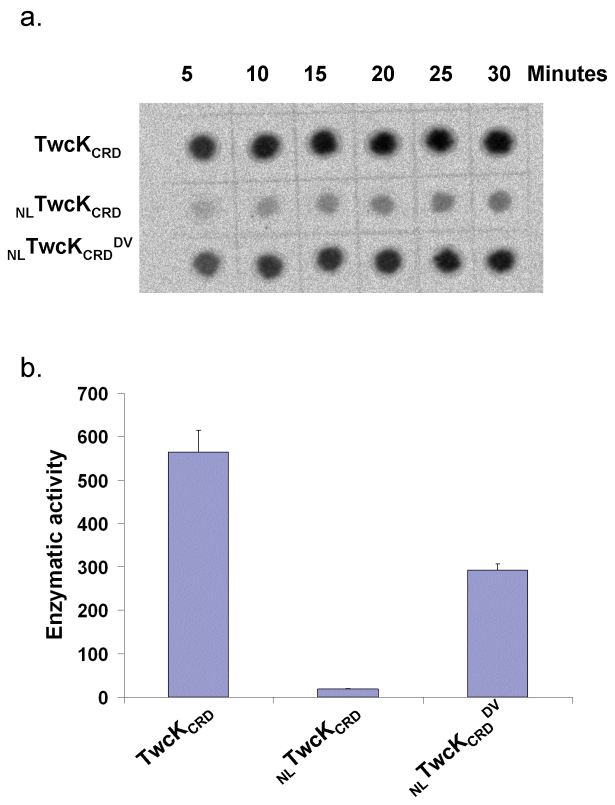

3.3.6 D24728V mutation enhances the interaction with MuRF1 and TK ubiquitination *in vivo*

Our investigations strongly imply the pathogenic nature of DtoV mutation by demonstrating the disruption of NL functionality. As NL was found to act as an inhibitor of MuRF1 binding, we have tested the effect of DtoV mutation on MuRF1 affinity. We have found that the DtoV mutation abolishes NL inhibitory effect on MuRF1 binding to A168-NL construct in GST pulldown assays using recombinant proteins; mutant A168-NL binds MuRF1 more strongly than the wildtype (**Figure 3.10a**). In order to evaluate the functional relevance of this observation *in vivo*, we

expressed GST tagged A168-TK^{WT} or A168-TK^{DtoV} and MuRF1 in differentiated rat cardiac myocyte H9C2 cells. Overexpression of MuRF1 resulted in reduced levels of A168-TK^{DtoV}, but did not affect wildtype protein levels (**Figure 3.10b**). To determine if the reduction in mutant protein levels was mediated via the ubiquitin proteasome pathway, we treated A168-TK^{DtoV} overexpressing cells with the cell permeable proteasome inhibitor MG-132. Proteasome inhibition rescued levels of mutant A168-TK in soluble fractions (**Figure 3.10c**). However, we observed significant accumulation of A168-TK^{DtoV} in insoluble fractions (**Figure 3.10c**), suggesting that the ubiquitin proteasome pathway is needed for removal of possibly misfolded A168-TK^{DtoV}. We conclude that the DtoV mutation within an A168-TK context enhances binding to MuRF1 *in vitro* and results in reduced protein levels due to enhanced degradation through the ubiquitin proteasome pathway in H9C2 cells.

Figure 3.10 DtoV exchange alters TK and MuRF1 interaction. **a**. Recombinant A168-NL^{DtoV} interacts more strongly with MuRF1 than WT construct in GST pulldown assays. **b**. Overexpression of MuRF1 in differentiated H9C2 rat cardiac myocytes reduced both total and purified quantities of GST-tagged A168-TK^{DtoV} fusion peptides as shown by Western blots with TK-specific antibodies. **c**. The proteasome inhibitor MG-132 partly restored MuRF1-induced A168-TK^{DtoV} protein depletion as shown by Western blots with TK-specific antibodies. In addition, proteasome inhibition by MG-132 caused accumulation of A168-TK^{DtoV} in the insoluble fraction, probably corresponding to misfolded proteins.

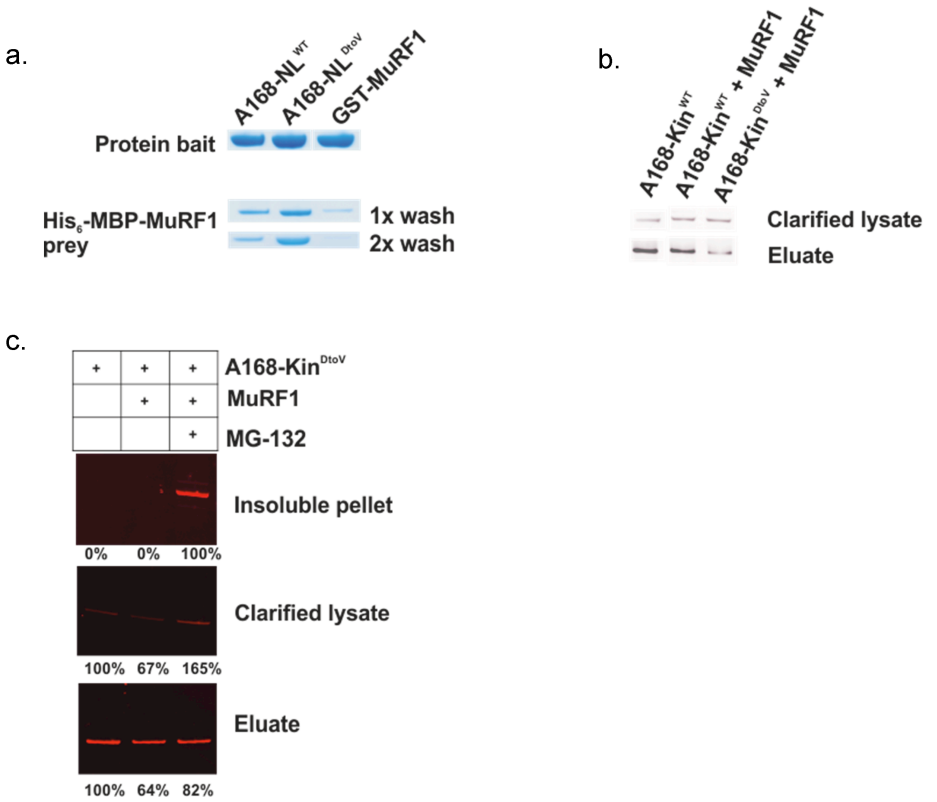

3.4 Discussion

The crystal structure of A170-M1 reveals an unexpected crucial role of a 23-residue NL linker motif for MuRF1 and TK crosstalk. The MuRF1 binding site in A168-A170 [6,22] and a newly discovered affinity region in TK are brought into close proximity by NL, which wraps around the N-lobe of the kinase, thus reducing the distance between two signaling platforms. The observed packing mainly arises from interactions between the highly conserved helical NYD motif located in a junction between the A170 domain and TK. Intriguingly, a rare SNP, rs200675195, results in a

D24728V exchange precisely in this motif. To date, the NHLBI GO Exome Sequencing Project has identified rs200675195 in 5 individuals. The here-represented cohort is enriched in samples from patients with heart, lung and blood disorders. Unfortunately we were not able to obtain clinical characteristics of these patients. However, structural analysis of DtoV effects by NMR and SAXS demonstrated that this exchange increased interdomain flexibility and abolished NL-TK interaction and thereby releasing the inhibitory NL effect in the homologous invertebrate TwcK. Taken together, our structural observations point to the pathogenicity of the DtoV mutation, adding to the evidence accumulated in recent years that mutations in *TTN* are an important genetic contributor to DCM (Gerull et al., 2002, Gerull et al., 2006, Hermann et al., 2012).

To explore the pathogenic nature of the DtoV exchange we have sequenced the *TTN* exon 358 from 200 cardiomyopathy patients. This exon encodes TK and a binding site for MuRF1 in the section immediately N-terminal to the kinase. Our *TTN* genetic screen identified rs200675195 co-segregating with the disease in a small family affected by DCM. The second genetic variation in a gene possibly linked to DCM, rs201763096 as identified by whole exome analysis in nexilin, has a frequency above the proposed cut-off for pathogenic DCM variants and was predicted to be benign. However, future studies will need to address the relative contributions of DtoV and rs201763096, because individuals carrying more than one rare (MAF <1%) sarcomeric allele have a higher risk of adverse cardiovascular events (Bick et al., 2012).

At the molecular level we have found that DtoV abolishes the inhibitory effect of NL and results in enhanced MuRF1 binding. The latter translates *in vivo* into enhanced MuRF1-mediated titin degradation by the ubiquitin-proteasome pathway. Speculatively, increased ubiquitination could result from both enhanced binding and increased flexibility between two MuRF1 affine modules, A168-A170 and TK, resulting in misubiquitination of TK surface lysines that would be otherwise inaccessible for MuRF1 in rigid WT protein. This phenomenon *per se* could lead to the accumulating loss of mutant titin, resembling the findings in the Herman *et al*. (2012) study where nonsense mutations of titin were identified as a major mutational group possibly causing DCM through haploinsufficiency or by means of a dominant

negative mechanism. Furthermore, we have found that A168-TK^{DtoV} accumulates in insoluble aggregates when the ubiquitin-proteasome pathway is inhibited, indicating that mutant titin might have a folding defect and active removal of misfolded proteins is needed to prevent the pathological accumulation of aggregates. This pathway resembles the clinical findings in autosomal dominant inclusion body myopathy associated with Paget disease of the bone and frontotemporal dementia (IBMPFD) patients. IBMPFD is a late-onset genetic multisystem disorder leading to dilated cardiomyopathy with inclusion bodies formed of ubiquitinated mutant protein (Hubbers et al., 2007). Taken together, our data indicate that the possible pathomechanism of DtoV mutation involves loss and/or accumulation of mutant protein in pathogenic insoluble aggregates.

In summary, our combined structural-functional analysis provides the first evidence that TK mutation is involved in human cardiomyopathy in a mechanism likely to involve functional crosstalk with MuRF1. Discerning between pathogenic or benign rare genetic variants due to unexpected variability of the human genome represents a challenge in the clinical setting (Mestroni and Taylor, 2013). Only very rarely does linkage data alone provide a definitive answer and therefore additional approaches should be taken. The structure-driven approach carried out in this work to assess the pathogenicity of DtoV could be applied to differentiate other rare benign genetic variants versus pathogenic mutations in DCM.

Chapter 4

Functional and structural consequences of I10 domain mutation associated with arrhythmogenic right ventricular dysplasia

4.1 Introduction

Arrhythmogenic right ventricular cardiomyopathy (ARVC), dilated and hypertrophic cardiomyophaties are the three major types of hereditary cardiomyopathies (CMs). While they all share pump failure at late disease stages, ARVC manifests early with life-threatening arrhythmias, making it the major cause of sudden cardiac death in the population aged below 25 years (Wichter et al., 2005). Genetic screening for preclinical diagnosis is central to ARVC management (Sen-Chowdhry et al., 2007). Accordingly, much emphasis has been given to identifying the gene mutations causing ARVC and the cellular pathways involved. Nine ARVC genes have been identified to date (*TGFB3*, *RYR2, TMEM43, DSP, PKP2, DSG2, DSC2, JUP, TTN*), of which five (*DSP, PKP2, DSG2, DSC2,* and *JUP*) encode proteins integral to cell-cell junctions at the intercalated disk. This finding has led to the belief that, mechanistically, ARVC results from a perturbed desmosomal force transmission. However, about 50% of ARVC affected families that undergo genetic screening do not show any linkage to known chromosomal loci (Sen-Chowdhry et al., 2007). Consequently, there is an acute need for the identification and validation of new causes of ARVC.

Recently, the importance of the titin gene (*TTN*) in ARVC has started to emerge (Taylor et al., 2011). In a recent study of 38 ARVC affected families, a T2850I[5] *TTN* allele demonstrated complete co-segregation with the ARVC phenotype. Data suggested that the T2580I mutation causes destabilization of the titin immunoglobulin domain I10, to where it maps, causing augmented vulnerability of the titin protein to proteolysis (Taylor et al., 2011; Anderson et al., 2013,). Taylor et al. showed that the HSQC spectrum of the mutated I10 domain ($I10^{T2580I}$) is a

[5] If otherwise not indicated, titin residues are numbered according to the reference sequence protein entry NP_003310

composite of two sets of signals: a main set of well dispersed signals similar to those present in the WT protein and a second set with a reduced chemical shift dispersion, indicative of a poorly folded state. NMR findings were in good agreement with chemical denaturation experiments that exploited the native fluorescence of the single tryptophan residue in the hydrophobic core of I10. In hydrophobic environment Trp has a high quantum yield, which is reduced by exposure to a hydrophilic environment upon denaturation. Unfolding experiments revealed a diminished intrinsic fluorescence of $I10^{T2580I}$, with little fluoresence change upon denaturation. Taken together, the investigations by Taylor et al. led to the conclusion that, at least, a fraction of $I10^{T2580I}$ is unfolded in *in vitro* samples. Anderson et al. studied the kinetic and mechanical stability of I10 and $I10^{T2580I}$ using single molecule force spectroscopy. They showed that the mutation decreases the force required for mechanical unfolding and increases the rate of unfolding by 4-fold, concurring with Taylor et al. in their conclusions of the overall pathomechanism of the T2580I mutation.

Despite these available studies, little understanding exists to date of the molecular alterations induced by this mutation and its implications *in vivo*. Thus, in this work, the disease mechanism of T2850I in ARVC is investigated by applying structural analysis of wild-type and mutated forms of the protein as well as transfection studies *in vivo*. Insights into T2850I mutation could not be inferred from the current structural data on titin's I-band. Firstly, the T2850I mutation is located in the proximal, constitutive I-band section of titin (**Figure 4.1**). Based on a key set of structural features within the domains and their linkers (Marino et al., 2005) Ig domains from this region belong to so called "N-variable" type, characterized by the short BC and FG loops, reduced number or absence of prolines at the N-terminal A strand and high sequence variability. However, all known structures of Ig-tandems from titin represent the "N-conserved" type. Characteristic features of this domain type: longer FG β-hairpins and prevalence of a PP motif at the N-terminal A strand orchestrate the interdomain orientation as crystal structures revealed (von Castelmur et al., 2008). Therefore reliable estimations could not be made for this I-band region based on published crystal structures. Taken together structure of I9-I11 would be needed for reliable estimation of T2850I mutational effects.

Figure 4.1 Domain organization of cardiac titin's I-band region.
Domains are as follows: Ig domains are in red; unique sequences in blue; Fn3 domains in white, PEVK region in yellow. The PEVK spring region is flanked on either side by Ig tandems (termed "proximal" and "distal" according to their distance to the Z-disc). The I10 domain affected in ARVC is highlighted in pale green; boxed regions indicate borders of crystallized titin fragments Z1Z2 (Marino et al., 2006), I1 (Mayans et al., 2001) I9-I11, I65-I70 (von Castelmur et al., 2008), I91 citation (Stacklies et al., 2009).

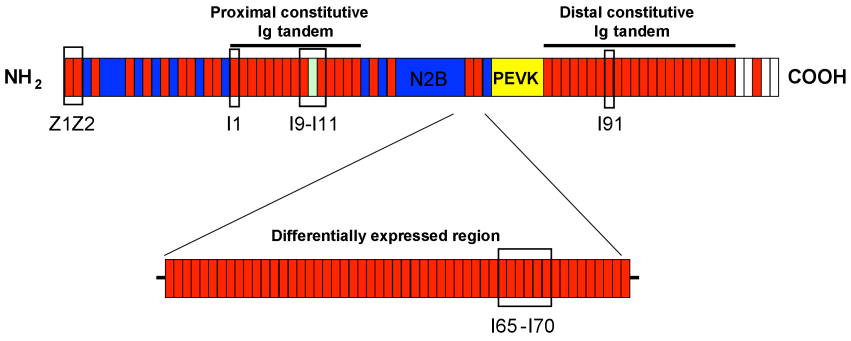

4.2 Materials and Methods

4.2.1 Cloning

Titin gene fragments encoding I9-I11 (residues 2749-3009 of the titin reference sequence NP_003310) and I10 (residues 2835-2895) were PCR amplified from a randomly primed cDNA library of human skeletal muscle (**Table 4.1**). Genes were then used as a source of wild-type I7-I13 fragments (residues 2560-3189), and the latter as source of I9-I11 and I10 coding fragments. For protein expression, encoding fragments were inserted into the pETM11 vector (Bogomolovas et al., 2009) through NcoI/Acc65I restriction sites. All constructs carried an N-terminal His_6-tag and a TEV protease cleavage site. Upon tag removal, the GAM tripeptide remained at the N-terminus of recombinant proteins after the tag removal. A valine residue was inserted into the C-terminus of β-strand G in domain I11 to facilitate crystallization of I9-I11.

Table 4.1 PCR primers used in the cloning of wild-type and mutant titin I-band fragments.
Non-complementary nucleotides: restriction sites, stuffer sequence and mutation site are in capital letters.

Construct	Primers
I9-I11^{WT}	F. primer: GATC CCATG gttaaaatcattaaaaaaccgaaagatgtgaccg R. primer: GATC GGTACC ctactaaacatacagggttgcggtgctggttgc
I9-I11^{TtoI}	F. primer: GATC CCATG gttaaaatcattaaaaaaccgaaagatgtgaccg R. primer: GATC GGTACC ctactaaacatacagggttgcggtgctggttgc F. mut. primer: aaaaccatgaaaaatattgaagtgccggaaaTtaaaaccgccagctttgaatg cgaagtgagc R. mut. primer: gctcacttcgcattcaaagctggcggttttaAtttccggcacttcaatattttt catggtttt
I10^{WT}	F. primer: GATC CCATG gaaaccctgcatattaccaaaaccatgaaaaatattgaagtgccggaaac taaaaccgcc R. primer: GATC GGTACC ttattaggtaacggtcagggttgcgctaacctgatcattaccgcaaac aaaggtata
I10^{TtoI}	F. primer: GATC CCATG gaaaccctgcatattaccaaaaccatgaaaaatattgaagtgccgga aaTtaaaaccgcc R. primer: GATC GGTACC ttattaggtaacggtcagggttgcgctaacctgatcattaccgcaaac Aaaggtata

4.2.2 Protein expression and purification

Proteins were expressed using BL21 *E.coli* cells in TB (12g/L tryptone, 24 g/L yeast extract, 4 mL/L glycerol, 17 mM KH_2PO_4, 72 mM K_2HPO_4) medium. Cells were grown at 37 °C to an OD_{600} = 1, induced with 0.2 mM IPTG and expression allowed to proceed overnight at 18 °C. Cells were harvested by centrifugation at 4 °C, washed with Mg^{2+}/Ca^{2+} free PBS (8g/L NaCl, 0.2g/L KCl, 1.44g/L Na_2HPO_4, 0.24g/L KH_2PO_4), repelleted and frozen at -20 °C. For purification, the cell pellet was resuspended in lysis buffer (25 mM HEPES, 250 mM NaCl, 10 mM Imidazole, 0.2% NP-40, 2 mM β-mercaptoethanol, pH 7.5) supplemented with EDTA-free protease inhibitor cocktail (Roche). After resuspension, the mixture was supplemented with 1 mg/mL lysozyme, 50 μg/mL DNAse I and 5 mM $MgSO_4$, sonicated and centrifuged at 30000 g for 30 min at 4 °C. The supernatant was loaded through 0.22 μm filter onto Ni^{2+}-NTA beads (Qiagen) that had been previously equilibrated in lysis buffer. Beads were washed with 10 x bead volumes of lysis buffer, subsequently with lysis buffer without detergent and eluted in 3 x bead volumes of elution buffer (25 mM HEPES, 250 mM NaCl, 300 mM Imidazole, 2 mM β-mercaptoethanol, pH 7.5). Eluted

fractions were exchanged to TEV digestion buffer (25 mM Tris, 50 mM NaCl, 5 mM β-mercaptoethanol, pH 7.5) using a HiPrep 26/20 Desalting column connected to an Äkta prime chromatography system (both GE Healthcare Life Sciences). His_6-tagged TEV protease was then added and the mixture incubated overnight at room temperature. Remaining contaminants, uncleaved products, affinity tag and protease were removed from the cleaved protein in a second, subtractive Ni^{+2}-NTA purification in TEV digestion buffer. Obtained preparations were concentrated (membrane cut-off 10 and 30 kDa for I10 and I9-I11 constructs, respectively) and further purified on a HiLoad 16/60 Superdex 75 prep grade column in crystallization buffer (20 mM HEPES pH 7.3, 50 mM NaCl, 0.5 mM TCEP). The I9-I11 sample was concentrated to 12 mg/mL and I10 to 24 mg/mL (according to A_{280}) and stored at 4 ^{o}C until further use. Purity was confirmed by SDS-PAGE.

For NMR studies, I10 was produced in M9 medium with $^{15}NH_4Cl$ as source of nitrogen and ^{13}C glucose as carbon source. Protein expression and purification was performed as described above for the unlabeled protein. Gel filtration was performed in NMR buffer (20 mM Tris pH 7, 50 mM NaCl, 0.5 mM TCEP, 0.2%NaN_3). For NMR studies, the sample was concentrated to 2 mM.

4.2.3 Differential scanning fluorimetry

The melting temperatures of the I10 domain and its variants were determined by differential scanning fluorimetry (DSF). Measurements were performed in triplicate on a Mx3005P Real-Time *PCR* System (Stratagene). The fluorescence of SYPRO Orange (Invitrogen) was monitored using custom FAM (492 nm) and ROX (610 nm) filters for excitation and emission, respectively. Measurements were performed in optical 96-well plates (Applied biosystems); each well contained 25 µL mixture consisting of 5 µM protein, 15X SYPRO Orange in assay buffer (100 mM HEPES pH 8, 150 mM NaCl). Fluorescence was recorded at 1 °C/min temperature ramp from 25 to 95 °C. The melting profiles recorded were analysed the with MATLAB technical computing package using a script for the fitting of the Boltzmann

equation with linear pre- and post- transitional fluorescence shifts as described (Matulis et al., 2005).

4.2.4 Crystallization and crystal structure determination of I10

The crystallization screening of I10 was performed at the BZH (Biochemie-Zentrum Heidelberg) crystallization platform using a Phoenix RE (Rigaku) nanolitre crystallization robot. The screening was performed in 96-well Intelliplates (Art Robbins Instruments) at 18 °C, using the vapour diffusion method in sitting drops containing 500 nL protein stock and 500 nL of mother liquor. Initial crystals appeared in 0.2 M $CaCl_2$, 20% [w/v] PEG 3350 after four days. The crystals were optimized manually in 48-well VDX plates (Hampton Research) at 20 °C in hanging drops consisting of 1 µL protein solution at 24 mg/mL and 1 µL of mother liquor. Crystals used for X-ray diffraction grew in two conditions: [A] 0.2 M $CaCl_2$, 30% [w/v] PEG 3350, 0.1 M Tris pH 7.5, 3% [v/v] Isopropanol; and [B] 0.2 M $CaCl_2$, 25% [w/v] PEG 8000, 0.1 M Tris pH 7.5. Selected crystals were cryoprotected by soaking in mother liquor supplemented with 30% [v/v] glycerol before being flash frozen in liquid N_2.

X-ray diffraction data were collected on beamline I24 [A] and I04-1 [B] at the Diamond Light Source synchrotron (Didcot, Oxfordshire, UK) using a PILATUS 6M [A] or PILATUS 2M [B] photon counting detector (Dectris, Baden, Switzerland). Data processing was performed using XDS/XDSCALE (Kabsch, 2010) or SCALA (Evans, 2006) for [A] and [B] crystal forms, respectively. Table summarizing data collection and refinement is presented in the corresponding result subsection.

Phasing of the crystal structure from condition [B] was done by molecular replacement with Phaser (McCoy, 2007) using as a search model the NMR solution structure of I10 obtained in this study (see below). The model was manually rebuilt in Coot (Emsley et al., 2010) and refined using phenix.refine (Adams et al., 2011) treating each Ig domain as a TLS (Translation/Libration/Screw) group. The structure so calculated was used as search model in molecular replacement to phase the high resolution X-ray diffraction data collected from crystals grown in condition [A]. Model refinement was as above, except that automatic model building was included

using ARP/wARP (Langer et al., 2008). This overall strategy for structural elucidation was chosen because data obtained from I10 crystal in condition B had 1 protein copy per asymmetric unit, whereas crystal in condition A contained 16 copies per asymmetric unit. The success of molecular replacement depends on the quality and completeness of the search model, and generally becomes more difficult as the number of components in the asymmetric unit increases (McCoy, 2007). In addition, NMR structures score poorer in molecular replacement. Often NMR structure of same protein fails when used as a search model for molecular replacement (Chen et al., 2000). Therefore, we first obtained the best possible crystallographic search model by solving the phasing of the simplest asymmetric unit (containing just 1 copy) using an NMR model and then used the resulting crystallographic model as a search model to phase the data at higher resolution but with a more complex phasing problem (16 copies).

4.2.5 Crystallization and crystal structure determination of I9-I11

Rhys Williams and Olga Mayans, University of Liverpool carried out the crystal structure elucidation of I9-I11. In brief, crystals were grown at 19 °C in sitting drops using 96-well Intelliplates (Art Robbins Instruments) and a nano-drop liquid-dispensing robot (Screenmaker 96+8, Innovadyne). Drops consisted of 200 nL of protein solution (12-16 mg/mL) and 200 nL of mother liquor. Diffraction quality crystals were obtained from [condition C] 0.1 M Tris HCl pH 8.5, 30 % [w/v] PEG 4000, 0.2 M $MgCl_2$ and [condition D] 0.1 M Bis-Tris Propane pH 8.5, 20 % [w/v] PEG 3350, 0.2 M sodium acetate. Selected crystals were manually excised from the respective clusters, mounted in litho-loops and cryoprotected by soaking in mother liquor supplemented with 20% [v/v] glycerol before being flash frozen in liquid N_2.

X-ray diffraction data were collected on beamline I02 [A] and I104 [B] at the Diamond Light Synchrotron Source (Didcot, Oxfordshire, UK). Data collection and experimental setup are summarized in table 3. Data processing was performed using iMosflm (Battye et al., 2011) and SCALA (Evans, 2006). Phasing was by molecular replacement in Phaser (McCoy et al., 2007) using other titin domains as search models (namely, PDB ID 3CLY and 2YZ8 with ~ 30% sequence identity). The

molecular replacement solution was improved by automatic model building using ARP/wARP (Langer et al., 2008) in warpNtrace mode with side chain docking. Manual model manipulation used Coot (Emsley et al., 2010). Refinement was in phenix.refine (Adams et al., 2011) with each Ig domain defined as a separate TLS group.

The crystal structure of I9-I11 in condition D was solved by molecular replacement using the crystal structure of I9-I11 from condition A as search model. The position of individual Ig was adjusted by rigid body refinement in phenix.refine (Adams et al., 2011). The model was further manually built using Coot (Emsley et al., 2010) and refined in phenix.refine (Adams et al., 2011) treating each Ig domain as an individual TLS group.

4.2.6 NMR studies of wild-type and mutant I10

This work was in collaboration with Dr. Bernd Simon at EMBL, Heidelberg. NMR spectra were acquired at 22 °C on Bruker DRX500, Avance III 600 and Avance III 700 spectrometers. Proton chemical shifts were referenced to the internal water signal and corrected for temperature, salt and pH, whereas heteronuclear resonances were indirectly referenced based on gyromagnetic ratios. All spectra were processed with nmrpipe and analyzed with nmrview (Johnson, 2004). Sequential backbone NH, N, CO, Cα and Cβ resonances were assigned from the following 3D experiments: HNCO, HNCA, HNCACB, CACB(CO)NH. For sidechain assignment the following experiments were performed: HBHA(CBCACO)NH, H(CCCO)NH-TOCSY, (H)C(CCO)NH-TOCSY and H(C)CH-TOCSY. Distance constraints for structure calculation were obtained from a simultaneous 3D $^{15}N/^{13}C$ -edited [^{1}H, ^{1}H]-NOESY (H_2O) spectrum with a mixing time of 120ms. NH hydrogen bonds were determined by acquiring a ^{1}H-^{15}N HSQC spectrum after dissolving lyophilised protein in D_2O. ^{15}N T1, T2 and heteronuclear NOE data were acquired with an interleaved data acquisition scheme at 500 MHz. S^2 Lipari-Szabo model-free order parameter values where calculated with Tensor (Dosset et al., 2000).

Structures were calculated in Aria1.2 (Bardiaux et al., 2008) using modifed annealing protocols. Dihedral angle restrains were derived from the program TALOS+ and NOE connectivities were assigned manually and further calibrated in 8 iterations, calculating 20 structures in first seven and 100 structures in last iteration. NOE restraints were used with a soft square-well potential, using an energy constant of 50 kcal mol^{-1} $Å^{-2}$; dihedral angle restrains were applied with energy constants of 200 kcal mol^{-1} rad^{-2}. The bounds for hydrogen bond restrains were 1.8–2.3 Å for H_N–O distances and 2.8–3.3 Å for N–O distances. The final ensemble of structures was refined in an explicit water shell and the statistics of the 10 lowest energy structures was analyzed.

4.2.7 Transgenic muscle

The work here described was carried out in collaboration with Muzamil Majid Khan at University of Applied Sciences Mannheim. All animal experiments with wild-type C57BL/*6* mice were approved by German authorities and the local committee (Regierungspräsidium Karlsruhe). For in vivo visualisation WT and mutant I7-I13 fragments were cloned into pEGFP-C1 vector, resulting in N-terminal fusion with EGFP. Transfection of GFP tagged I-band titin fragments into *tibialis anterior* muscles was done as previously described (Dona et al., 2003, Roder et al., 2010). Mice were anesthetized with an intraperitoneal injection of Rompun (Bayer Pharma; active substance ketamine; 5mg/kg) plus Zoletil 100 (Vibrac Laboratories, active substances tiletamine and zolazepam; 30mg/kg). After hair removal, the skin and fascia overlying the *tibialis anterior* were incised. One electrode plate was inserted underneath the muscle, 10 µg of expression plasmid were injected into the *tibialis anterior* muscle and a second electrode plate was placed above the muscle. Five 25 V and 20 ms long electric pulses were applied (ECM 830; BTX Genetronics). The electrodes were removed, and the wound was closed. Ten days later, mice were euthanized by cervical dislocation and transfected muscle sections were counterstained with Texas Red®-X Phalloidin and visualized under a laser scanning confocal microscope or GFP expression was detected using Western Blot with anti GFP (abcam ab290) antibody as described (Moriscot et al., 2010).

4.2.8 Biomechanical measurements on cardiac myocytes

This work was carried out in collaboration with Emmy Manders at VU University Medical Center, the Netherlands. The donor heart sample was obtained after informed consent and with approval of the local ethical committee, conforming to the principles outlined in the Declaration of Helsinki. The sample was immediately frozen and stored in liquid nitrogen. Cardiomyocytes were mechanically isolated from a left ventricular donor heart to study sarcomeric function as described previously (Kooij et al., 2010, van der Velden et al., 2003, van Dijk et al., 2012). Briefly, tissue was thawed in relaxing solution and cardiomyocyte membranes were permeabilized with 0.5% Triton X-100. A single cell was attached to a length motor and a force transducer and sarcomere length was set at 2.2 µm. Total force generating capacity (F_{tot}) was determined by transferring the cardiomyocyte to activating solution (calcium concentration [Ca^{2+}] of 31.6 µmol/L (Fabiato and Fabiato, 1978). When the steady force was reached, the cell was shortened to 70% of its original length, followed by a quick re-stretch to its original length. The rate of force redevelopment (κ_{tr}) was determined by fitting a single exponential through the force redevelopment curve (Sieck and Prakash, 1997, Brenner and Eisenberg, 1986). Passive force (F_{pas}) was determined by shortening the cell to 70% of its original length in relaxing solution. Active force (F_{max}) was calculated by subtracting F_{pas} from F_{tot}. All experiments were performed at 15 °C. To determine tension, force was normalized to the cross sectional area of the cell.

The calcium sensitivity of force was determined by placing the cell in solutions with incremental Ca^{2+} concentrations. Forces at submaximal Ca^{2+} concentrations were normalized to maximal force obtained at a Ca^{2+} concentration of 31.6 µmol/L. The pCa_{50}, i.e. the Ca^{2+} concentrations at which 50% of the maximal force is reached, was calculated by fitting a modified Hill equation through the data points. Subsequently, the cell was incubated for 30 minutes with either the WT or the mutant fragment (concentration of 10 mg/ml in relaxing solution). After these, the measurements of maximal tension, passive tension, $\kappa_{tr,}$ and calcium sensitivity were repeated.

4.3 Results

4.3.1 Expression and purification of I-band titin Ig-tandems

Early in this work, we identified a flaw in the I10 construct design used in previous studies (Taylor et al., 2011; Anderson et al., 2013). Those reports used an N-terminally truncated form of the I10 domain that missed β-strand A. It is known that this secondary structure element is structurally important for the Ig folds of titin (Pfuhl et al., 1997). Thus, we anticipated that the misconstructed I10 variants might have led to unreliable results. The I10 construct used in this study was N-terminally extended by 6 amino acids with respect to that in Taylor et al. to include the complete structural N-terminus of the fold (**Figure. 4.2**).

Figure 4.2 Phasing of I10 domain constructs. Alignment of N-termini sequences of I10 domain constructs used in Taylor et al., and current work. Secondary structure elements are indicated according crystal structure (see below). The subsequent elucidation of the I10 crystal structure revealed that the domain N-terminus is formally defined by residue L6 in the sequence below.

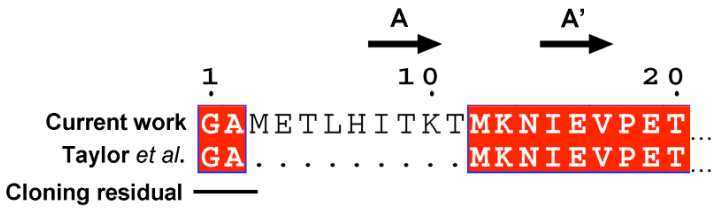

Recombinant immunoglobulin domain tandems from human I-band titin, both native and isotope labelled, were successfully over-produced in *E.coli* cultures. Protein samples were obtained in high yield (~20 mg/L medium) and at high purity suitable for structural studies (**Figure 4.3**). Gel filtration profiles for I10 (**Figure 4.3A**) and I9-I11 (**Figure 4.3B**) indicated that the resulting samples were well-folded, monomeric protein preparations (as indicated by elution volumes).

Figure 4.3 Purification of human I-band titin Ig-tandems.
Gel filtration chromatogram and associated SDS-PAGE of **A**: I9-I11^{WT} and **B**: I10^{WT}.

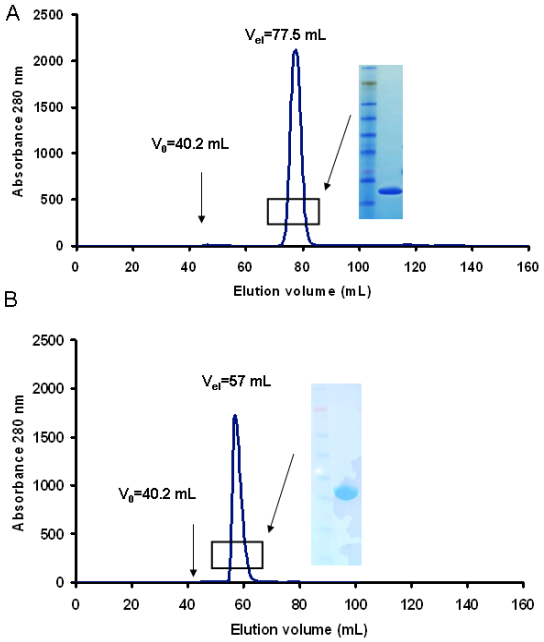

4.3.2 DSF studies of I10

Global stability of I10 domains was measured using DSF. This technique allows determination of melting temperature leading to the externalization of the hydrophobic core marking the domain unfolding. Therefore this method was applied only for single domain construct I10.Both wild-type and mutant I10 gave sharp, directly interpretable single transition melting profiles, however mutation significantly reduced the melting temperature by 10.9 °C (**Figure 4.4A**).

These findings indicate that I10 fold can well accommodate the mutation although at the cost of a weakened hydrophobic core. It is noteworthy that robustness of titin's Ig domains might be a general feature as is was shown that the Z1 domain can accommodate extensive FLAG tag insertion into the CD loop (Bruning et al., 2012). As obtained results does not align well with the extensive domain destabilization reported in pervious studies (Taylor et al., 2012; Anderson et al., 2013) the effect of improved domain borders was evaluated. Novel design of domain

boarders increased the melting temperatures of both: wild-type by 10.1 °C and mutant by 14.2 °C (**Figure 4.4B**). It was noteworthy that mutational effect was larger (Tm_{wt}-Tm_{mutant} =14.2 °C) between constructs used in Taylor *et al.*, than using optimally designed constructs (Tm_{wt}-Tm_{mutant} =10.9 °C).

Taken together, DSF data suggest that suboptimal design of domain boarders in Taylor *et al.* might have contributed to overestimation of the mutational effect on domain stability and, thereby, the contribution of molecular instability in the ARVC pathology.

Figure 4.4 DSF analysis of I10 domain stability. A. Melting curves of wild-type and mutant I10 proteins. T2850I exchange reduces melting temperature of I10 domain by 11 ° C, however still remaining far above the physiological temperature range. **B**. Differences in melting temperatures of I10 domain constructs used in Taylor *et al.*, and this study. Note the significant stabilization of protein constructs upon proper design of domain borders.

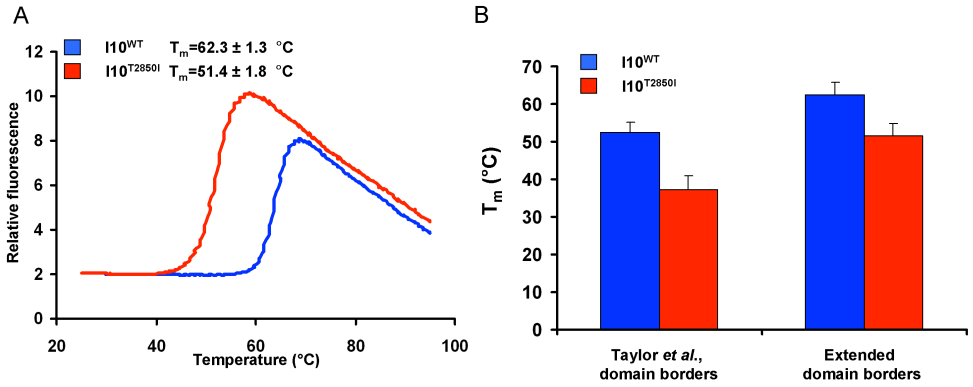

4.3.3 Crystal structure of $I10^{WT}$

Previous studies on the T2850I mutation (Anderson et al., 2013, Bogomolovas et al., 2009) provided only a phenomenological description of mutational effects on protein stability, but lacked molecular insights. Therefore, here the atomic structure of I10 was elucidated using X-ray crystallography. Wild-type and mutant I10 were

assayed in crystallization, but only the wild-type variant led to crystal formation (**Figure 4.5**).

Figure 4.5: Crystals of I10^{WT} grown in 0.2 M $CaCl_2$, 20% [w/v] PEG 3350

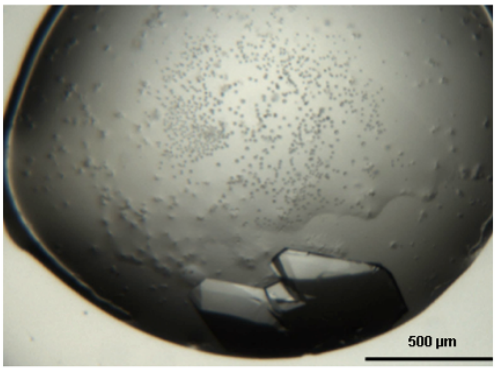

The manual optimization of the initial crystallization hit resulted in crystals of high diffraction quality and led to the recording of high resolution data (1.74 Å resolution) for I10^{WT} in space group $P2_12_12_1$ (condition B, **Table 4.2**). This crystal form was initially intractable by molecular replacement, because of the numerous protein copies in the asymmetric unit (14-16 copies estimated based on the calculated Matthews coefficient; Ref). Finally, this crystal form was resolved by molecular replacement using the crystal structure of I10 obtained from poorer quality crystals (2.0 Å resolution) in space group P1, but containing a single protein copy per asymmetric unit (**Table 4.2**).

Table 4.2 X ray data and model refinement statistics for $I10^{WT}$

	$I10^{WT}$ (A)	$I10^{WT}$ (B)
Space group	$P4_1$	$P2_12_12_1$
Cell dimensions: *a*, *b*, *c* (Å) a, b, g (°)	 31.2, 31.2, 93.9 90, 90, 90	 74.6, 136.2, 140.1 90, 90, 90
Solvent content (%)	51	46
Matthews coefficient ($Å^3$/Da)	2.49	2.27
Copies in ASU	1	16
X-ray data		
X-ray source	DIAMOND I24	DIAMOND I04-1
Detector	PILATUS 6M	PILATUS 2M
Wavelength (Å)	0.9464	0.9173
Detector-crystal distance (mm)	502	222
Resolution (Å)	26.00-2.00 (2.071-2.00)	29.65-1.738 (1.80-1.738)
Unique reflections	5665 (560)	145378 (13857)
R_{sym} (I) (%)	13.9 (34.13)	9.6 (71.4)
Multiplicity	2.2 (1.9)	7.5 (7.1)
Completeness, %	93.2 (91.95)	98.77 (95.19)
I/σ (I)	4.96 (2.38)	15.38 (2.77)
Refinement		
No. of reflections Working/test set	5215/449	143915/1455
Protein atoms/solvent molecules	696/123	11199/1625
Rfactor/Rfree, %	17.53/22.99	17.45/20.49
RMSD bond length, Å	0.007	0.007
RMSD bond angle, °	1.092	1.16

The following structural details of $I10^{WT}$ will be discussed on the basis of the $P2_12_12_1$ crystal form, elucidated at the highest resolution of 1.74 Å (**Figure 4.6**). Structural elucidation demonstrated that this crystal form contains 16 protein copies in the asymmetric unit. The self-rotation function calculated with POLARFN (CCP4) strongly implied two two-fold non-crystallographic axes: first orthogonal to the crystal ***b*** axis and forming an approximately 45° angle with the ***c*** axis (**Fig. 4.6A**), that can be directly recognized in the asymmetric unit (**Figure 4.6B**). Asymmetric unit consists of 4 square pyramid shaped I10 tetramers forming a hexahedron-like structure.

Figure 4.6 Non crystallographic symmetry in I10 crystal. A. Self-rotation function calculated with POLARFN (CCP4) in stereographic projection at κ=180°. Peaks arising from twofold symmetry axes are indicated in red (crystallographic) and green (noncrystallographic). **B**. Asymmetric unit of $I10^{WT}$ crystal. Four square pyramid-like tetramers of I10 forming the unit are highlighted in different colours.

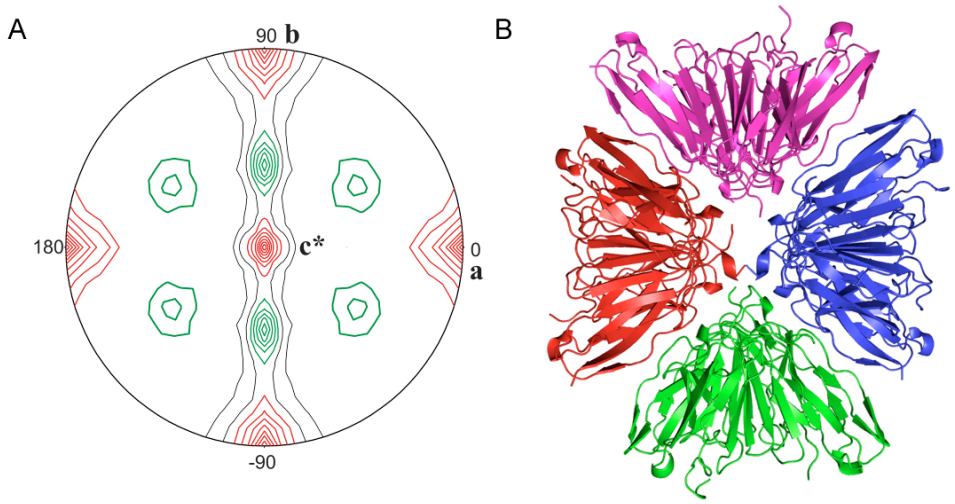

I10 exhibits an immunoglobulin I-type fold, comprising nine b-strands (A,A',B,C,C',D,E,F,G) organized in two b-sheets (A,B,E,D and A',G,F,C,C') that pack against each other in an antiparallel fashion. The affected threonine residue is located in a β-turn (residues P2848-K2851) connecting b-strands A' and B (**Figure 4.7A**). Noteworthy, identical loop conformation was observed in all protein copies obtained from two different crystallization conditions. According to its dihedral angles, this turn is classified as type II (Hutchinson and Thornton, 1994). This type of turns is sometimes called the "glycine" turn (Richardson and Richardson, 1989) as the residue *i+2* adopts a left handed 3_{10} helix conformation (ideal φ/ψ angles +90°/0°) that is sterically well tolerated only by glycine, which lacks a side chain.

Figure 4.7 Crystal structure of I10. A. Overall representation of $I10^{WT}$ β-sheets A'FCC'G and the ABED are coloured in red and blue respectively. Position of the T2850 mutation in the A'B b-turn is indicated by a purple sphere. **B**. Backbone representation of type II β-turn in A'B loop. Residues are numbered according protein sequence and β-turn naming conventions. Note the short hydrogen bond (16 kJ/mol according YASARA prediction) between carbonyl of *i+1* and sidechain of T2850 residue. Observed dihedral angles and ideal values of type II β-turn are given in table below. **C**. Hydrogen bonding stabilizing A'B loop. **D**. Ramachandran plot with T2850 residue in high-energy region. F. Distribution of *i+2* residues in A'B β-turns of proximal constitutively expressed titin I-band region. Note that most of the domains have side chain containing polar residues, whereas glycine is found only in approximately ¼ of the domains.

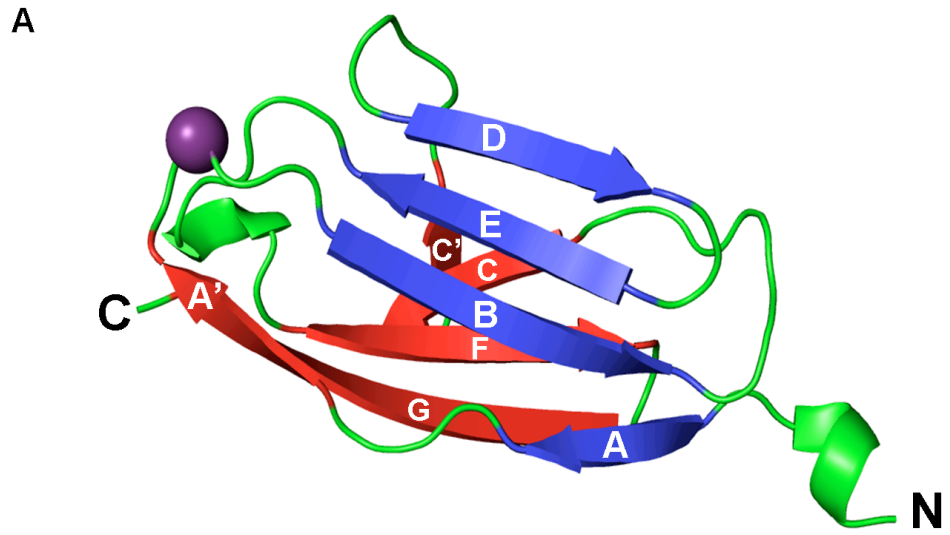

B

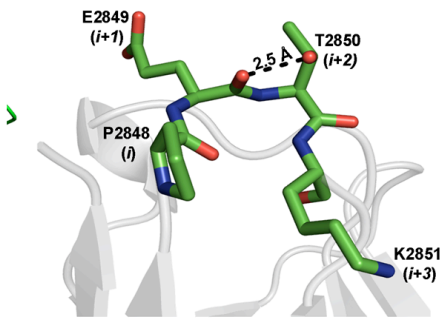

	Residue *i+1*		Residue *i+2*	
	φ angle (°)	ψ angle (°)	φ angle (°)	ψ angle (°)
$I10^{WT}$	-51.9	141.2	77.1	-7.9
Ideal angle	-60	120	80	0

C

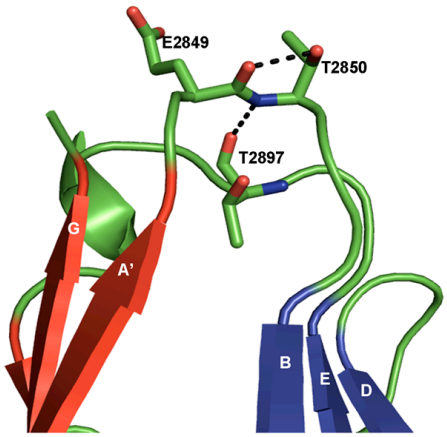

D

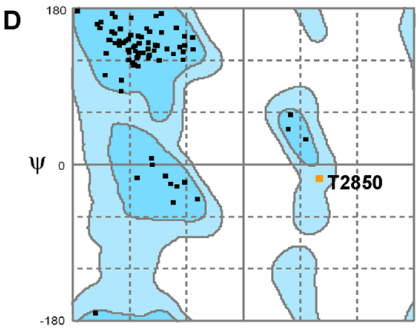

E

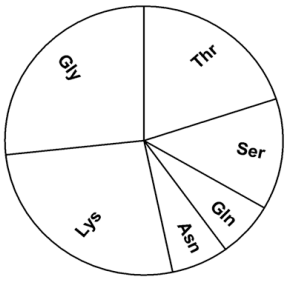

The sidechain C_β atom of *i+2* residue would sterically clash with the carbonyl group of preceding *i+1* residue. Thus about 76% of this type of turns has glycine and only 0.7% threonine in *i+2* position (Hutchinson and Thornton, 1994). However, in I10 such an "inconvenient" conformation is stabilized through two hydrogen bonds (**Figure 4.7C**). T2850 adopts a pseudoproline conformation by forming a hydrogen bond between its side chain hydroxyl and the carbonyl of the previous residue, E2849. The backbone position of T2850 is further stabilized through a hydrogen bond between the amide group of T2850 and the side chain hydroxyl of T2897 in EF loop. As a result, threonine in this position adopts a high-energy conformation within the generously allowed αL Ramachandran region. Speculatively, such atypical stabilization of type II β-turns between A' and B strands might be universal for the proximal constitutively expressed titin I-band region, as mostly polar residues are found in *i+2* position (**Figure 4.7E**).

In brief, the crystal structure of $I10^{WT}$ revealed that mutation affected residue T2850 resides in A'B loop, where it adopts atypical high-energy conformation that is stabilized through hydrogen bonding. Therefore T2850I mutation might have a strong destabilizing effect on I10 domain, by disrupting the predicted hydrogen bond between T2850 and E2849.

4.3.4 Crystal structure of I9-I11

The crystal structure of I10 revealed that the sidechain of T2850 is surface exposed (0.034 burial index as calculated with FoldX (Van Durme et al., 2011). Therefore, it could be involved in interactions with the preceding Ig domain and its mutation could lead to the destabilization of Ig-Ig interfaces. In order to address this question, the crystal structure of I10 flanked by its neighbouring Ig domains was elucidated to 1.53 Å resolution. Both wild-type and mutant constructs underwent crystallization screening, but only the wild-type yielded crystals. Rhys Williams and Olga Mayans, University of Liverpool carried out the crystal structure elucidation of I9-I11.

Figure 4.8 Appearance of initial I9-I11^{WT} crystallization hit *in situ* A. Crystals in condition A (0.1 M Tris HCl pH 8.5, 30 % [w/v] PEG 4000, 0.2 M $MgCl_2$); space group P1 **B**. Crystals in condition B (20 % [w/v] PEG 3350, 0.2 M sodium acetate); space group $P2_12_12_1$.

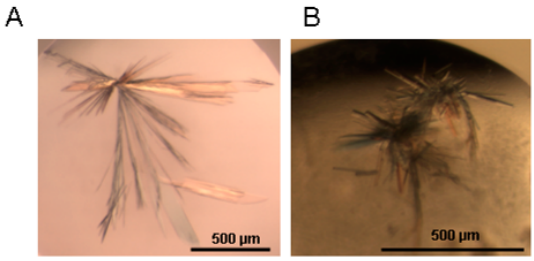

Two independent crystal structures of I9-I11^{WT} were solved during the course of this work (**Table 4.3; Figure 4.8**). The crystal structure obtained from condition B was chosen as reference in this study as it has the highest resolution of 1.53 Å.

Table 4.3: X-ray data and model refinement statistics for I9-I11

	I9-I11 (A)	I9-I11 (B)
Space group	P1	$P2_12_12_1$
Cell dimensions: *a*, *b*, *c* (Å) a, b, g (°)	 37.7, 42.4, 83.5 85.2, 79.8, 87.0	 42.3, 65.8, 108.4 90, 90, 90
Solvent content (%)	44	52
Matthews coefficient (Å^3/Da)	2.17	2.52
Copies in ASU	2	1
X-ray data		
X-ray source	DIAMOND I02	DIAMOND I04
Detector	PILATUS 6M	PILATUS 6M-F
Wavelength (Å)	0.9795	0.9795
Detector-crystal distance (mm)	347	285
Resolution (Å)	19.427-1.906 (1950-1.906)	41.83-1.53 (1.610-1.530)
Unique reflections	38254 (6392)	45488 (6392)
R_{sym} (I) (%)	7.6 (64.5)	5.8 (41.4)
Multiplicity	3.5 (3.4)	5.5 (5.1)
Completeness, %	96.61 (86.2)	97.5 (95.9)
I/σ (I)	11.3 (1.8)	12.6 (3.8)
Refinement		
No. of reflections Working/test set	38230/1151	45171/2687
Protein atoms/solvent molecules	4089/264	2131/543
Rfactor/Rfree, %	19.28/22.83	16.15/19.65
RMSD bond length, Å	0.08	0.006
RMSD bond angle, °	1.119	1.094

Figure 4.9 Crystal structures of I9-I11 A. Crystal structure solved from condition A, with two copies in asymmetric unit. The content of the asymmetric unit is shown. **B**. Crystal structure from crystallisation condition B with a single copy in asymmetric unit. This crystal structure is used as reference for the further discussion.

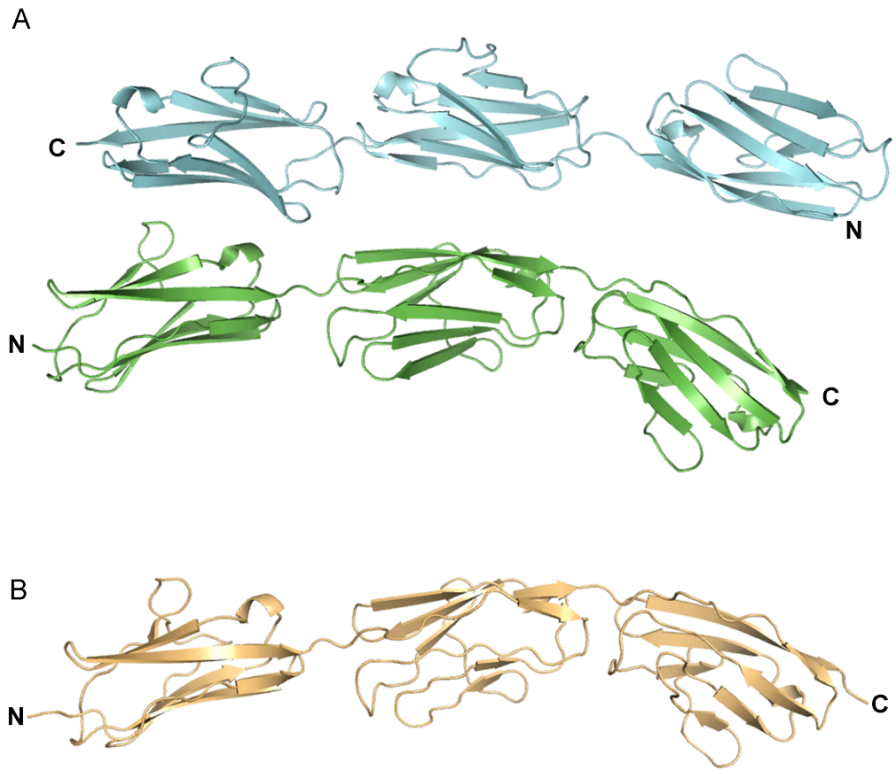

I9-I11 adopts an extended conformation (**Figure 4.9**) observed in other known titin Ig-tandems (Marino et al., 2006, Muller et al., 2007, von Castelmur et al., 2008, Mrosek et al., 2007). Features of Ig-Ig interfaces in I9-I11 orchestrate overall domain arrangement that differs from the known titin Ig-domains. A Short linker connecting the I9-I11 fragment was compared to all other of titin's Ig-tandems with similar interdomain connectors (**Figure 4.10**). In this work linkers were defined as regions with no secondary structure (coil) between G stand of preceding and A strand of following Ig domain, as determined with YASARA secondary structure assignment module. To start with, the crystal structure of I9-I11 revealed that interconnected domains do not adopt the "up-down" domain arrangement seen in other Ig-tandems from differentially expressed portion of titin I-band (von Castelmur et al., 2008) or A-band (Muller et al., 2007, Mrosek et al., 2007) (**Figure 4.10**). Indeed I9-I11 has a

smallest domain torsion angles ranging from 45° to 68°, whereas the angle between other domains ranges from 80 to 144 degrees.

Figure 4.10 Interdomain characteristics of titin Ig-Ig tandems. Upper section All known structures of titin Ig- tandems connected with short linkers were compared. The linker was considered random coil region (based on YASARA secondary structure assignment algorithm) between G and A' strands of subsequent Ig domains. Domain torsion angle was estimated between matched regions of CD loops. Tilt angle calculated between the largest axes of inertia. **Lower section**. Structures used for the comparison. Corresponding β-sheets are in red and blue.

	Linker sequence	Torsion angle (°)	Tilt angle (°)	Interface area (Å^2)	Distance (Å)
I9-I10[a]	-TL-	45.4 / 58.8 / 68.6	4.5 / 12.2 / 8.16	162.2 / 161.4 / 152.2	42.6 / 41.8 / 42.1
I10-I11[a]	-PI-	33.5 / 47.0 / 48.8	34.3 / 37.2 / 34. 3	327.3 / 311.7 / 317.7	37.0 / 37.0 / 37.4
I67-I68[b]	-EPP-	154.0	26.0	207.8	44.5
I68-I69[b]	-EPP-	153.5	9.4	267.1	42.9
A168-A169[c]	-[V]PA-	80.86/104.23	7.69/27.8	251.1/245.1	42.93/41.72
A164-A165[d]	-TP-	144.1	52.1	362.8	38.8

[a] Parameters are given in the following order: condition B copy A, condition A copy A, condition A copy B. [b] Based on 2RIK entry (von Castelmur et al, 2008). [c] Based on 2NZI (Mrosek et al., 2007) and 2J8H (Mueller et al., 2007). [d] Based on four ASU copies of 3LCY (Chen et al., unpublished)

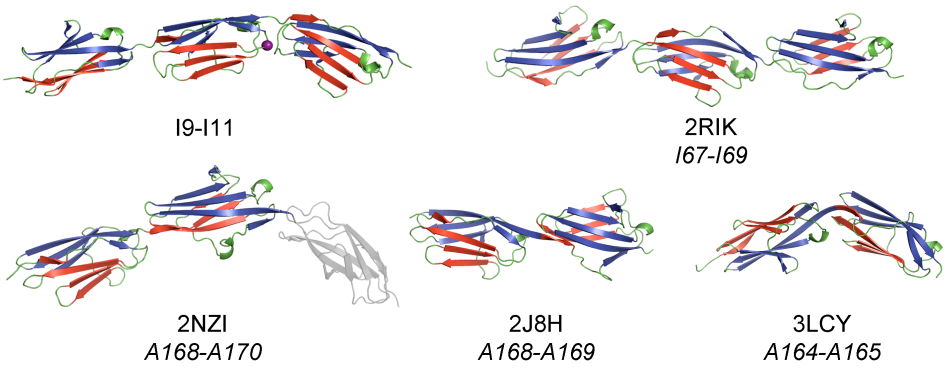

In contrast to all described Ig-tandems, I9-I11 consists of N-variable type domains, defined by the shortened BC and FG elements (Marino et al., 2005) (**Figure 4.11**). In the context of the titin chain, this would allow extended Ig-Ig interactions, as in Ig tandems from alternatively spliced region of titin's I-band these motifs are orchestrating "up-down" intradomain arrangement (von Castelmur et al., 2008). Thus, domains in the I9-I11 tandem can adopt small domain torsion angles and form extensive interfaces.

Figure 4.11 Superimposition of N-variable and N-conserved Ig domains from titin I-band. N-variable domains (I9-I11, I91) are in red N-conserved (I1, I65-I70) are in semitransparent gray. Note the short BC and FG loops of N-variable domains

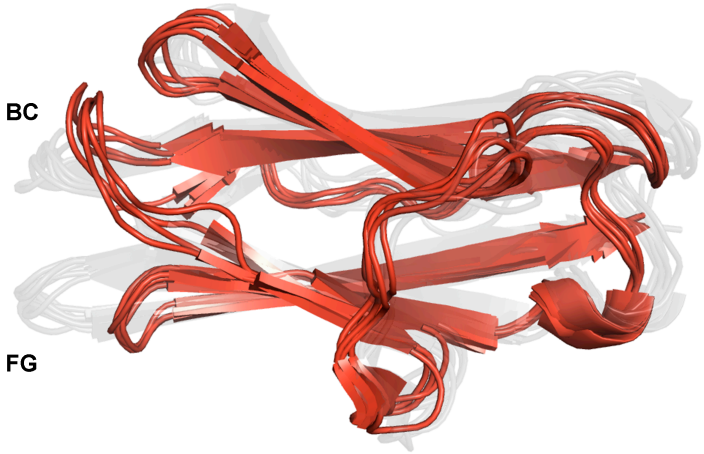

Mutation affected T2850 is buried (Burial of side chain 0.79, burial of main chain 0.82 calculated with FoldX (Van Durme et al., 2011)) within the extended I10-I11 interface. I10-I11 interaction is mediated by four potential hydrogen bonds, mainly from the A'B loop of I10 and the BC loop of I11 (**Figure 4.12B**). In Ig-tandem context T2850 residue preserves intradomain hydrogen bonds (with T2897 and E2849) observed in I10 crystal structure and in addition is hydrogen bonded with S2952 from BC loop of I11 domain. In contrast to the extensive I10-I11 hydrogen bond network, two hydrogen bonds mediate I9-I10 interface and only E2834-H2861 has non-local nature, connecting G strand of I9 and BC loop of I10 (**Table 4.4; Figure 4.12CB**).

Although domain interfaces in I9-I11 differ in hydrogen bonding patterns, both are mediated through conserved hydrophobic interactions. *i* residues (L2761 and P2848 for I9 and I10, respectively) of β-turn in AB loops form hydrophobic interactions with the residue in BC (H2861 and Y2948 for I9 and I10, respectively) loop of next Ig domain (**Figure 4.12BC**). Taken together T2850 is involved in both: intra- and interdomain organization of titin filament.

Figure 4.12 Crystal structure of I9-I11^{WT} A. Overall representation of I9-I11^{WT} crystal structure from the proximal Ig tandem segment in cartoon representation. I9-I11 consists of three connected immunoglobulin domains. Two β-sheets (consisting of A'FCC'G and ABED strands) forming the Ig-fold are in red and blue, respectively. The T2850I mutation is represented as a purple sphere. **B**. I9-I10 interface. L2758 and H2861 are forming the hydrophobic interaction. **C**. I10-I11 interface. Y2948 and P2848 involved in hydrophobic interaction are represented in thin lines.

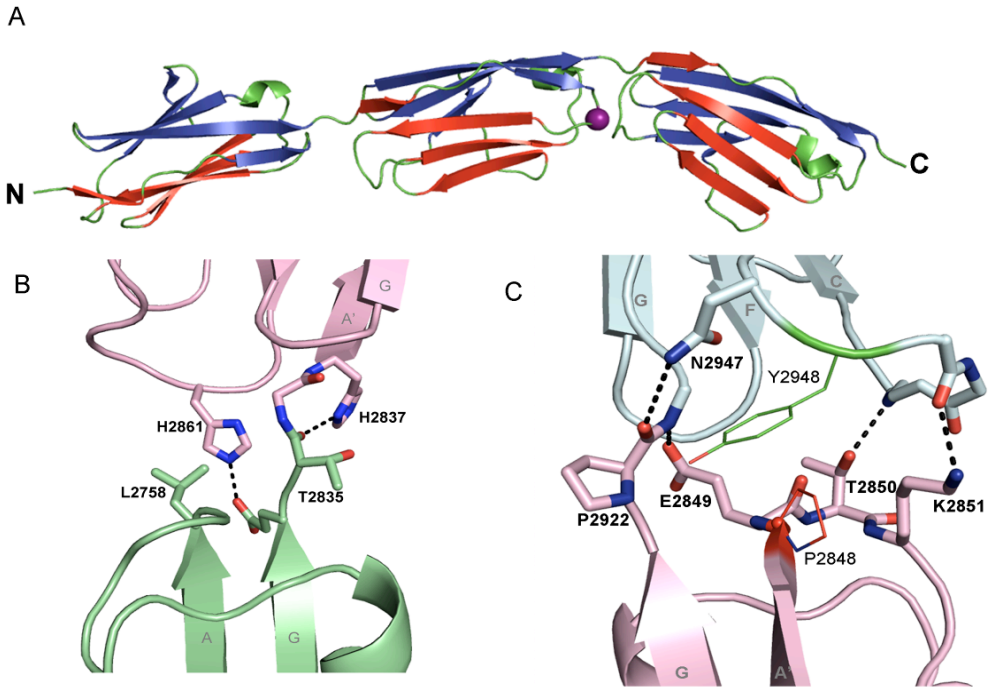

Table 4.4 Inter- and intradomain contacts in I9-I11

	Hydrogen bond	Distance (Å)	Energy (kJ/mol)	Hydrophobic interactions	Strength (AU)
I9-I11	$E2834_{OE1}$-$H2861_{NE2}$	1.49-1.81	13.7-25	L2761-H2861	1.4-3.8
	$T2835_{O}$-$H2837_{ND1}$	1.89-2.16	19.9-22.3		
I10-I11	$E2849_{OE1}$-$I2923_{N}$*	1.89-1.95	22.3-22.9	P2848-Y2948	8.1-9.3
	$T2850_{OG1}$-$S2952_{N}$*	2.01-2.14	21.7-25		
	$K2851_{NZ}$-$E2949_{O}$*	2.03-2.31	12.25-19.15		
I10	$T2850_{N}$-$T2897_{O}$	1.73-1.76	25		
	$T2850_{OG1}$-$E2849_{O}$*	1.66-1.69	20.3-21.1		

*Hydrogen bond is absent in protein copy B of P1 crystal form, due to extensive crystal contacts, distorting domain arrangement.

I9-I10 and I10-I11 interfaces differ in their interaction areas and hydrogen-bonding pattern but retain the same hydrophobic and electrostatic interaction blueprints. Speculatively, corresponding hydrophobic interactions between the *i* residue of the A'B turn and the aromatic or aliphatic portion of a sidechain in the corresponding BC loop position (**Figure 4.13AB**) might be common for the constitutively expressed regions of titin's I-band. In alternatively spliced region of titin's I-band glycine is found in the vast majority of the domains (see **Appendix 3** for the alignment) and the inter-residue distance is outside the hydrophobic interaction range (**Figure 4.13C**).

Figure 4.13 Conserved hydrophobic in constitutively expressed region of titin's I-band. **A**. Conserved pattern of domain linking hydrophobic interactions. *i* residue (red) in A'B turn interacts with aromatic residue (green) in BC loop of proceeding domain. **B**. Structural alignment of known titin's I-band Ig domains with indicated possible interacting residues. Note that glycine is found in corresponding BC loop position in alternatively spliced titin's I band Ig tandems. [*,†,‡] alignment based on I9-I11^{WT}, PDB ID 1G1C, 3B43, respectively; otherwise on primary sequence. **C**. Summary of predicted interaction pairs. Residues are numbered according the PDB coordinate files. Hydrophobic interactions predicted using YASARA software. In parentheses relative strength (arbitrary units) of interaction is given.

A

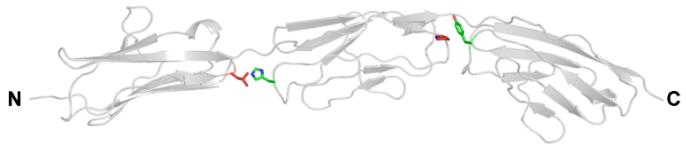

B

C

	Interacting residues	Hydrophobic interaction	Distance (Å)
I9-I10	L16-H116	Yes (3.803)	6.26
I10-I11	P103-Y203	Yes (8.261)	4.08
I65-I66	A14-G123	None	14.58
I66-I67	T110-G219	None	16.37
I67-I68	A206-G313	None	12.61
I68-I69	K300-G406	None	10.73
I69-I70	L393-G499	None	12.37

Electrostatic potential maps of single domains in I9-I11 tandem revealed a conserved pattern: negative C-terminal regions of the preceding Ig domain interact with the positively charged N-terminus of following domain. In the middle of the negative cluster a conserved glutamate resides located at the position *i+1* in the A'B β-hairpin (**Figure 4.14**). Such electrostatic patterns of domain stabilization might be universal for the constitutively expressed Ig tandems in I-band of titin, as high conservation of the described glutamate implies (see **Appendix 3** for the alignment) Thus, taken together interdomain arrangement in I9-I11 is mediated through hydrophobic and electrostatic interactions that might be representative for the constitutively expressed regions of titin's I-band in general.

Figure 4.14 Electrostatic interdomain interactions in I9-I11. Electrostatic potential *in vacuuo* was calculated using the particle mesh Ewald approach in AMBER03 force field with YASARA for single Ig domains. The range and colour coding of the potential is +200.0 kJ/mol (blue) to -200 kJ/mol (red). Potential mapped to I9-I11structure is presented above and negative clusters of individual domains are shown below. Arrows indicate position of conserved glutamate in *i+1* position in A'B β-hairpin.

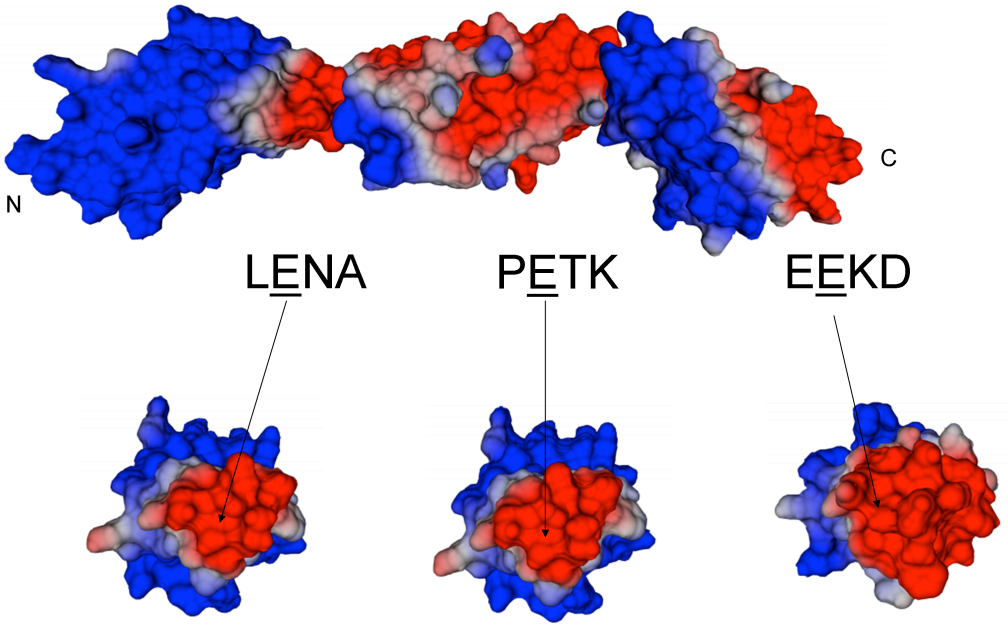

Exchange to the larger hydrophobic sidechain of isoleucine was predicted to have strong destabilizing effect (ΔΔG = 6.45 kcal/mol as calculated with FoldX (Van Durme et al., 2011)) within the I9-I11 context. This effect could be attributed to the

loss of hydrogen bond between the side-chain hydroxyl of T2850 and backbone amide of S2952. Taken together I9-I11 structure implies that T2850I exchange would not be tolerated and might perturb interdomain organization.

4.3.5 NMR studies of I10

Attempts to crystallize the T2850I mutant version of I10 or I9-I11 failed, therefore the mutational effect was characterized using NMR on I10. HSQC spectra of both wild-type and mutant I10 domain show sharp, well-dispersed peaks characteristic of folded proteins (**Figure 4.15**). However, a fraction of amide resonances was perturbed by the T2850I mutation. Chemical shift perturbations were quantified using a weighted average chemical shift difference (Nordstrand et al., 2000) and regarded as large ($0.03 < \Delta\delta_{AV} < 0.15$ ppm) or extensive ($\Delta\delta_{AV} > 0.15$ ppm). In the 91 residue-long I10 construct, 4 residues underwent extensive, and 21 residues large chemical shift perturbations. When mapped on the crystal structure of I10, the affected residues clustered around the mutation site primarily in the A'B and EF loop regions (**Figure 4.16A**). The perturbed residues furthest from the mutation site localized in the CD loop. It is noteworthy that the backbone amide in mutation site underwent a comparably small perturbation of only 0.06 ppm.

In order to address the effect of the mutation on protein dynamics, the S^2 model-free order parameter was calculated **(Figure 4.16B**). This parameter is a measure of local rigidity, where a rigid residue would acquire a value of 1 and a flexible residue would be 0. Comparison of wild-type and mutant I10 dynamics in terms of S^2 indicated that the mutant exhibits increased mobility, particularly in the loop regions. Regions of increased local mobility match well the clusters of residues with the largest chemical shift perturbations. The crystal structure of I10 allowed the interpretation of the observed mutational effects through mapping. Chemical shift perturbations and increased local flexibility cluster in the BC and FC loops that are interconnected through hydrogen bonds mediated by T2850 (as described in **Section 4.3.4**). Thus, loss of these hydrogen bonds could be in part responsible for the structural perturbations. To test this hypothesis, *15*N-labeled I10 protein was flash frozen in liquid nitrogen, lyophilized, re-dissolved in D_2O and its *1*H-*15*N HSQC

spectrum recorded (**Figure 4.17A**). This experiment allowed identification of slow exchanging amide protons in a hydrogen-bonded state or burial inside the hydrophobic core. I10 and $I10^{T2850I}$ have nearly identical hydrogen bonding patterns (**Figure 4.17B**). However, the amide of mutant $I10^{T2850I}$ was no longer hydrogen-bonded as opposed to wild-type T2850 (T20). In consequence, a former donor of hydrogen bond T2897 (T67) experience extensive chemical shift perturbation of 0.47 ppm. In a similar fashion an extensive chemical shift of E2849 (E19) could be a result of a lost hydrogen bond between the main-chain carboxyl group and hydroxyl group of T2850 (T20) side-chain. Taken together chemical shift perturbations and clusters of increased local mobility caused by T2850I mutation gather around the mutation site at the "C-terminal" loop cluster of this Ig domain caused by the altered hydrogen bond network.

Figure 4.15 HSQC spectra overlay of assigned wild-type (red) and mutant (black) I10 domains. Most significant chemical shift perturbations are indicated. Residue label font size corresponds to the relative magnitude of chemical shift differences.

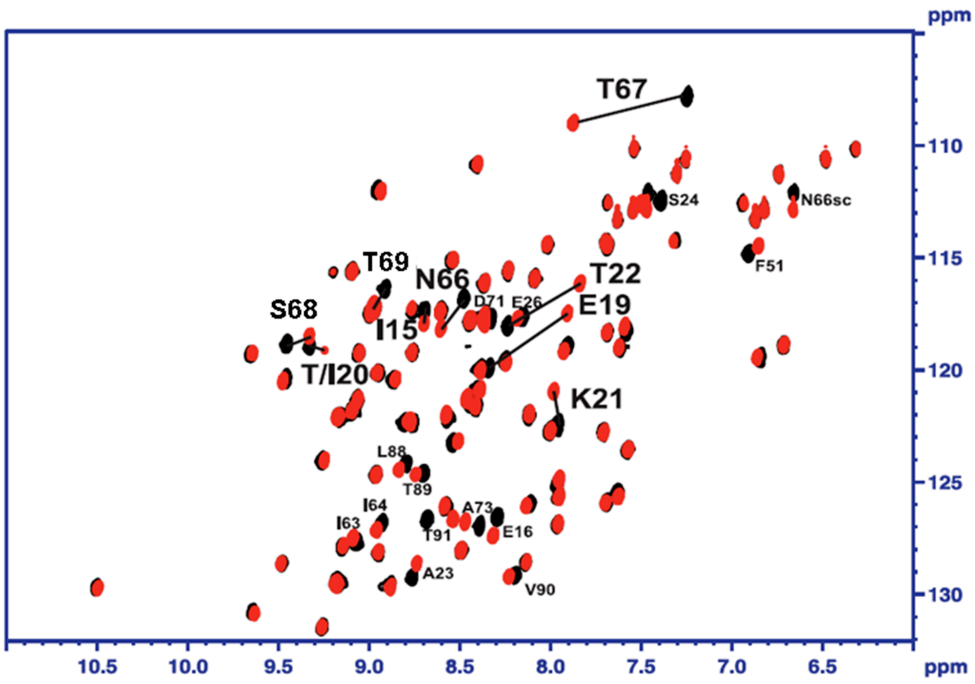

Figure 4.16 NMR study of mutational effects. **A**. Weighted backbone amide chemical shift differences between wild-type and mutant I10 mapped on structure of I10WT. Large (0.03<ΔδAV<0.15 ppm) and extensive (ΔδAV>0.15 ppm) chemical shift perturbations are represented as orange and red spheres. Position of mutated residue is marked with white asterix. **B**. S^2 model free parameter for wild-type (blue) and mutant (red) I10. Note increased flexibility of mutant loop residues. Arrow indicates mutation site. Cartoon above the chart illustrates secondary structure elements of I10 domain.

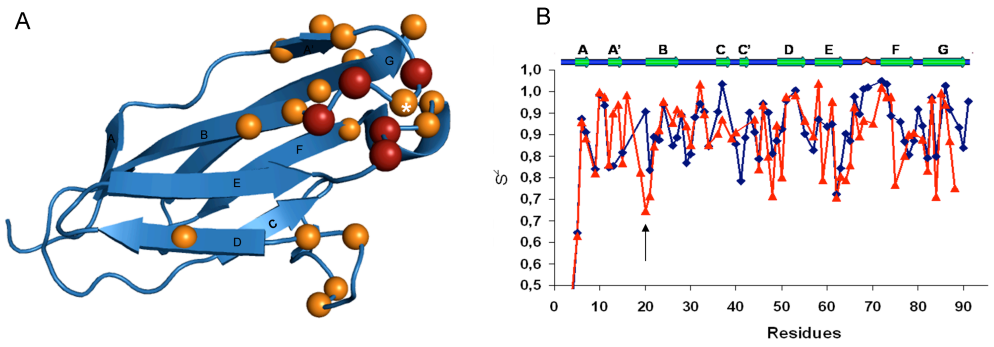

Figure 4.17 Mutational effects on hydrogen bonding A. Overlay of HSQC spectra before (green) and after (red) exchange to D_20. Note protection from H/D exchange of wild-type T20, but not mutant I20 amide (arrow). **B**. Hydrogen-bonded amide protons in wild-type and mutant I10 observed by slow H > D exchange. Arrow indicates lost hydrogen bond upon T2850I mutation. Secondary structure elements are presented according the crystal I10 structure. To ease labelling in the HSQC spectra, protein residues are numerated with respect to the beginning of the I10 sequence as described in this study, so that T2850 is T20.

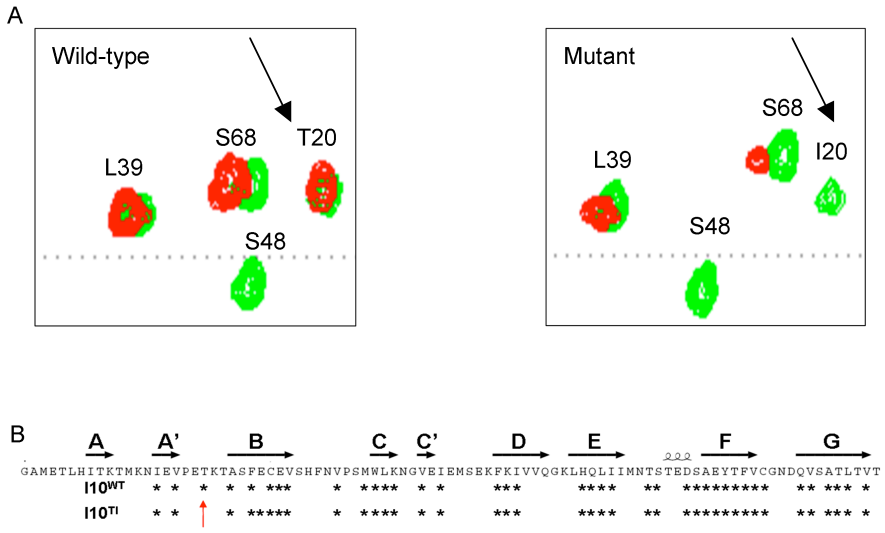

In order to reveal how observed mutational effects affect the organization of the I10 domain solution structures were calculated (**Figure 4.18A**). In the NMR ensemble, β-sheet C' was distorted and not represented. Representative structures (calculated with NMRclust (Kelley et al., 1997) of wild-type and mutant I10 superimpose very well, giving RMSD = 1.55 Å (just marginally above the intra-ensemble variation) (**Figure 4.18B**), indicating that the mutation does not affect the overall fold of I10. It is noteworthy that the mutated A'B loop retains the wildtype structure, whereas the mutant isoleucine follows the side chain of the native threonine (**Figure 4.18C**, sidechain residues).

Figure 4.18 NMR solution structure of wild-type and mutant I10.
A. Superimposition of WT (blue) and mutant (red) solution structure ensembles. T2850/I2850 are represented as sticks. **B**. NMR and refinement statistics for protein structures. **C**. Superimposition of representative (calculated with NMRclust) wild-type (blue) and mutant (red) NMR structures**.**

A

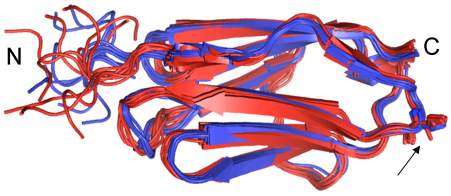

C

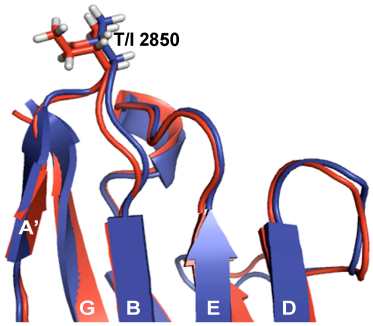

B

	$I10^{WT}$	$I10^{T2850I}$
NMR distance and dihedral constraints		
Distance constraints		
Total NOE	1603	1515
NOE completness	52.6%	46.3%
Long-range ($\|i-j\|>5$)	632	487
Hydrogen bonds	30	33
Total dihedral angle restraints (TALOS +)		
φ	70	71
ψ	70	71
Structure statistics		
Violations (mean ± s.d.)		
Distance constraints (Å)	0.071±0.004	0.036±0.002
Dihedral angle constraints (°)	0.45±0.07	0.89±0.14
Max. dihedral angle violation (°)	3.6	7.8
Max. distance constraint violation (Å)	0.27	0.32
Deviations from idealized geometry		
Bond lengths (Å)	0.00382±0.00004	0.00415±0.00011
Bond angles (°)	0.44±0.01	0.54±0.02
Impropers (°)	1.48±0.10	1.80±0.11
Mean pairwise RMSD. deviation* (Å)		
Backbone	0.51 ± 0.11	0.68 ± 0.06
Heavy	1.15 ± 0.09	1.32 ± 0.08

* Pairwise RMSD was calculated for residues 6-91 between 10 refined structures.

Taken together, NMR analysis of WT and mutant I10 revealed that the pathogenic T2850I mutation does not largely alter the fold, but affects protein dynamics by increasing loop flexibility.

4.3.6 Effects of T2850I on protein stability and localization in vivo

To test whether the T2850I mutation led to a differential functionality *in vivo*, we assayed fragments of the titin chain in skeletal muscle. For this work, GFP-tagged titin fragments were introduced into skeletal muscle of live mice. The work here described was carried out in collaboration with Muzamil Majid Khan at University of Applied Sciences Mannheim.

GFP tagged wild-type and mutant I7-I13 Ig-tandem fragments were introduced into *tibialis anterior* muscle of living mice via electroporation. In order to minimize possible tag-caused interference extended titin fragments were chosen in this experimental setup. The cellular fate of titin fragments in transfected muscle extracts was followed by Western Blot, using anti-GFP antibody. Single sharp protein bands corresponding to the expected molecular weight of the constructs were detected by blotting (**Figure 4.19** left panel). No visible signs of degradation were observed for either the wild-type or mutant I7-I13. In summary, although the T2850I exchange has a destabilizing effect on the isolated I10 domain *in vitro*, the latter does not result in increased degradation of mutant titin fragments expressed in muscle of live mice.

Imaging of transfected muscles revealed a differential myocellular localization of the wild-type and mutant I7-I13 protein (**Figure 4.19** middle and right panels) WT fragments remained mostly soluble inside the cytoplasm, with only weak signs of striated pattern. However, the mutant I7-I13 acquired a striated pattern. In order to better characterize the observed staining patterns, fixed transgenic muscle sections were co-stained with fluorescent phalloidin conjugate. Phalloidin binds to thin filament-forming F-actin. Double labelling revealed that the wild-type construct concentrates in areas lacking F-actin (i.e. A-band), whereas the mutant fragment colocalized with phalloidin conjugate stained thin filament. Colocalization with F-actin in “double-band” striation pattern of mutant fragment in skeletal muscle resembles alignment laterally to the Z-disks. Such pattern would be expected for the native I10 position however other structures such as terminal cisternae of the sarcoplasmic reticulum would result in indistingusible staining pattern (Nori et al., 2006). The latter is of particular interest, as tsO45 mutant vesicular stomatitis virus

accumulates in the same pattern (Rahkila et al., 1996) when temperature is increased to induce its misfolding (Hammond and Helenius, 1994) and causes ER stress response. In similar fashion, the striated pattern of mutant I7-I13 myocellular localization could be the result of association with the structures of endoplasmic/sarcoplasic reticulum, caused by mutation-induced propensity to misfold. In order to test this hypothesis further studies are needed. As a primary experiment, differences in cellular response to the mutant and wild-type protein have to be compared. In summary, in vivo localization studies revealed that T2850I mutation alters myocellular localization but not the stability of I7-I13 titin fragments and further studies are needed to elucidate the cause of the observed differences.

Figure 4.19 In vivo studies of I7-I11 fragments. Panel Left. Stability of I7-I11 fragments *in vivo*. Western blot with anti-GFP antibody (left) and corresponding Coomassie stained gel of transgenic *T. anterior* muscles. Both, WT and mutated I7-I13 were stably expressed for two weeks in vivo, and Western blots indicated no proteolytic degradation. **Middle panel**. Differential localization of wild-type and mutant I7-I13 titin fragments in muscle. WT I7-I13 GFP fusion proteins remained mostly diffuse in the cytoplasm, whereas T2850I mutated I7-I13 fragments targeted to the myofibril. **Right panel**. Double labelling with phalloidin revealed that mutated I7-I13 fragments in myofibrils co-localise with phalloidin, while mutant I7-I13 matches the tkick filament region.

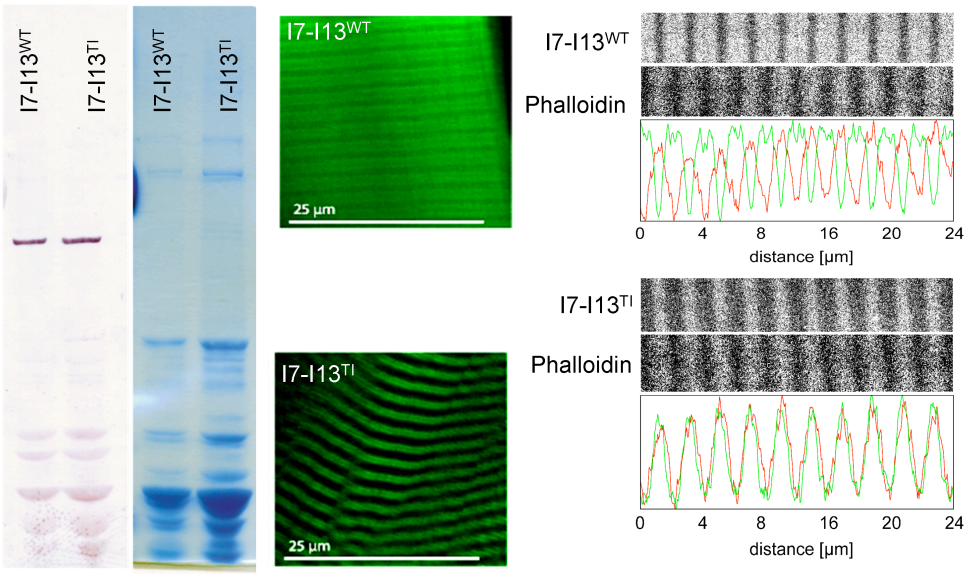

4.3.7 I7-I13 titin fragments affects cardiomyocyte contractility

Since the *in vivo* localisation studies detected a colocalization of T2850I mutated titin fragments with thin filaments, it was speculated that mutated titin fragments might alter the biomechanical properties of cardiomyocytes by interference with the force-bearing cross-bridges. To test this hypothesis, maximal tension and calcium sensitivity of skinned human cardiomyocytes was determined before and after addition of recombinant titin fragments to the assay solution. The biomechanical measurements were performed by Emmy Manders at VU University Medical Center, the Netherlands.

I7-I13 fragments had an effect on cardiomyocyte biomechanical properties. After addition of recombinant protein maximal active tension was reduced and calcium sensitivity increased (**Figure 4.20**). T2850I mutated titin fragment caused a 10% reduction of maximal tension. WT fragments demonstrated the same characteristics but due to higher variance and outliers the results did not reach statistical significance. Increased calcium sensitivity after titin fragment addition was noted for both WT and mutant fragments, but more pronounced after the addition of mutant fragment (**Figure 4.20B**).

Figure 4.20 Effect of recombinant I7-I13 fragments on the biomechanical properties of the cardiomyocytes. Human left ventricle cardiomyocytes were characterized biomechanically for active force and calcium sensitivity of force. Same measurements were repeated after incubation with recombinant titin fragments. A. Addition of mutant I7-I13 significantly decreased maximal active tension, whereas effect of WT protein did not reach statistical significance. Note higher data variation and presence of outlier in wild-type experiment. B Slight but significant increase of calcium sensitivity was seen for both WT and T105I fragments.

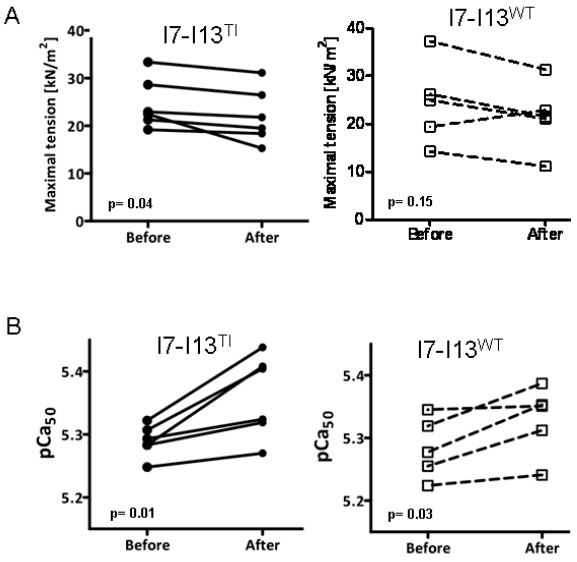

Obtained data does not exclude the posibility that the T2850I mutation might alter biomechanical cardiomyocyte properties. However additional experiments are required to understand/validate this phenomenon. Firstly, only 5-6 myocytes were used per experimental group making this dataset extremely sensitive to outliers. Therefore in order to gain solid statistical conclusion experiments should be repeated with higher biological replicate numbers. Secondly, buffers used for the pretreatment measurements and one with studied proteins originate from different batches so this experiment was not controlled for the buffer effects. Thus subtle changes in buffer compostion could have caused observed changes of biomechanical parameters. Finally, in order to link biomechanical alterations to pathogenesis of T2850I associated ARVC proper localization of recombinant titin fragments in skinned myofiber lattice should be confirmed.

Taken together, although these experiments lacking critical biological and technical controls preliminary data does not contradict the hypothesis that T2850I mutation might have an effect on the biomechanical myofibril properties.

4.4 Discussion

Performed work provides structural and physiological insights into T2850I mutation within the I10 domain alone and in context of neighbouring domains I9-I11. Obtained results demonstrated that the affected threonine residue adopts a high energy conformation, stabilized by two hydrogen bonds that are lost upon mutation, leading to the significant destabilization of the domain. In the context of the titin chain, the affected threonine was found to mediate Ig-Ig interactions. However, the weakening of mutant I10 observed *in vitro* did not translate into an increased titin chain fragment propensity for degradation *in vivo*, but rather caused differential myocellular targeting.

Obtained results are in contrast to previous structural studies on T2850I mutation (Taylor et al., 2011; Anderson et al., 2013) claiming domain destabilization as a major pathogenetic effect. In this work mutation caused a significant drop in melting temperature, indicative for domain destabilization, but was compatible with the Ig fold as revealed by NMR analysis. This observation is coherent with the reported outstanding mutational robustness of the titin Ig domain (Bruning, et al 2012). The overestimation of destabilizing effects could have been caused by suboptimal construct design used in previous studies on T2850I mutation. Sequence analysis revealed that the I10 construct was missing the A strand, which impaired intrinsic domain stability. Thus taken together, obtained results indicate that domain unfolding is unlikely factor in T2850I caused ARVC.

I10 structures revealed that the sidechain of the affected threonine is directed outwards the Ig domain, suggesting that T2850I might have an effect on interdomain interactions. In order to test this hypothesis the crystal structure of I10 surrounded by the neighbouring I9 and I10 domains was solved. The crystal structure revealed that the affected threonine is located in the middle of an extensive 5-hydrogen bond stabilized interface between I10 and I11. Conserved hydrophobic interdomain

interaction was observed in I9-I11 structure. Speculatively, T2850I exchange in the confined I10-I11 interface would disturb both polar and non-polar interactions. Thus, the disruption of the Ig-Ig interface might result in exposure of an interdomain hydrophobic patch. Taken together structural analysis suggested that the T2850I exchange effect might be composite and involve both local destabilization of I10 domain itself and exposure hydrophobic patch at the I10-I11 interface.

In order to gain insights into how proposed alterations might translate into physiological phenomena, the cellular fate of titin fragments was followed in skeletal muscle and the effect of recombinant protein on biomechanical properties of skinned human cardiac myocytes was measured. GFP-tagged wild-type and mutant I7-I13 fragments introduced into skeletal muscle of live mice show no obvious signs of degradation: using transgenic muscle extracts single band of expected molecular weight was detected using Western blot with anti-GFP antibodies. However, myocellular localization of titin fragments is different. While the vast majority of wild-type protein was diffuse, mutant protein tended to colocalize laterally to the Z-discs. Observed phenomenon could be interpreted in several ways. Firstly, earlier data suggested that the proximal titin Ig tandem segment close to the Z-disk has a propensity to weakly interact with the thin filament (Trombitas et al., 1993, Trombitas and Pollack, 1993, Trombitas et al., 1997). Therefore, T2850 exchange might stabilize this interaction by exposing a hydrophobic patch along the titin filament, conferring a non-physiological stickiness of titin to the thin filament. Thus, an increase in affinity would be sufficient to overcome the entropic barrier and allow mutant titin fragment to target expected localization, whereas physiological affinity of wild-type would not be sufficient for the proper localization within the myofibril in the described experimental setup. In similar fashion, pathologically increased affinity of filamin C to F-actin was shown to cause distal myopathy (Duff et al., 2011). Consequently, more stable titin- thin filament interaction would affect myofibrillar biomechanics and perhaps indirectly the Frank-Starling mechanism. Preliminary results do not contradict the hypothesis that recombinant I7-I13 fragments might have an effect on biomechanical properties. It should be noted that in *in vitro* single myofibril experiment, a molar excess of mutant titin fragments was added in solution. *In vivo* in ARVC affected hearts, only a single titin hydrophobic patch will be present that is unlikely to inhibit numerous actomyosin crossbridges. Therefore, future studies will

need to test the effect of introducing the T2850I allele into transgenic mice, and if this leads to more stable titin – thin filament associations within the periphery of the Z-disk, possibly in turn connected to a pathological activation of strain-sensing pathways at resting sarcomere lengths. On the other hand, observed mutant localization might be caused by the association with the structures of the sarcoplasmic reticulum. A Z-disc-like localization pattern does not necessary indicate association with the myofibril itself, because most of the cellular compartments and organelles in myocytes align into well-defined striations. Observed mutant I7-I13 localization pattern is identical to one observed for the folding defective viral probes (Kaisto and Metsikko, 2003, Rahkila et al., 1996), accumulating in terminal cisternae. In context of structural insights, this allows us to hypothesise that T2850I mutation in a cellular context might result in entrapment and accumulation of misfolded, degradation-resistant mutant titin fragments in the sarcoplasmic reticulum. However, studied GFP-tagged titin fragments do not have obvious signal peptides for ER targeting, but it was demonstrated that removal of misfolded cytosolic proteins require association with the endoplasmic reticulum (Metzger et al., 2008). In line with this hypothesis T2850I mutation would cause shortage of mutant titin molecules and a permanent endoplasmic reticulum stress response. The following could lead to heart disease as it was shown that titin transcript levels are reduced in dilated cardiomyophaty affected human hearts (Ahmad et al., 2010) and accumulation of misfolded proteins in the ER in transgenic mouse model causes dilated cardiomyopathy (Hamada et al., 2004). Thus, according this hypothesis the molecular pathomechanism of T2850I associated cardiomyopathy would resemble the one of ΔF508 caused cystic fibrosis, where mutant protein is partially retained in the endoplasmic reticulum (Kopito, 1999) resulting in deficiency of protein in the plasma membrane.

Taken together structural analysis provided a solid basis for the future elucidation of T2850I caused cardiomyopathy. Based on obtained data two novel molecular scenarios are proposed as how to T2850I exchange might lead to heart disease. According the first scenario, mutation might increase titin stickiness to the thin filament, inhibiting numerous actomyosin crossbridges and inducing pathological activation of strain-sensing pathways at resting sarcomere lengths. Attenuation of such strain-sensing pathways would then be a rational therapeutic to combat the severe ARVC pathology present in the T2850I carrying families. According to the

second scenario, misfolded mutant protein accumulates in the sarcoplasmic reticulum, resulting in shortage of functional titin filaments and permanent ER stress. Speculatively, T2850I mutation carrying patients could benefit from stimulation of folding-machinery to counteract shortage of functional titin molecules or activation of autophagy in order to “clean up” the “clogged” non-functional ER.

6 General discussion

In this work, a structure-driven approach was taken to gain insights into the function of the titin filament with emphasis on TK. In contrast to the scientific consensus, this work demonstrated that TK is a catalytically inactive molecular scaffold physically interconnected with the ubiquitin ligase MuRF1 signalling axis. Mutational perturbation of this link was found to be associated with DCM. A similar pattern of mutation-induced weakening of interdomain interactions was proposed as a pathogenetic trigger causing ARVC.

Discrimination between rare benign genetic variations and pathogenic mutations is a complex task (Mestroni and Taylor et al., 2013), due to the unexpectedly large number of rare genetic variants in the human genome (Nelson et al., 2012, Keinan and Clark 2012). In this work, supportive validation of pathogenic titin mutations was attained by the structural analysis of mutation-affected titin structures. Although the structures of mutants were not obtained in most cases, analysis of wildtypes allowed us to deduce mutational effects and directed subsequent functional studies. Biological effects caused by the D24728V mutation were studied in cell culture. Chosen experimental setup has limited potential as organ- and organ system- level phenomena (for example, pressure, contractility) cannot be produced but might act as major factors in disease ethiology. Effects of T2850I were studied in live animals but in skeletal instead of cardiac muscle, due to technical advantage. Thus, ectopic protein expression in a skeletal muscle is not sufficient to recreate the environment of heart and important factors might be missing in a given setup. Using *in vivo* approach differential responses to the mutant proteins were detected, however how the observed differences translate into the disease phenotype remains an open question(s) for the further studies. Taken together, this novel approach might help to increase confidence in discrimination of novel pathogenic titin mutations from benign genetic variations.

The structural effects of two cardiomyopathy-associated titin mutations studied in this work revealed shared conceptual similarities. Mutations presented in this work are different in the nature of amino acid substitution, localization in the sarcomere and protein folds affected. However, interactions between the domains were impaired in both cases. It is known that alteration of protein-protein binding affinities might lead to disease. However, the detrimental effect of altered interdomain interactions is a novel observation. The results presented underscore the importance of studying titin within the context of neighbouring domains, as this approach would allow a more complete insight into the pathogenic effects of mutations.

7 References

Ackermann, M. A. & Kontrogianni-Konstantopoulos, A. 2013. *Cardiomyopathies: When the Goliaths of Heart Muscle Hurt*.

Adams, P. D., Afonine, P. V., Bunkoczi, G., Chen, V. B., Echols, N., Headd, J. J., Hung, L. W., Jain, S., Kapral, G. J., Grosse Kunstleve, R. W., Mccoy, A. J., Moriarty, N. W., Oeffner, R. D., Read, R. J., Richardson, D. C., Richardson, J. S., Terwilliger, T. C. & Zwart, P. H. 2011. The Phenix software for automated determination of macromolecular structures. *Methods,* 55**,** 94-106.

Adzhubei, I., Jordan, D. M. & Sunyaev, S. R. 2013. Predicting functional effect of human missense mutations using PolyPhen-2. *Curr Protoc Hum Genet,* Chapter 7**,** Unit7 20.

Ahmad, S., Rai, T. S., Khullar, M., Bahl, A., Saikia, U. N., Thungapathra, M., Kumar, R. M., Mahajan, R. & Talwar, K. K. 2010. Decreased myocardial expression of dystrophin and titin mRNA and protein in dilated cardiomyopathy: possibly an adverse effect of TNF-alpha. *J Clin Immunol,* 30**,** 520-30.

Anderson, B. R., Bogomolovas, J., Labeit, S. & Granzier, H. 2013. Single Molecule Force Spectroscopy on Titin Implicates Ig Domain Stability as a Cardiac Disease Mechanism. *J Biol Chem*.

Arimura, T., Bos, J. M., Sato, A., Kubo, T., Okamoto, H., Nishi, H., Harada, H., Koga, Y., Moulik, M., Doi, Y. L., Towbin, J. A., Ackerman, M. J. & Kimura, A. 2009. Cardiac ankyrin repeat protein gene (ANKRD1) mutations in hypertrophic cardiomyopathy. *J Am Coll Cardiol,* 54**,** 334-42.

Arya, R., Kedar, V., Hwang, J. R., Mcdonough, H., Li, H. H., Taylor, J. & Patterson, C. 2004. Muscle ring finger protein-1 inhibits PKC{epsilon} activation and prevents cardiomyocyte hypertrophy. *J Cell Biol,* 167**,** 1147-59.

Atkinson, R. A., Joseph, C., Kelly, G., Muskett, F. W., Frenkiel, T. A., Nietlispach, D. & Pastore, A. 2001. Ca2+-independent binding of an EF-hand domain to a novel motif in the alpha-actinin-titin complex. *Nat Struct Biol,* 8**,** 853-7.

Bandaranayake, R. M., Ungureanu, D., Shan, Y., Shaw, D. E., Silvennoinen, O. & Hubbard, S. R. 2012. Crystal structures of the JAK2 pseudokinase domain and the pathogenic mutant V617F. *Nat Struct Mol Biol,* 19**,** 754-9.

Bang, M. L., Centner, T., Fornoff, F., Geach, A. J., Gotthardt, M., Mcnabb, M., Witt, C. C., Labeit, D., Gregorio, C. C., Granzier, H. & Labeit, S. 2001. The complete gene sequence of titin, expression of an unusual approximately 700-kDa titin isoform, and its interaction with obscurin identify a novel Z-line to I-band linking system. *Circ Res,* 89**,** 1065-72.

Bardiaux, B., Bernard, A., Rieping, W., Habeck, M., Malliavin, T. E. & Nilges, M. 2008. Graphical analysis of NMR structural quality and interactive contact map of NOE assignments in ARIA. *BMC Struct Biol,* 8**,** 30.

Battye, T. G., Kontogiannis, L., Johnson, O., Powell, H. R. & Leslie, A. G. 2011. iMOSFLM: a new graphical interface for diffraction-image processing with MOSFLM. *Acta Crystallogr D Biol Crystallogr,* 67**,** 271-81.

Bick, A. G., Flannick, J., Ito, K., Cheng, S., Vasan, R. S., Parfenov, M. G., Herman, D. S., Depalma, S. R., Gupta, N., Gabriel, S. B., Funke, B. H., Rehm, H. L., Benjamin, E. J., Aragam, J., Taylor, H. A., Jr., Fox, E. R., Newton-Cheh, C., Kathiresan, S., O'donnell, C. J., Wilson, J. G., Altshuler, D. M., Hirschhorn, J. N., Seidman, J. G. & Seidman, C. 2012. Burden of rare sarcomere gene

variants in the Framingham and Jackson Heart Study cohorts. *Am J Hum Genet,* 91**,** 513-9.

Bodine, S. C., Latres, E., Baumhueter, S., Lai, V. K., Nunez, L., Clarke, B. A., Poueymirou, W. T., Panaro, F. J., Na, E., Dharmarajan, K., Pan, Z. Q., Valenzuela, D. M., Dechiara, T. M., Stitt, T. N., Yancopoulos, G. D. & Glass, D. J. 2001. Identification of ubiquitin ligases required for skeletal muscle atrophy. *Science,* 294**,** 1704-8.

Bogomolovas, J., Simon, B., Sattler, M. & Stier, G. 2009. Screening of fusion partners for high yield expression and purification of bioactive viscotoxins. *Protein Expr Purif,* 64**,** 16-23.

Boudeau, J., Miranda-Saavedra, D., Barton, G. J. & Alessi, D. R. 2006. Emerging roles of pseudokinases. *Trends Cell Biol,* 16**,** 443-52.

Brenner, B. & Eisenberg, E. 1986. Rate of force generation in muscle: correlation with actomyosin ATPase activity in solution. *Proc Natl Acad Sci U S A,* 83**,** 3542-6.

Brown, E. J., Beal, P. A., Keith, C. T., Chen, J., Shin, T. B. & Schreiber, S. L. 1995. Control of p70 s6 kinase by kinase activity of FRAP in vivo. *Nature,* 377**,** 441-6.

Bruning, M., Barsukov, I., Franke, B., Barbieri, S., Volk, M., Leopoldseder, S., Ucurum, Z. & Mayans, O. 2012. The intracellular Ig fold: a robust protein scaffold for the engineering of molecular recognition. *Protein Eng Des Sel,* 25**,** 205-12.

Bucher, R. M., Svergun, D. I., Muhle-Goll, C. & Mayans, O. 2010. The structure of the FnIII Tandem A77-A78 points to a periodically conserved architecture in the myosin-binding region of titin. *J Mol Biol,* 401**,** 843-53.

Carmignac, V., Salih, M. A., Quijano-Roy, S., Marchand, S., Al Rayess, M. M., Mukhtar, M. M., Urtizberea, J. A., Labeit, S., Guicheney, P., Leturcq, F., Gautel, M., Fardeau, M., Campbell, K. P., Richard, I., Estournet, B. & Ferreiro, A. 2007. C-terminal titin deletions cause a novel early-onset myopathy with fatal cardiomyopathy. *Ann Neurol,* 61**,** 340-51.

Centner, T., Yano, J., Kimura, E., Mcelhinny, A. S., Pelin, K., Witt, C. C., Bang, M. L., Trombitas, K., Granzier, H., Gregorio, C. C., Sorimachi, H. & Labeit, S. 2001. Identification of muscle specific ring finger proteins as potential regulators of the titin kinase domain. *J Mol Biol,* 306**,** 717-26.

Chang, X. & Wang, K. 2012. wANNOVAR: annotating genetic variants for personal genomes via the web. *J Med Genet,* 49**,** 433-6.

Chen, S. N., Czernuszewicz, G., Tan, Y., Lombardi, R., Jin, J., Willerson, J. T. & Marian, A. J. 2012. Human molecular genetic and functional studies identify TRIM63, encoding Muscle RING Finger Protein 1, as a novel gene for human hypertrophic cardiomyopathy. *Circ Res,* 111**,** 907-19.

Chen, Y. W., Dodson, E. J. & Kleywegt, G. J. 2000. Does NMR mean "not for molecular replacement"? Using NMR-based search models to solve protein crystal structures. *Structure,* 8**,** R213-20.

Choi, Y., Sims, G. E., Murphy, S., Miller, J. R. & Chan, A. P. 2012. Predicting the functional effect of amino acid substitutions and indels. *PLoS One,* 7**,** e46688.

Clarke, B. A., Drujan, D., Willis, M. S., Murphy, L. O., Corpina, R. A., Burova, E., Rakhilin, S. V., Stitt, T. N., Patterson, C., Latres, E. & Glass, D. J. 2007. The E3 Ligase MuRF1 degrades myosin heavy chain protein in dexamethasone-treated skeletal muscle. *Cell Metab,* 6**,** 376-85.

Depristo, M. A., Banks, E., Poplin, R., Garimella, K. V., Maguire, J. R., Hartl, C., Philippakis, A. A., Del Angel, G., Rivas, M. A., Hanna, M., Mckenna, A., Fennell, T. J., Kernytsky, A. M., Sivachenko, A. Y., Cibulskis, K., Gabriel, S. B., Altshuler, D. & Daly, M. J. 2011. A framework for variation discovery and genotyping using next-generation DNA sequencing data. *Nat Genet,* 43**,** 491-8.

Dona, M., Sandri, M., Rossini, K., Dell'aica, I., Podhorska-Okolow, M. & Carraro, U. 2003. Functional in vivo gene transfer into the myofibers of adult skeletal muscle. *Biochem Biophys Res Commun,* 312**,** 1132-8.

Dosset, P., Hus, J. C., Blackledge, M. & Marion, D. 2000. Efficient analysis of macromolecular rotational diffusion from heteronuclear relaxation data. *J Biomol NMR,* 16**,** 23-8.

Duff, R. M., Tay, V., Hackman, P., Ravenscroft, G., Mclean, C., Kennedy, P., Steinbach, A., Schoffler, W., Van Der Ven, P. F., Furst, D. O., Song, J., Djinovic-Carugo, K., Penttila, S., Raheem, O., Reardon, K., Malandrini, A., Gambelli, S., Villanova, M., Nowak, K. J., Williams, D. R., Landers, J. E., Brown, R. H., Jr., Udd, B. & Laing, N. G. 2011. Mutations in the N-terminal actin-binding domain of filamin C cause a distal myopathy. *Am J Hum Genet,* 88**,** 729-40.

Durand, D., Vives, C., Cannella, D., Perez, J., Pebay-Peyroula, E., Vachette, P. & Fieschi, F. 2010. NADPH oxidase activator p67(phox) behaves in solution as a multidomain protein with semi-flexible linkers. *J Struct Biol,* 169**,** 45-53.

Eilertsen, K. J., Kazmierski, S. T. & Keller, T. C., 3rd 1997. Interaction of alpha-actinin with cellular titin. *Eur J Cell Biol,* 74**,** 361-4.

Emsley, P., Lohkamp, B., Scott, W. G. & Cowtan, K. 2010. Features and development of Coot. *Acta Crystallogr D Biol Crystallogr,* 66**,** 486-501.

Endicott, J. A., Noble, M. E. & Johnson, L. N. 2012. The structural basis for control of eukaryotic protein kinases. *Annu Rev Biochem,* 81**,** 587-613.

Evans, P. 2006. Scaling and assessment of data quality. *Acta Crystallogr D Biol Crystallogr,* 62**,** 72-82.

Fabiato, A. & Fabiato, F. 1978. Effects of pH on the myofilaments and the sarcoplasmic reticulum of skinned cells from cardiace and skeletal muscles. *J Physiol,* 276**,** 233-55.

Fischer, H., Neto, M. D., Napolitano, H. B., Polikarpov, I. & Craievich, A. F. 2010. Determination of the molecular weight of proteins in solution from a single small-angle X-ray scattering measurement on a relative scale. *Journal of Applied Crystallography,* 43**,** 101-109.

Franke, D., Kikhney, A. G. & Svergun, D. I. 2012. Automated acquisition and analysis of small angle X-ray scattering data. *Nuclear Instruments & Methods in Physics Research Section a-Accelerators Spectrometers Detectors and Associated Equipment,* 689**,** 52-59.

Freiburg, A. & Gautel, M. 1996. A molecular map of the interactions between titin and myosin-binding protein C. Implications for sarcomeric assembly in familial hypertrophic cardiomyopathy. *Eur J Biochem,* 235**,** 317-23.

Fukuda, K., Knight, J. D., Piszczek, G., Kothary, R. & Qin, J. 2011. Biochemical, proteomic, structural, and thermodynamic characterizations of integrin-linked kinase (ILK): cross-validation of the pseudokinase. *J Biol Chem,* 286**,** 21886-95.

Fukuda, N. & Granzier, H. L. 2005. Titin/connectin-based modulation of the Frank-Starling mechanism of the heart. *J Muscle Res Cell Motil,* 26**,** 319-23.

Fukuzawa, A., Lange, S., Holt, M., Vihola, A., Carmignac, V., Ferreiro, A., Udd, B. & Gautel, M. 2008. Interactions with titin and myomesin target obscurin and obscurin-like 1 to the M-band: implications for hereditary myopathies. *J Cell Sci,* 121**,** 1841-51.

Fulton, A. B. & Isaacs, W. B. 1991. Titin, a huge, elastic sarcomeric protein with a probable role in morphogenesis. *Bioessays,* 13**,** 157-61.

Furst, D. O., Osborn, M., Nave, R. & Weber, K. 1988. The organization of titin filaments in the half-sarcomere revealed by monoclonal antibodies in immunoelectron microscopy: a map of ten nonrepetitive epitopes starting at the Z line extends close to the M line. *J Cell Biol,* 106**,** 1563-72.

Furukawa, T., Ono, Y., Tsuchiya, H., Katayama, Y., Bang, M. L., Labeit, D., Labeit, S., Inagaki, N. & Gregorio, C. C. 2001. Specific interaction of the potassium channel beta-subunit minK with the sarcomeric protein T-cap suggests a T-tubule-myofibril linking system. *J Mol Biol,* 313**,** 775-84.

Gerull, B., Atherton, J., Geupel, A., Sasse-Klaassen, S., Heuser, A., Frenneaux, M., Mcnabb, M., Granzier, H., Labeit, S. & Thierfelder, L. 2006. Identification of a novel frameshift mutation in the giant muscle filament titin in a large Australian family with dilated cardiomyopathy. *J Mol Med (Berl),* 84**,** 478-83.

Gerull, B., Gramlich, M., Atherton, J., Mcnabb, M., Trombitas, K., Sasse-Klaassen, S., Seidman, J. G., Seidman, C., Granzier, H., Labeit, S., Frenneaux, M. & Thierfelder, L. 2002. Mutations of TTN, encoding the giant muscle filament titin, cause familial dilated cardiomyopathy. *Nat Genet,* 30**,** 201-4.

Gloeckner, C. J., Kinkl, N., Schumacher, A., Braun, R. J., O'neill, E., Meitinger, T., Kolch, W., Prokisch, H. & Ueffing, M. 2006. The Parkinson disease causing LRRK2 mutation I2020T is associated with increased kinase activity. *Hum Mol Genet,* 15**,** 223-32.

Goll, C. M., Pastore, A. & Nilges, M. 1998. The three-dimensional structure of a type I module from titin: a prototype of intracellular fibronectin type III domains. *Structure,* 6**,** 1291-302.

Gotthardt, M., Hammer, R. E., Hubner, N., Monti, J., Witt, C. C., Mcnabb, M., Richardson, J. A., Granzier, H., Labeit, S. & Herz, J. 2003. Conditional expression of mutant M-line titins results in cardiomyopathy with altered sarcomere structure. *J Biol Chem,* 278**,** 6059-65.

Granzier, H., Kellermayer, M., Helmes, M. & Trombitas, K. 1997. Titin elasticity and mechanism of passive force development in rat cardiac myocytes probed by thin-filament extraction. *Biophys J,* 73**,** 2043-53.

Granzier, H., Labeit, D., Wu, Y. & Labeit, S. 2002. Titin as a modular spring: emerging mechanisms for elasticity control by titin in cardiac physiology and pathophysiology. *J Muscle Res Cell Motil,* 23**,** 457-71.

Granzier, H. L. & Labeit, S. 2004. The giant protein titin: a major player in myocardial mechanics, signaling, and disease. *Circ Res,* 94**,** 284-95.

Granzier, H. L. & Labeit, S. 2005. Titin and its associated proteins: the third myofilament system of the sarcomere. *Adv Protein Chem,* 71**,** 89-119.

Grater, F., Shen, J., Jiang, H., Gautel, M. & Grubmuller, H. 2005. Mechanically induced titin kinase activation studied by force-probe molecular dynamics simulations. *Biophys J,* 88**,** 790-804.

Gregorio, C. C., Trombitas, K., Centner, T., Kolmerer, B., Stier, G., Kunke, K., Suzuki, K., Obermayr, F., Herrmann, B., Granzier, H., Sorimachi, H. & Labeit, S. 1998. The NH2 terminus of titin spans the Z-disc: its interaction

with a novel 19-kD ligand (T-cap) is required for sarcomeric integrity. *J Cell Biol,* 143**,** 1013-27.
Guo, W., Bharmal, S. J., Esbona, K. & Greaser, M. L. 2010. Titin diversity--alternative splicing gone wild. *J Biomed Biotechnol,* 2010**,** 753675.
Hamada, H., Suzuki, M., Yuasa, S., Mimura, N., Shinozuka, N., Takada, Y., Nishino, T., Nakaya, H., Koseki, H. & Aoe, T. 2004. Dilated cardiomyopathy caused by aberrant endoplasmic reticulum quality control in mutant KDEL receptor transgenic mice. *Mol Cell Biol,* 24**,** 8007-17.
Hamel, L. P., Benchabane, M., Nicole, M. C., Major, I. T., Morency, M. J., Pelletier, G., Beaudoin, N., Sheen, J. & Seguin, A. 2011. Stress-responsive mitogen-activated protein kinases interact with the EAR motif of a poplar zinc finger protein and mediate its degradation through the 26S proteasome. *Plant Physiol,* 157**,** 1379-93.
Hammond, C. & Helenius, A. 1994. Quality control in the secretory pathway: retention of a misfolded viral membrane glycoprotein involves cycling between the ER, intermediate compartment, and Golgi apparatus. *J Cell Biol,* 126**,** 41-52.
Hayashi, C., Ono, Y., Doi, N., Kitamura, F., Tagami, M., Mineki, R., Arai, T., Taguchi, H., Yanagida, M., Hirner, S., Labeit, D., Labeit, S. & Sorimachi, H. 2008. Multiple molecular interactions implicate the connectin/titin N2A region as a modulating scaffold for p94/calpain 3 activity in skeletal muscle. *J Biol Chem,* 283**,** 14801-14.
Hedberg, C., Melberg, A., Dahlbom, K. & Oldfors, A. 2013. Hereditary myopathy with early respiratory failure is caused by mutations in the titin FN3 119 domain. *Brain*.
Heierhorst, J., Tang, X., Lei, J., Probst, W. C., Weiss, K. R., Kemp, B. E. & Benian, G. M. 1996. Substrate specificity and inhibitor sensitivity of Ca2+/S100-dependent twitchin kinases. *Eur J Biochem,* 242**,** 454-9.
Helmes, M., Lim, C. C., Liao, R., Bharti, A., Cui, L. & Sawyer, D. B. 2003. Titin determines the Frank-Starling relation in early diastole. *J Gen Physiol,* 121**,** 97-110.
Herman, D. S., Lam, L., Taylor, M. R. G., Wang, L. B., Teekakirikul, P., Christodoulou, D., Conner, L., Depalma, S. R., Mcdonough, B., Sparks, E., Teodorescu, D. L., Cirino, A. L., Banner, N. R., Pennell, D. J., Graw, S., Merlo, M., Di Lenarda, A., Sinagra, G., Bos, J. M., Ackerman, M. J., Mitchell, R. N., Murry, C. E., Lakdawala, N. K., Ho, C. Y., Barton, P. J. R., Cook, S. A., Mestroni, L., Seidman, J. G. & Seidman, C. E. 2012. Truncations of Titin Causing Dilated Cardiomyopathy. *New England Journal of Medicine,* 366**,** 619-628.
Hidalgo, C., Hudson, B., Bogomolovas, J., Zhu, Y., Anderson, B., Greaser, M., Labeit, S. & Granzier, H. 2009. PKC phosphorylation of titin's PEVK element: a novel and conserved pathway for modulating myocardial stiffness. *Circ Res,* 105**,** 631-8, 17 p following 638.
Hirner, S., Krohne, C., Schuster, A., Hoffmann, S., Witt, S., Erber, R., Sticht, C., Gasch, A., Labeit, S. & Labeit, D. 2008. MuRF1-dependent regulation of systemic carbohydrate metabolism as revealed from transgenic mouse studies. *J Mol Biol,* 379**,** 666-77.
Hoshijima, M. 2006. Mechanical stress-strain sensors embedded in cardiac cytoskeleton: Z disk, titin, and associated structures. *Am J Physiol Heart Circ Physiol,* 290**,** H1313-25.

Houmeida, A., Holt, J., Tskhovrebova, L. & Trinick, J. 1995. Studies of the interaction between titin and myosin. *J Cell Biol,* 131**,** 1471-81.
Hu, Ly, Kontrogianni-Konstantopoulos, A. 2013. The kinase domains of obscurin interact with intercellular adhesion proteins. *FASEB J* 27, 2001-12.
Huang, H., Hittle, J., Zappacosta, F., Annan, R. S., Hershko, A. & Yen, T. J. 2008. Phosphorylation sites in BubR1 that regulate kinetochore attachment, tension, and mitotic exit. *J Cell Biol,* 183**,** 667-80.
Hubbers, C. U., Clemen, C. S., Kesper, K., Boddrich, A., Hofmann, A., Kamarainen, O., Tolksdorf, K., Stumpf, M., Reichelt, J., Roth, U., Krause, S., Watts, G., Kimonis, V., Wattjes, M. P., Reimann, J., Thal, D. R., Biermann, K., Evert, B. O., Lochmuller, H., Wanker, E. E., Schoser, B. G., Noegel, A. A. & Schroder, R. 2007. Pathological consequences of VCP mutations on human striated muscle. *Brain,* 130**,** 381-93.
Hutchinson, E. G. & Thornton, J. M. 1994. A revised set of potentials for beta-turn formation in proteins. *Protein Sci,* 3**,** 2207-16.
Improta, S., Politou, A. S. & Pastore, A. 1996. Immunoglobulin-like modules from titin I-band: extensible components of muscle elasticity. *Structure,* 4**,** 323-37.
Isaacs, W. B., Kim, I. S., Struve, A. & Fulton, A. B. 1992. Association of titin and myosin heavy chain in developing skeletal muscle. *Proc Natl Acad Sci U S A,* 89**,** 7496-500.
Itoh-Satoh, M., Hayashi, T., Nishi, H., Koga, Y., Arimura, T., Koyanagi, T., Takahashi, M., Hohda, S., Ueda, K., Nouchi, T., Hiroe, M., Marumo, F., Imaizumi, T., Yasunami, M. & Kimura, A. 2002. Titin mutations as the molecular basis for dilated cardiomyopathy. *Biochem Biophys Res Commun,* 291**,** 385-93.
Iyer, G. H., Garrod, S., Woods, V. L., Jr. & Taylor, S. S. 2005. Catalytic independent functions of a protein kinase as revealed by a kinase-dead mutant: study of the Lys72His mutant of cAMP-dependent kinase. *J Mol Biol,* 351**,** 1110-22.
Jin, J. P. 2000. Titin-thin filament interaction and potential role in muscle function. *Adv Exp Med Biol,* 481**,** 319-33; discussion 334-5.
Johnson, B. A. 2004. Using NMRView to visualize and analyze the NMR spectra of macromolecules. *Methods Mol Biol,* 278**,** 313-52.
Kabsch, W. 2010. Xds. *Acta Crystallogr D Biol Crystallogr,* 66**,** 125-32.
Kaisto, T. & Metsikko, K. 2003. Distribution of the endoplasmic reticulum and its relationship with the sarcoplasmic reticulum in skeletal myofibers. *Exp Cell Res,* 289**,** 47-57.
Kedar, V., Mcdonough, H., Arya, R., Li, H. H., Rockman, H. A. & Patterson, C. 2004. Muscle-specific RING finger 1 is a bona fide ubiquitin ligase that degrades cardiac troponin I. *Proc Natl Acad Sci U S A,* 101**,** 18135-40.
Keinan, A. & Clark, A. G. 2012. Recent explosive human population growth has resulted in an excess of rare genetic variants. *Science,* 336**,** 740-3.
Khan, M. M., Strack, S., Wild, F., Hanashima, A., Gasch, A., Brohm, K., Reischl, M., Carnio, S., Labeit, D., Sandri, M., Labeit, S. & Rudolf, R. 2014. Role of autophagy, SQSTM1, SH3GLB1, and TRIM63 in the turnover of nicotinic acetylcholine receptors. *Autophagy,* 10**,** 123-36.
Knoll, R. & Buyandelger, B. 2013. Z-disc transcriptional coupling, sarcomeroptosis and Mechanoptosis [corrected]. *Cell Biochem Biophys,* 66**,** 65-71.
Knoll, R., Hoshijima, M. & Chien, K. R. 2002. Muscle LIM protein in heart failure. *Exp Clin Cardiol,* 7**,** 104-5.

Knoll, R., Linke, W. A., Zou, P., Miocic, S., Kostin, S., Buyandelger, B., Ku, C. H., Neef, S., Bug, M., Schafer, K., Knoll, G., Felkin, L. E., Wessels, J., Toischer, K., Hagn, F., Kessler, H., Didie, M., Quentin, T., Maier, L. S., Teucher, N., Unsold, B., Schmidt, A., Birks, E. J., Gunkel, S., Lang, P., Granzier, H., Zimmermann, W. H., Field, L. J., Faulkner, G., Dobbelstein, M., Barton, P. J., Sattler, M., Wilmanns, M. & Chien, K. R. 2011. Telethonin deficiency is associated with maladaptation to biomechanical stress in the mammalian heart. *Circ Res,* 109**,** 758-69.

Knoll, R., Postel, R., Wang, J., Kratzner, R., Hennecke, G., Vacaru, A. M., Vakeel, P., Schubert, C., Murthy, K., Rana, B. K., Kube, D., Knoll, G., Schafer, K., Hayashi, T., Holm, T., Kimura, A., Schork, N., Toliat, M. R., Nurnberg, P., Schultheiss, H. P., Schaper, W., Schaper, J., Bos, E., Den Hertog, J., Van Eeden, F. J., Peters, P. J., Hasenfuss, G., Chien, K. R. & Bakkers, J. 2007. Laminin-alpha4 and integrin-linked kinase mutations cause human cardiomyopathy via simultaneous defects in cardiomyocytes and endothelial cells. *Circulation,* 116**,** 515-25.

Konagurthu, A. S., Whisstock, J. C., Stuckey, P. J. & Lesk, A. M. 2006. MUSTANG: a multiple structural alignment algorithm. *Proteins,* 64**,** 559-74.

Konarev, P. V., Volkov, V. V., Sokolova, A. V., Koch, M. H. J. & Svergun, D. I. 2003. PRIMUS: a Windows PC-based system for small-angle scattering data analysis. *Journal of Applied Crystallography,* 36**,** 1277-1282.

Kontrogianni-Konstantopoulos, A. & Bloch, R. J. 2003. The hydrophilic domain of small ankyrin-1 interacts with the two N-terminal immunoglobulin domains of titin. *J Biol Chem,* 278**,** 3985-91.

Kontrogianni-Konstantopoulos, A., Catino, D. H., Strong, J. C., Randall, W. R. & Bloch, R. J. 2004. Obscurin regulates the organization of myosin into A bands. *Am J Physiol Cell Physiol,* 287**,** C209-17.

Kooij, V., Saes, M., Jaquet, K., Zaremba, R., Foster, D. B., Murphy, A. M., Dos Remedios, C., Van Der Velden, J. & Stienen, G. J. 2010. Effect of troponin I Ser23/24 phosphorylation on Ca2+-sensitivity in human myocardium depends on the phosphorylation background. *J Mol Cell Cardiol,* 48**,** 954-63.

Kopito, R. R. 1999. Biosynthesis and degradation of CFTR. *Physiol Rev,* 79**,** S167-73.

Labeit, S., Gautel, M., Lakey, A. & Trinick, J. 1992. Towards a molecular understanding of titin. *EMBO J,* 11**,** 1711-6.

Labeit, S., Kolmerer, B. & Linke, W. A. 1997. The giant protein titin. Emerging roles in physiology and pathophysiology. *Circ Res,* 80**,** 290-4.

Labeit, S., Lahmers, S., Burkart, C., Fong, C., Mcnabb, M., Witt, S., Witt, C., Labeit, D. & Granzier, H. 2006. Expression of distinct classes of titin isoforms in striated and smooth muscles by alternative splicing, and their conserved interaction with filamins. *J Mol Biol,* 362**,** 664-81.

Lange, A., Wickstrom, S. A., Jakobson, M., Zent, R., Sainio, K. & Fassler, R. 2009a. Integrin-linked kinase is an adaptor with essential functions during mouse development. *Nature,* 461**,** 1002-6.

Lange, S., Auerbach, D., Mcloughlin, P., Perriard, E., Schafer, B. W., Perriard, J. C. & Ehler, E. 2002. Subcellular targeting of metabolic enzymes to titin in heart muscle may be mediated by DRAL/FHL-2. *J Cell Sci,* 115**,** 4925-36.

Lange, S., Ouyang, K., Meyer, G., Cui, L., Cheng, H., Lieber, R. L. & Chen, J. 2009b. Obscurin determines the architecture of the longitudinal sarcoplasmic reticulum. *J Cell Sci,* 122**,** 2640-50.

Lange, S., Xiang, F., Yakovenko, A., Vihola, A., Hackman, P., Rostkova, E., Kristensen, J., Brandmeier, B., Franzen, G., Hedberg, B., Gunnarsson, L. G., Hughes, S. M., Marchand, S., Sejersen, T., Richard, I., Edstrom, L., Ehler, E., Udd, B. & Gautel, M. 2005. The kinase domain of titin controls muscle gene expression and protein turnover. *Science,* 308**,** 1599-603.

Langer, G., Cohen, S. X., Lamzin, V. S. & Perrakis, A. 2008. Automated macromolecular model building for X-ray crystallography using ARP/wARP version 7. *Nat Protoc,* 3**,** 1171-9.

Lee, E. H., Hsin, J., Von Castelmur, E., Mayans, O. & Schulten, K. 2010. Tertiary and secondary structure elasticity of a six-Ig titin chain. *Biophys J,* 98**,** 1085-95.

Lei, J., Tang, X., Chambers, T. C., Pohl, J. & Benian, G. M. 1994. Protein kinase domain of twitchin has protein kinase activity and an autoinhibitory region. *J Biol Chem,* 269**,** 21078-85.

Ling, P., Yao, Z., Meyer, C. F., Wang, X. S., Oehrl, W., Feller, S. M. & Tan, T. H. 1999. Interaction of hematopoietic progenitor kinase 1 with adapter proteins Crk and CrkL leads to synergistic activation of c-Jun N-terminal kinase. *Mol Cell Biol,* 19**,** 1359-68.

Linke, W. A. & Kruger, M. 2010. The giant protein titin as an integrator of myocyte signaling pathways. *Physiology (Bethesda),* 25**,** 186-98.

Linke, W. A., Kulke, M., Li, H., Fujita-Becker, S., Neagoe, C., Manstein, D. J., Gautel, M. & Fernandez, J. M. 2002. PEVK domain of titin: an entropic spring with actin-binding properties. *J Struct Biol,* 137**,** 194-205.

Liu, X., Rao, L., Zhou, B., Zhang, B. L., Wang, Y. Y., Chen, B., Wu, Y. & Huang, P. 2008. [Titin gene mutations in Chinese patients with dilated cardiomyopathy]. *Zhonghua Xin Xue Guan Bing Za Zhi,* 36**,** 1066-9.

Malureanu, L. A., Jeganathan, K. B., Hamada, M., Wasilewski, L., Davenport, J. & Van Deursen, J. M. 2009. BubR1 N terminus acts as a soluble inhibitor of cyclin B degradation by APC/C(Cdc20) in interphase. *Dev Cell,* 16**,** 118-31.

Marino, M., Svergun, D. I., Kreplak, L., Konarev, P. V., Maco, B., Labeit, D. & Mayans, O. 2005. Poly-Ig tandems from I-band titin share extended domain arrangements irrespective of the distinct features of their modular constituents. *J Muscle Res Cell Motil,* 26**,** 355-65.

Marino, M., Zou, P., Svergun, D., Garcia, P., Edlich, C., Simon, B., Wilmanns, M., Muhle-Goll, C. & Mayans, O. 2006. The Ig doublet Z1Z2: a model system for the hybrid analysis of conformational dynamics in Ig tandems from titin. *Structure,* 14**,** 1437-47.

Matsumoto, Y., Hayashi, T., Inagaki, N., Takahashi, M., Hiroi, S., Nakamura, T., Arimura, T., Nakamura, K., Ashizawa, N., Yasunami, M., Ohe, T., Yano, K. & Kimura, A. 2005. Functional analysis of titin/connectin N2-B mutations found in cardiomyopathy. *J Muscle Res Cell Motil,* 26**,** 367-74.

Matulis, D., Kranz, J. K., Salemme, F. R. & Todd, M. J. 2005. Thermodynamic stability of carbonic anhydrase: measurements of binding affinity and stoichiometry using ThermoFluor. *Biochemistry,* 44**,** 5258-66.

Mayans, O., Benian, G. M., Simkovic, F. & Rigden, D. J. 2013. Mechanistic and functional diversity in the mechanosensory kinases of the titin-like family. *Biochem Soc Trans,* 41**,** 1066-71.

Mayans, O. & Labeit, S. 2012. MuRFs: specialized members of the TRIM/RBCC family with roles in the regulation of the trophic state of muscle and its metabolism. *Adv Exp Med Biol,* 770**,** 119-29.

Mayans, O., Van Der Ven, P. F., Wilm, M., Mues, A., Young, P., Furst, D. O., Wilmanns, M. & Gautel, M. 1998. Structural basis for activation of the titin kinase domain during myofibrillogenesis. *Nature,* 395**,** 863-9.

Mayans, O. & Wilmanns, M. 1999. X-ray analysis of protein crystals with thin-plate morphology. *Journal of Synchrotron Radiation,* 6**,** 1016-1020.

Mayans, O., Wuerges, J., Canela, S., Gautel, M. & Wilmanns, M. 2001. Structural evidence for a possible role of reversible disulphide bridge formation in the elasticity of the muscle protein titin. *Structure,* 9**,** 331-40.

Mccoy, A. J. 2007. Solving structures of protein complexes by molecular replacement with Phaser. *Acta Crystallogr D Biol Crystallogr,* 63**,** 32-41.

Mccoy, A. J., Grosse-Kunstleve, R. W., Adams, P. D., Winn, M. D., Storoni, L. C. & Read, R. J. 2007. Phaser crystallographic software. *J Appl Crystallogr,* 40**,** 658-674.

Mcelhinny, A. S., Kakinuma, K., Sorimachi, H., Labeit, S. & Gregorio, C. C. 2002. Muscle-specific RING finger-1 interacts with titin to regulate sarcomeric M-line and thick filament structure and may have nuclear functions via its interaction with glucocorticoid modulatory element binding protein-1. *J Cell Biol,* 157**,** 125-36.

Mckenna, A., Hanna, M., Banks, E., Sivachenko, A., Cibulskis, K., Kernytsky, A., Garimella, K., Altshuler, D., Gabriel, S., Daly, M. & Depristo, M. A. 2010. The Genome Analysis Toolkit: a MapReduce framework for analyzing next-generation DNA sequencing data. *Genome Res,* 20**,** 1297-303.

Meder, B., Haas, J., Keller, A., Heid, C., Just, S., Borries, A., Boisguerin, V., Scharfenberger-Schmeer, M., Stahler, P., Beier, M., Weichenhan, D., Strom, T. M., Pfeufer, A., Korn, B., Katus, H. A. & Rottbauer, W. 2011. Targeted next-generation sequencing for the molecular genetic diagnostics of cardiomyopathies. *Circ Cardiovasc Genet,* 4**,** 110-22.

Mertens, H. D., Piljic, A., Schultz, C. & Svergun, D. I. 2012. Conformational analysis of a genetically encoded FRET biosensor by SAXS. *Biophys J,* 102**,** 2866-75.

Mestroni, L. & Taylor, M. R. 2013. Genetics and genetic testing of dilated cardiomyopathy: a new perspective. *Discov Med,* 15**,** 43-9.

Metzger, M. B., Maurer, M. J., Dancy, B. M. & Michaelis, S. 2008. Degradation of a cytosolic protein requires endoplasmic reticulum-associated degradation machinery. *J Biol Chem,* 283**,** 32302-16.

Miller, M. K., Bang, M. L., Witt, C. C., Labeit, D., Trombitas, C., Watanabe, K., Granzier, H., Mcelhinny, A. S., Gregorio, C. C. & Labeit, S. 2003. The muscle ankyrin repeat proteins: CARP, ankrd2/Arpp and DARP as a family of titin filament-based stress response molecules. *J Mol Biol,* 333**,** 951-64.

Moriscot, A. S., Baptista, I. L., Bogomolovas, J., Witt, C., Hirner, S., Granzier, H. & Labeit, S. 2010. MuRF1 is a muscle fiber-type II associated factor and together with MuRF2 regulates type-II fiber trophicity and maintenance. *J Struct Biol,* 170**,** 344-53.

Mrosek, M., Labeit, D., Witt, S., Heerklotz, H., Von Castelmur, E., Labeit, S. & Mayans, O. 2007. Molecular determinants for the recruitment of the ubiquitin-ligase MuRF-1 onto M-line titin. *FASEB J,* 21**,** 1383-92.

Mueller-Dieckmann, C., Panjikar, S., Schmidt, A., Mueller, S., Kuper, J., Geerlof, A., Wilmanns, M., Singh, R. K., Tucker, P. A. & Weiss, M. S. 2007. On the routine use of soft X-rays in macromolecular crystallography. Part IV. Efficient determination of anomalous substructures in biomacromolecules

using longer X-ray wavelengths. *Acta Crystallogr D Biol Crystallogr,* 63**,** 366-80.
Mues, A., Van Der Ven, P. F., Young, P., Furst, D. O. & Gautel, M. 1998. Two immunoglobulin-like domains of the Z-disc portion of titin interact in a conformation-dependent way with telethonin. *FEBS Lett,* 428**,** 111-4.
Muller, S., Lange, S., Gautel, M. & Wilmanns, M. 2007. Rigid conformation of an immunoglobulin domain tandem repeat in the A-band of the elastic muscle protein titin. *J Mol Biol,* 371**,** 469-80.
Nelson, M. R., Wegmann, D., Ehm, M. G., Kessner, D., St Jean, P., Verzilli, C., Shen, J., Tang, Z., Bacanu, S. A., Fraser, D., Warren, L., Aponte, J., Zawistowski, M., Liu, X., Zhang, H., Zhang, Y., Li, J., Li, Y., Li, L., Woollard, P., Topp, S., Hall, M. D., Nangle, K., Wang, J., Abecasis, G., Cardon, L. R., Zollner, S., Whittaker, J. C., Chissoe, S. L., Novembre, J. & Mooser, V. 2012. An abundance of rare functional variants in 202 drug target genes sequenced in 14,002 people. *Science,* 337**,** 100-4.
Nordstrand, K., Sandstrom, A., Aslund, F., Holmgren, A., Otting, G. & Berndt, K. D. 2000. NMR structure of oxidized glutaredoxin 3 from Escherichia coli. *J Mol Biol,* 303**,** 423-32.
Nori, A., Valle, G., Bortoloso, E., Turcato, F. & Volpe, P. 2006. Calsequestrin targeting to sarcoplasmic reticulum of skeletal muscle fibers. *Am J Physiol Cell Physiol,* 291**,** C245-53.
Norton, N., Li, D. & Hershberger, R. E. 2012a. Next-generation sequencing to identify genetic causes of cardiomyopathies. *Curr Opin Cardiol,* 27**,** 214-20.
Norton, N., Robertson, P. D., Rieder, M. J., Zuchner, S., Rampersaud, E., Martin, E., Li, D., Nickerson, D. A. & Hershberger, R. E. 2012b. Evaluating pathogenicity of rare variants from dilated cardiomyopathy in the exome era. *Circ Cardiovasc Genet,* 5**,** 167-74.
Obermann, W. M., Gautel, M., Weber, K. & Furst, D. O. 1997. Molecular structure of the sarcomeric M band: mapping of titin and myosin binding domains in myomesin and the identification of a potential regulatory phosphorylation site in myomesin. *EMBO J,* 16**,** 211-20.
Ohlsson, M., Hedberg, C., Bradvik, B., Lindberg, C., Tajsharghi, H., Danielsson, O., Melberg, A., Udd, B., Martinsson, T. & Oldfors, A. 2012. Hereditary myopathy with early respiratory failure associated with a mutation in A-band titin. *Brain,* 135**,** 1682-94.
Ojima, K., Kawabata, Y., Nakao, H., Nakao, K., Doi, N., Kitamura, F., Ono, Y., Hata, S., Suzuki, H., Kawahara, H., Bogomolovas, J., Witt, C., Ottenheijm, C., Labeit, S., Granzier, H., Toyama-Sorimachi, N., Sorimachi, M., Suzuki, K., Maeda, T., Abe, K., Aiba, A. & Sorimachi, H. 2010. Dynamic distribution of muscle-specific calpain in mice has a key role in physical-stress adaptation and is impaired in muscular dystrophy. *J Clin Invest,* 120**,** 2672-83.
Peled, Y., Gramlich, M., Yoskovitz, G., Feinberg, M. S., Afek, A., Polak-Charcon, S., Pras, E., Sela, B. A., Konen, E., Weissbrod, O., Geiger, D., Gordon, P. M., Thierfelder, L., Freimark, D., Gerull, B. & Arad, M. 2014. Titin mutation in familial restrictive cardiomyopathy. *Int J Cardiol,* 171**,** 24-30.
Peng, J., Raddatz, K., Labeit, S., Granzier, H. & Gotthardt, M. 2005. Muscle atrophy in titin M-line deficient mice. *J Muscle Res Cell Motil,* 26**,** 381-8.
Peng, J., Raddatz, K., Molkentin, J. D., Wu, Y., Labeit, S., Granzier, H. & Gotthardt, M. 2007. Cardiac hypertrophy and reduced contractility in hearts deficient in the titin kinase region. *Circulation,* 115**,** 743-51.

Pernigo, S., Fukuzawa, A., Bertz, M., Holt, M., Rief, M., Steiner, R. A. & Gautel, M. 2010. Structural insight into M-band assembly and mechanics from the titin-obscurin-like-1 complex. *Proc Natl Acad Sci U S A,* 107**,** 2908-13.

Petoukhov, M. V., Konarev, P. V., Kikhney, A. G. & Svergun, D. I. 2007. ATSAS 2.1 - towards automated and web-supported small-angle scattering data analysis. *Journal of Applied Crystallography,* 40**,** S223-S228.

Pfeffer, G., Griffin, H., Pyle, A., Horvath, R. & Chinnery, P. F. 2013. Reply: Hereditary myopathy with early respiratory failure is caused by mutations in the titin FN3 119 domain. *Brain*.

Pfuhl, M., Improta, S., Politou, A. S. & Pastore, A. 1997. When a module is also a domain: the role of the N terminus in the stability and the dynamics of immunoglobulin domains from titin. *J Mol Biol,* 265**,** 242-56.

Pfuhl, M. & Pastore, A. 1995. Tertiary structure of an immunoglobulin-like domain from the giant muscle protein titin: a new member of the I set. *Structure,* 3**,** 391-401.

Pinotsis, N., Petoukhov, M., Lange, S., Svergun, D., Zou, P., Gautel, M. & Wilmanns, M. 2006. Evidence for a dimeric assembly of two titin/telethonin complexes induced by the telethonin C-terminus. *J Struct Biol,* 155**,** 239-50.

Polge, C., Heng, A. E., Jarzaguet, M., Ventadour, S., Claustre, A., Combaret, L., Bechet, D., Matondo, M., Uttenweiler-Joseph, S., Monsarrat, B., Attaix, D. & Taillandier, D. 2011. Muscle actin is polyubiquitinylated in vitro and in vivo and targeted for breakdown by the E3 ligase MuRF1. *FASEB J,* 25**,** 3790-802.

Puchner, E. M., Alexandrovich, A., Kho, A. L., Hensen, U., Schafer, L. V., Brandmeier, B., Grater, F., Grubmuller, H., Gaub, H. E. & Gautel, M. 2008. Mechanoenzymatics of titin kinase. *Proc Natl Acad Sci U S A,* 105**,** 13385-90.

Puchner, E. M. & Gaub, H. E. 2010. Exploring the conformation-regulated function of titin kinase by mechanical pump and probe experiments with single molecules. *Angew Chem Int Ed Engl,* 49**,** 1147-50.

Rahkila, P., Alakangas, A., Vaananen, K. & Metsikko, K. 1996. Transport pathway, maturation, and targetting of the vesicular stomatitis virus glycoprotein in skeletal muscle fibers. *J Cell Sci,* 109 (Pt 6)**,** 1585-96.

Raynaud, F., Fernandez, E., Coulis, G., Aubry, L., Vignon, X., Bleimling, N., Gautel, M., Benyamin, Y. & Ouali, A. 2005. Calpain 1-titin interactions concentrate calpain 1 in the Z-band edges and in the N2-line region within the skeletal myofibril. *FEBS J,* 272**,** 2578-90.

Richardson, J. & Richardson, D. 1989. Principles and Patterns of Protein Conformation. *In:* FASMAN, G. (ed.) *Prediction of Protein Structure and the Principles of Protein Conformation.* Springer US.

Roder, I. V., Choi, K. R., Reischl, M., Petersen, Y., Diefenbacher, M. E., Zaccolo, M., Pozzan, T. & Rudolf, R. 2010. Myosin Va cooperates with PKA RIalpha to mediate maintenance of the endplate in vivo. *Proc Natl Acad Sci U S A,* 107**,** 2031-6.

Rudolf, R., Bogomolovas, J., Strack, S., Choi, K. R., Khan, M. M., Wagner, A., Brohm, K., Hanashima, A., Gasch, A., Labeit, D. & Labeit, S. 2013. Regulation of nicotinic acetylcholine receptor turnover by MuRF1 connects muscle activity to endo/lysosomal and atrophy pathways. *Age (Dordr),* 35**,** 1663-74.

Satoh, M., Takahashi, M., Sakamoto, T., Hiroe, M., Marumo, F. & Kimura, A. 1999. Structural analysis of the titin gene in hypertrophic cardiomyopathy:

identification of a novel disease gene. *Biochem Biophys Res Commun,* 262**,** 411-7.
Sauer, F., Vahokoski, J., Song, Y. H. & Wilmanns, M. 2010. Molecular basis of the head-to-tail assembly of giant muscle proteins obscurin-like 1 and titin. *EMBO Rep,* 11**,** 534-40.
Scheeff, E. D. & Bourne, P. E. 2005. Structural evolution of the protein kinase-like superfamily. *PLoS Comput Biol,* 1**,** e49.
Scheeff, E. D., Eswaran, J., Bunkoczi, G., Knapp, S. & Manning, G. 2009. Structure of the pseudokinase VRK3 reveals a degraded catalytic site, a highly conserved kinase fold, and a putative regulatory binding site. *Structure,* 17**,** 128-38.
Schu, P. V., Takegawa, K., Fry, M. J., Stack, J. H., Waterfield, M. D. & Emr, S. D. 1993. Phosphatidylinositol 3-kinase encoded by yeast VPS34 gene essential for protein sorting. *Science,* 260**,** 88-91.
Sen-Chowdhry, S., Syrris, P. & Mckenna, W. J. 2007. Role of genetic analysis in the management of patients with arrhythmogenic right ventricular dysplasia/cardiomyopathy. *J Am Coll Cardiol,* 50**,** 1813-21.
Shaw, R. J., Kosmatka, M., Bardeesy, N., Hurley, R. L., Witters, L. A., Depinho, R. A. & Cantley, L. C. 2004. The tumor suppressor LKB1 kinase directly activates AMP-activated kinase and regulates apoptosis in response to energy stress. *Proc Natl Acad Sci U S A,* 101**,** 3329-35.
Shymanets, A., Ahmadian, M. R. & Nurnberg, B. 2009. Gbetagamma-copurified lipid kinase impurity from Sf9 cells. *Protein Pept Lett,* 16**,** 1053-6.
Sieck, G. C. & Prakash, Y. S. 1997. Cross-bridge kinetics in respiratory muscles. *Eur Respir J,* 10**,** 2147-58.
Sim, N. L., Kumar, P., Hu, J., Henikoff, S., Schneider, G. & Ng, P. C. 2012. SIFT web server: predicting effects of amino acid substitutions on proteins. *Nucleic Acids Res,* 40**,** W452-7.
Sorimachi, H., Kimura, S., Kinbara, K., Kazama, J., Takahashi, M., Yajima, H., Ishiura, S., Sasagawa, N., Nonaka, I., Sugita, H., Maruyama, K. & Suzuki, K. 1996. Structure and physiological functions of ubiquitous and tissue-specific calpain species. Muscle-specific calpain, p94, interacts with connectin/titin. *Adv Biophys,* 33**,** 101-22.
Stacklies, W., Vega, M. C., Wilmanns, M. & Grater, F. 2009. Mechanical network in titin immunoglobulin from force distribution analysis. *PLoS Comput Biol,* 5**,** e1000306.
Stahl, S. W., Puchner, E. M., Alexandrovich, A., Gautel, M. & Gaub, H. E. 2011. A conditional gating mechanism assures the integrity of the molecular force-sensor titin kinase. *Biophys J,* 101**,** 1978-86.
Suijkerbuijk, S. J., Van Dam, T. J., Karagoz, G. E., Von Castelmur, E., Hubner, N. C., Duarte, A. M., Vleugel, M., Perrakis, A., Rudiger, S. G., Snel, B. & Kops, G. J. 2012. The vertebrate mitotic checkpoint protein BUBR1 is an unusual pseudokinase. *Dev Cell,* 22**,** 1321-9.
Taylor, M., Graw, S., Sinagra, G., Barnes, C., Slavov, D., Brun, F., Pinamonti, B., Salcedo, E. E., Sauer, W., Pyxaras, S., Anderson, B., Simon, B., Bogomolovas, J., Labeit, S., Granzier, H. & Mestroni, L. 2011. Genetic variation in titin in arrhythmogenic right ventricular cardiomyopathy-overlap syndromes. *Circulation,* 124**,** 876-85.
Taylor, S. S., Shaw, A., Hu, J., Meharena, H. S. & Kornev, A. 2013. Pseudokinases from a structural perspective. *Biochem Soc Trans,* 41**,** 981-6.

Temmerman, K., Simon, B. & Wilmanns, M. 2013. Structural and functional diversity in the activity and regulation of DAPK-related protein kinases. *FEBS J,* 280**,** 5533-50.
Toro, C., Olive, M., Dalakas, M. C., Sivakumar, K., Bilbao, J. M., Tyndel, F., Vidal, N., Farrero, E., Sambuughin, N. & Goldfarb, L. G. 2013. Exome sequencing identifies titin mutations causing hereditary myopathy with early respiratory failure (HMERF) in families of diverse ethnic origins. *BMC Neurol,* 13**,** 29.
Trombitas, K., Greaser, M. L. & Pollack, G. H. 1997. Interaction between titin and thin filaments in intact cardiac muscle. *J Muscle Res Cell Motil,* 18**,** 345-51.
Trombitas, K. & Pollack, G. H. 1993. Elastic properties of the titin filament in the Z-line region of vertebrate striated muscle. *J Muscle Res Cell Motil,* 14**,** 416-22.
Trombitas, K., Pollack, G. H., Wright, J. & Wang, K. 1993. Elastic properties of titin filaments demonstrated using a "freeze-break" technique. *Cell Motil Cytoskeleton,* 24**,** 274-83.
Van Der Velden, J., Papp, Z., Zaremba, R., Boontje, N. M., De Jong, J. W., Owen, V. J., Burton, P. B., Goldmann, P., Jaquet, K. & Stienen, G. J. 2003. Increased Ca2+-sensitivity of the contractile apparatus in end-stage human heart failure results from altered phosphorylation of contractile proteins. *Cardiovasc Res,* 57**,** 37-47.
Van Dijk, S. J., Paalberends, E. R., Najafi, A., Michels, M., Sadayappan, S., Carrier, L., Boontje, N. M., Kuster, D. W., Van Slegtenhorst, M., Dooijes, D., Dos Remedios, C., Ten Cate, F. J., Stienen, G. J. & Van Der Velden, J. 2012. Contractile dysfunction irrespective of the mutant protein in human hypertrophic cardiomyopathy with normal systolic function. *Circ Heart Fail,* 5**,** 36-46.
Van Durme, J., Delgado, J., Stricher, F., Serrano, L., Schymkowitz, J. & Rousseau, F. 2011. A graphical interface for the FoldX forcefield. *Bioinformatics,* 27**,** 1711-2.
Von Castelmur, E., Marino, M., Svergun, D. I., Kreplak, L., Ucurum-Fotiadis, Z., Konarev, P. V., Urzhumtsev, A., Labeit, D., Labeit, S. & Mayans, O. 2008. A regular pattern of Ig super-motifs defines segmental flexibility as the elastic mechanism of the titin chain. *Proc Natl Acad Sci U S A,* 105**,** 1186-91.
Von Castelmur, E., Strumpfer, J., Franke, B., Bogomolovas, J., Barbieri, S., Qadota, H., Konarev, P. V., Svergun, D. I., Labeit, S., Benian, G. M., Schulten, K. & Mayans, O. 2012. Identification of an N-terminal inhibitory extension as the primary mechanosensory regulator of twitchin kinase. *Proc Natl Acad Sci U S A,* 109**,** 13608-13.
Wadosky, K. M., Rodriguez, J. E., Hite, R. L., Min, J. N., Walton, B. & Willis, M. S. 2014. Muscle RING Finger-1 Attenuates IGF-1-dependent cardiomyocyte hypertrophy by Inhibiting JNK Signaling. *Am J Physiol Endocrinol Metab*.
Weinert, S., Bergmann, N., Luo, X., Erdmann, B. & Gotthardt, M. 2006. M line-deficient titin causes cardiac lethality through impaired maturation of the sarcomere. *J Cell Biol,* 173**,** 559-70.
Wichter, T., Paul, T. M., Eckardt, L., Gerdes, P., Kirchhof, P., Bocker, D. & Breithardt, G. 2005. Arrhythmogenic right ventricular cardiomyopathy. Antiarrhythmic drugs, catheter ablation, or ICD? *Herz,* 30**,** 91-101.
Willis, M. S., Ike, C., Li, L., Wang, D. Z., Glass, D. J. & Patterson, C. 2007. Muscle ring finger 1, but not muscle ring finger 2, regulates cardiac hypertrophy in vivo. *Circ Res,* 100**,** 456-9.

Willis, M. S., Schisler, J. C., Li, L., Rodriguez, J. E., Hilliard, E. G., Charles, P. C. & Patterson, C. 2009. Cardiac muscle ring finger-1 increases susceptibility to heart failure in vivo. *Circ Res,* 105**,** 80-8.

Willis, M. S., Wadosky, K. M., Rodriguez, J. E., Schisler, J. C., Lockyer, P., Hilliard, E. G., Glass, D. J. & Patterson, C. 2014. Muscle ring finger 1 and muscle ring finger 2 are necessary but functionally redundant during developmental cardiac growth and regulate E2F1-mediated gene expression in vivo. *Cell Biochem Funct,* 32**,** 39-50.

Witt, C. C., Burkart, C., Labeit, D., Mcnabb, M., Wu, Y., Granzier, H. & Labeit, S. 2006. Nebulin regulates thin filament length, contractility, and Z-disk structure in vivo. *EMBO J,* 25**,** 3843-55.

Witt, C. C., Witt, S. H., Lerche, S., Labeit, D., Back, W. & Labeit, S. 2008. Cooperative control of striated muscle mass and metabolism by MuRF1 and MuRF2. *EMBO J,* 27**,** 350-60.

Witt, S. H., Granzier, H., Witt, C. C. & Labeit, S. 2005. MURF-1 and MURF-2 target a specific subset of myofibrillar proteins redundantly: towards understanding MURF-dependent muscle ubiquitination. *J Mol Biol,* 350**,** 713-22.

Yagawa, K., Yamano, K., Oguro, T., Maeda, M., Sato, T., Momose, T., Kawano, S. & Endo, T. 2010. Structural basis for unfolding pathway-dependent stability of proteins: vectorial unfolding versus global unfolding. *Protein Sci,* 19**,** 693-702.

Yoskovitz, G., Peled, Y., Gramlich, M., Lahat, H., Resnik-Wolf, H., Feinberg, M. S., Afek, A., Pras, E., Arad, M., Gerull, B. & Freimark, D. 2012. A novel titin mutation in adult-onset familial dilated cardiomyopathy. *Am J Cardiol,* 109**,** 1644-50.

Zhu, Y., Bogomolovas, J., Labeit, S. & Granzier, H. 2009. Single molecule force spectroscopy of the cardiac titin N2B element: effects of the molecular chaperone alphaB-crystallin with disease-causing mutations. *J Biol Chem,* 284**,** 13914-23.

Zou, P., Gautel, M., Geerlof, A., Wilmanns, M., Koch, M. H. & Svergun, D. I. 2003. Solution scattering suggests cross-linking function of telethonin in the complex with titin. *J Biol Chem,* 278**,** 2636-44.

Zou, P., Pinotsis, N., Lange, S., Song, Y. H., Popov, A., Mavridis, I., Mayans, O. M., Gautel, M. & Wilmanns, M. 2006. Palindromic assembly of the giant muscle protein titin in the sarcomeric Z-disk. *Nature,* 439**,** 229-33.

Chapter 8 Appendices

8.1 Major types of intrinsic human cardiomyopathies

Cardiomyopathy	Clinical features
Dilated	Gradual increase in left ventricular chamber volumes, wall thinning and change in geometry to more spherical, associated with the primary decline in systolic heart function.
Hypertrophic	Thickening of left ventricle, due to pathological hypertrophy associated with myocardial disarray (both myocytes and sarcomeres), cardiac fibrosis; altered chamber shape and biomechanical properties manifests in combined diastolic-systolic dysfunction, dynamic outflow obstruction and arrhythmias.
Arrhythmogenic right ventricle	Isolated thinning of right ventricle due to fibrofatty infiltration, causing an early conduction disturbances leading to the life-threatening arrhythmias
Restrictive	Rigid walls of cardiac chambers restrict the heart from stretching and filling blood properly. Primary severe diastolic dysfunction leading to the biartrial enlargement, elevated artrial pressure and left ventricle wall thickening, without chamber dilatation.

8.2 Appendix 1 Sequence conservation of VAIK and DFG motifs in TK-like kinases from vertebrates and invertebrates

Vertebrate titins	**VAIK**		**DFG**
Homo_sapiens	CVETSSKKT	**YMAK**FVKVKGTDQVLVK	TIKII**EFG**QARQL
Ailuropoda_melanoleuca	CVETSSKKT	**YMAK**FVKVKGTDQVLVK	TIKII**EFG**QARQL
Anolis_carolinensis	CVETATKKT	**YLAK**FVKVKGADQVLVK	IIKII**EFG**QARQL
Bos_taurus	CVETSSKKT	**YMAK**FVKVKGTDQVLVK	TIKII**EFG**QARQL
Callithrix_jacchus	CVETSSKKT	**YMAK**FVKVKGTDQVLVK	TIKII**EFG**QARQL
Canis_familiaris	CVETSSKKT	**YMAK**FVKVKGTDQVLVK	IIKII**EFG**QARQL
Cavia_porcellus	CVETSSKKT	**FMAK**FVKVKGTDQVLVK	VIKII**EFG**QARQL
Danio_rerio_A	CIETSSEKT	**YMAK**FVKVKGADQALVK	NVKII**ELG**QSRHL
Danio_rerio_B	SIEISSKKT	**FLAK**FIKVKGADRELVA	TIKII**EMG**QARLL
Dasypus_novemcinctus	CVETSSKKT	**YMAK**FVKVKGTDQVLVK	TIKII**EFG**QARQL
Dipodomys_ordii	CVETSSKKT	**FMAK**FVKVKGTDQVLVK	TIKII**EFG**QARQL
Echinops_telfairi	CVETSSKKT	**YMAK**FVKVKGTDQVLVK	TIKII**EFG**QARQL
Equus_caballus	CVETSSKKT	**YMAK**FVKVKGTDQVLVK	VIKII**EFG**QARQL
Erinaceus_europaeus	CVETSSKKT	**YMAK**FVKVKGTDQVLVK	IIKII**EFG**QARQL
Felis_catus	CVETSSKKT	**YMAK**FVKVKGTDQVLVK	SIKII**EFG**QARQL
Gadus_morhua_A	CVEIATKKT	**FMAK**FIKVKGMDRELVL	ELKII**EMG**QARLL
Gadus_morhua_B	CVEKSSERT	**YMAK**FVKVRGADQAIVK	NVKII**ELG**QCRHL
Gallus_gallus	CVEAVSKKT	**YLAK**FVKVKGADQVLVK	VVKIV**EFG**QARQL
Gasterosteus_aculeatus_A	CTEIATKKT	**FMAK**SIKVKGTDRELVL	TTKII**EMG**QARLL
Gorilla_gorilla	CVETSSKKT	**YMAK**FVKVKGTDQVLVK	TIKII**EFG**QAHQL
Ictidomys_tridecemlineatus	CVETSSKKT	**FMAK**FVKVKGTDQVLVK	TIKII**EFG**QARQL
Latimeria_chalumnae	CVENTSKKT	**YMAK**FVKVKGADQVLVK	LVKII**ELG**QARQL
Loxodonta_africana	CVETSSKKT	**FMAK**FVKVKGTDQVLVK	TVKII**EFG**QARQL
Macaca_mulatta	CVETSSKKT	**YMAK**FVKVKGTDQVLVK	TIKII**EFG**QARQL
Macropus_eugenii	CVETSSKKT	**YMAK**FVKVKGTDQVLVK	VIKII**EFG**QARQL
Meleagris_gallopavo	CVEAVSKKT	**YLAK**FVKVKGADQVLVK	VVKIV**EFG**QARQL
Microcebus_murinus	CVETSSKKT	**YMAK**FVKVKGTDQVLVK	TIKII**EFG**QARQL
Monodelphis_domestica	CVETSSKKT	**YMAK**FVKVKGTDQVLVK	TIKII**EFG**QARQL
Mus_musculus	CVETSSKRT	**FMAK**FVKVKGTDQVLVK	TIKII**EFG**QARQL
Myotis_lucifugus	CVETSSKKT	**YMAK**FVKVKGTDQVLVK	VIKII**EFG**QARQL
Nomascus_leucogenys	CVETSSKKT	**YMAK**FVKVKGTDQVLVK	TIKII**EFG**QARQL
Ochotona_princeps	CVETSSKKT	**FMAK**FVKVKGTDQVLIK	VIKII**EFG**QARQL
Oreochromis_niloticus	CVEISSEKT	**YMAK**FVKVRGADQTLVK	NVKII**ELG**QSRHL
Ornithorhynchus_anatinus	CVETSSKKT	**YMAK**FVKVKGTDQVLVK	TIKII**EFG**QARQL
Oryctolagus_cuniculus	CVETSSKKT	**FMAK**FVKVKGTDQVLVK	VIKII**EFG**QARQL
Oryzias_latipes_A	CTEIATKKT	**FMAK**FIKVKGTDRELVL	NIKII**DMG**QSRLL
Oryzias_latipes_B	CVNISSEKT	**YMAK**FVKVRGADQAIIK	NVKII**ELG**QSRHL
Otolemur_garnettii	CVETSSKKT	**YMAK**FVKVKGTDQVLVK	TIKII**EFG**QARQL
Pelodiscus_sinensis	CVETVSKKT	**FLAK**FVKVKGADQVLVK	IIKII**EFG**QARQL
Petromyzon_marinus	CVEISSKKT	**YMAK**FAKVKGADQGSTK	RVKLV**EFG**QARIL
Pongo_abelii	CVETSSKKT	**YMAK**FVKVKGTDQVLVK	TIKII**EFG**QARQL
Procavia_capensis	CVETSSKKT	**YMAK**FVKVKGTDQVLVK	TIKII**EFG**QARQL
Pteropus_vampyrus	CVETSSKKT	**YMAK**FVKVKGTDQVLVK	TIKII**EFG**QARQL
Rattus_norvegicus	CVETSSKKT	**FMAK**FVKVKGTDQVLVK	IIKII**EFG**QARQL
Sarcophilus_harrisii	CVETSSKKT	**YMAK**FVKVKGTDQVLVK	VIKII**EFG**QARQL
Sorex_araneus	CVETSSKKT	**YMAK**FVKVKGTDQVLVK	LIKII**EFG**QARQL
Sus_scrofa	CVETSSKKT	**YMAK**FVKVKGADQVLVK	TIKII**EFG**QARQL
Takifugu_rubripes_A	CVEIATKKT	**FMAK**FIKVKGTDRELVL	NIKII**EMG**QARLL
Takifugu_rubripes_B	CVDICSEKT	**YMAK**FVKVRGADQALVK	NVKII**ELG**QCRHL
Tetraodon_nigroviridis_A	CVEIATKRT	**FMAK**FIKVKGTDRELVL	TIKII**EMG**QARLL
Tupaia_belangeri	CVETSSKKT	**YMAK**FVKVKGTDQVLVK	TIKII**EFG**QARQL
Xenopus_tropicalis	CIENSSKKT	**YLAK**FVKVKGADQVLVK	TIKIT**EFG**QARQL
Cricetulus_griseus	CVETSSKKT	**FMAK**FVKVKGTDQVLVK	TIKII**EFG**QARQL
Mustela_putorius_furo	CVETSSKKT	**YMAK**FVKVKGTDQVLVK	TIKII**EFG**QARQL
Heterocephalus_glaber	CVETSSKKT	**FMAK**FVKVKGTDQVLVK	IIKII**EFG**QARQL
Xiphophorus_maculatus_A	CVEIATKKT	**FMAK**FIKVKGTDRELVL	NIKMI**EMG**QSRLL
Xiphophorus_maculatus_B	CVDISSEKT	**YMAK**FVKVRGADQAIIK	TVKII**ELG**QSRHL

Invertebrate titin-like kinases (include twitchin, projectin and TTN-1 kinases)

```
Caenorabditis_elegans          NNFAAKFVM .... ELKLIDFGLTAHL
Caenorhabditis_briggsae        NNFAAKFVM .... ELKLIDFGLTAHL
Caenorhabditis_remanei         NNFAAKFVM .... ELKLIDFGLTAHL
Ascaris_suum                   NTFAAKFVN .... QLKLIDFGLAAKL
Brugia_malayi                  NTFAAKFVN .... QLKLIDFGLAAKL
Loa_loa                        NTFAAKFVN .... QLKLIDFGLAAKL
Trichinella_spiralis           NVFAAKFVN .... VLKLIDFGLAAKL
Tribolium_castaneum            NIFAAKFIP .... NIKLIDFGLATKL
Pediculus_humanus              SIFAAKFIP .... NIKLIDFGLATKL
Procambarus_clarkii            NIFAAKFIP .... NVKLIDFGLATKL
Harpegnathos_saltator          NIFAAKFIP .... NVKLIDFGLATKL
Mytilus_galloprovincialis      RVFVAKFIN .... EVKMIDFGLATKL
Crassostrea_gigas              RVFVAKFIN .... NVKMIDFGLATKL
Aplysia californica            RVFVAKFIN .... SVKIIDFGLATKL
Drosophila_willstoni           NIFAAKFIP .... SVKLIDFGLATRL
Drosophila_pseudoobscura       NIFAAKFIP .... NVKLIDFGLATRL
Drosophila_persimilis          NIFAAKFIP .... NVKLIDFGLATRL
Drosophila_melanogaster        NIFAAKFIP .... NVKLIDFGLATRL
Aedes_aegypti                  NVFAAKFIP .... NVKLIDFGLATRL
Anopheles_darlingi             NVFAAKFIP .... NVKLIDFGLATRL
Anopheles_gambiae              NVFAAKFIP .... NVKLIDFGLATRL
Culex_quinquefasciatus         NVFAAKFIP .... NVKLIDFGLATRL
```

8.3 Appendix 3 Structure based alignment of Ig domains from titin I-band

N-termini of Ig domains are represented. *i+2* residue of β-turn between A' and B sheets is in red. Residue positions forming interdomain hydrophobic interaction in I9-I11 are in green and joined with bow. Non-glycine residues are underlined. Conserved glutamate between A' and B sheets is in blue. Residues are numbered according Uniprot entry Q8W742. Where possible crystal structures were used

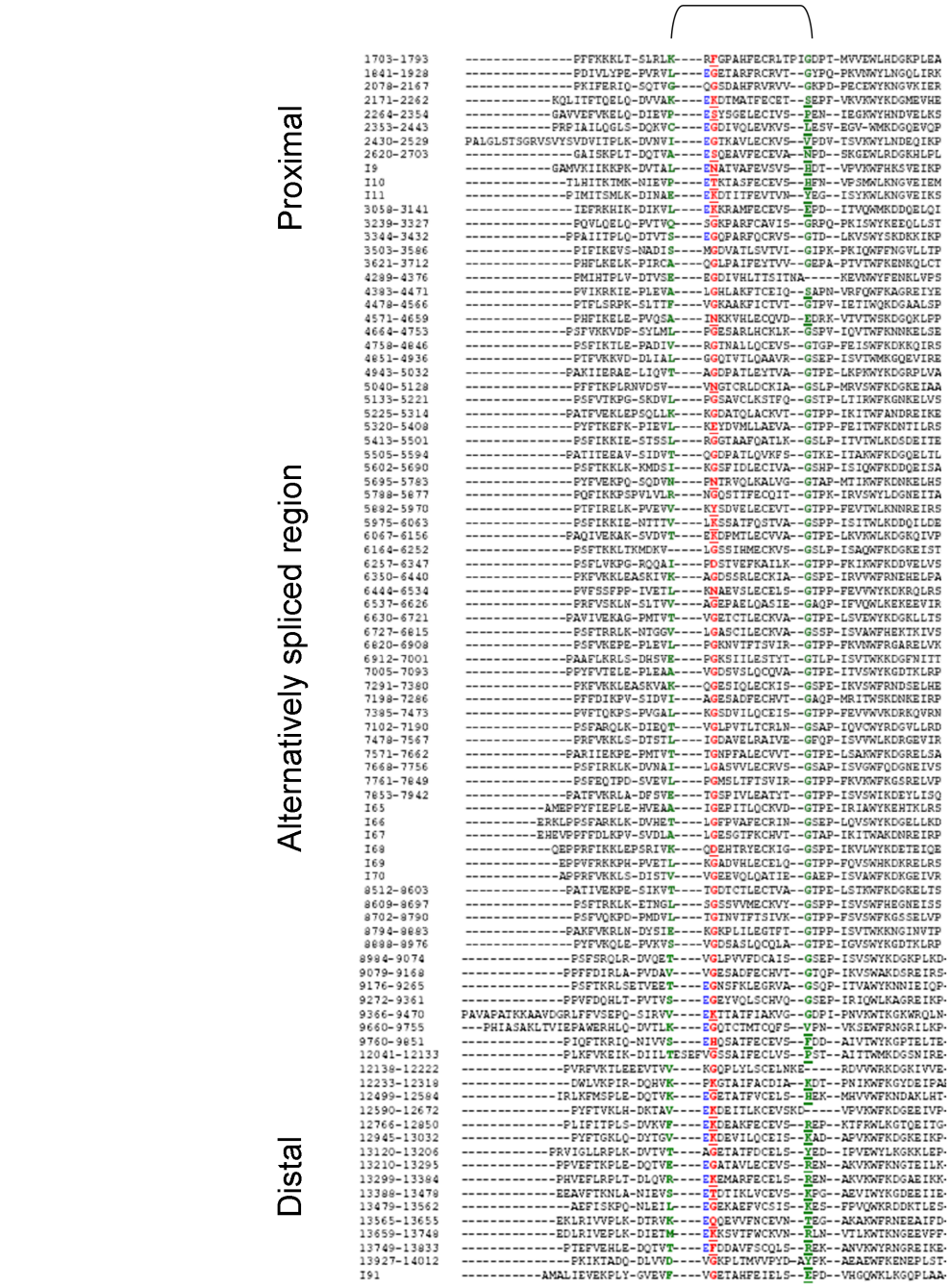
Proximal
Alternatively spliced region
Distal

8.4 Appendix 4 Personal Bibliography

8.4.1 Research papers

Bogomolovas, J., Simon, B., Sattler, M. & Stier, G. 2009. Screening of fusion partners for high yield expression and purification of bioactive viscotoxins. *Protein Expr Purif,* 64**,** 16-23.

Zhu, Y., **Bogomolovas, J**., Labeit, S. & Granzier, H. 2009. Single molecule force spectroscopy of the cardiac titin N2B element: effects of the molecular chaperone alphaB-crystallin with disease-causing mutations. *J Biol Chem,* 284**,** 13914-23.

Hidalgo, C., Hudson, B., **Bogomolovas, J**., Zhu, Y., Anderson, B., Greaser, M., Labeit, S. & Granzier, H. 2009. PKC phosphorylation of titin's PEVK element: a novel and conserved pathway for modulating myocardial stiffness. *Circ Res,* 105**,** 631-8

Moriscot, A. S., Baptista, I. L., **Bogomolovas, J**., Witt, C., Hirner, S., Granzier, H. & Labeit, S. 2010. MuRF1 is a muscle fiber-type II associated factor and together with MuRF2 regulates type-II fiber trophicity and maintenance. *J Struct Biol,* 170**,** 344-53

Anderson, B. R., **Bogomolovas, J**., Labeit, S. & Granzier, H. 2010. The effects of PKCalpha phosphorylation on the extensibility of titin's PEVK element. *J Struct Biol,* 170**,** 270-7.

Ojima, K., Kawabata, Y., Nakao, H., Nakao, K., Doi, N., Kitamura, F., Ono, Y., Hata, S., Suzuki, H., Kawahara, H., **Bogomolovas, J**., Witt, C., Ottenheijm, C., Labeit, S., Granzier, H., Toyama-Sorimachi, N., Sorimachi, M., Suzuki, K., Maeda, T., Abe, K., Aiba, A. & Sorimachi, H. 2010. Dynamic distribution of muscle-specific calpain in mice has a key role in physical-stress adaptation and is impaired in muscular dystrophy. *J Clin Invest,* 120**,** 2672-83.

Taylor, M., Graw, S., Sinagra, G., Barnes, C., Slavov, D., Brun, F., Pinamonti, B., Salcedo, E. E., Sauer, W., Pyxaras, S., Anderson, B., Simon, B., **Bogomolovas, J**., Labeit, S., Granzier, H. & Mestroni, L. 2011. Genetic variation in titin in arrhythmogenic right ventricular cardiomyopathy-overlap syndromes. *Circulation,* 124**,** 876-85.

Von Castelmur, E., Strumpfer, J., Franke, B., **Bogomolovas, J**., Barbieri, S., Qadota, H., Konarev, P. V., Svergun, D. I., Labeit, S., Benian, G. M., Schulten, K. & Mayans, O. 2012. Identification of an N-terminal inhibitory extension as the primary mechanosensory regulator of twitchin kinase. *Proc Natl Acad Sci U S A,* 109**,** 13608-13.

Chung, C. S., **Bogomolovas, J**., Gasch, A., Hidalgo, C. G., Labeit, S. & Granzier, H. L. 2011. Titin-actin interaction: PEVK-actin-based viscosity in a large animal. *J Biomed Biotechnol,* 2011**,** 310791.

Anderson, B. R., **Bogomolovas, J**., Labeit, S. & Granzier, H. 2013. Single Molecule Force Spectroscopy on Titin Implicates Ig Domain Stability as a Cardiac Disease Mechanism. *J Biol Chem*. 288, 5303-15

Rudolf, R., **Bogomolovas, J**., Strack, S., Choi, K. R., Khan, M. M., Wagner, A., Brohm, K., Hanashima, A., Gasch, A., Labeit, D. & Labeit, S. 2013. Regulation of nicotinic acetylcholine receptor turnover by MuRF1 connects

muscle activity to endo/lysosomal and atrophy pathways. *Age (Dordr),* 35**,** 1663-74.

Bogomolovas J, Gasch A, Simkovic F, Rigden DJ, Labeit S, Mayans O. 2014 Titin kinase is an inactive pseudokinase scaffold that supports MuRF1 recruitment to the sarcomeric M-line. *Open Biol*, 4(5)

8.4.2 Book chapters

Labeit, S., **Bogomolovas, J**., Labeit, D. & Granzier, H. 2011. Titin Gene (TTN). *In: eLS.* John Wiley & Sons, Ltd.

Bogomolovas, J., Granzier, H. & Labeit, S. 2012. Giant Proteins. *In:* Mooren, F. (ed.) *Encyclopedia of Exercise Medicine in Health and Disease.* Springer Berlin Heidelberg.

8.5 Appendix 5 Copyright permissions and statements

Figure 1.1 was reprinted from *Physiology (Bethesda)* **25**, Linke W A , and Krüger M The Giant Protein Titin as an Integrator of Myocyte Signaling Pathways, 186-198, 2010, with permission from American Physiological Society

Table 1.1 was adapted from A. Ackermann and Aikaterini Kontrogianni-Konstantopoulos, Cardiomyopathies: when the Goliaths of Heart Muscle Hurt, 2013 published under the CC BY 3.0 license, with permission from Maegen Ackermann and Aikaterini Kontrogianni-Konstantopoulos